Fall 2015

Mechanical characteristics of organically modified fly ash-kaolinite mixtures

Xin Kang

Department: Civil, Architectural and Environmental Engineering

MECHANICAL CHARACTERISTICS OF ORGANICALLY MODIFIED FLY ASH-KAOLINITE MIXTURES

by

XIN KANG

A DISSERTATION

Presented to the Faculty of the Graduate School of the

MISSOURI UNIVERSITY OF SCIENCE AND TECHNOLOGY

In Partial Fulfillment of the Requirements for the Degree

DOCTOR OF PHILOSOPHY

in

CIVIL ENGINEERING

2015

Approved
Bate Bate, Advisor
Yu-Ning Louis Ge
Ronaldo Luna
J. David Rogers
Jianmin Wang

ABSTRACT

Fly ash is a hazardous waste material to the environment. Beneficial reuse of fly ash, however, brings economic and environmental benefits, i.e., decreases the cost of disposal, reduces greenhouse gas emission, and improves mechanical properties of construction materials. Due to the lack of pozzolanic properties, the reuse rate of Class F fly ash in geotechnical engineering is relatively low (ACAA 2013). In order to promote the effectiveness and sustainability of high volume reuse of class F fly ash in geotechnical engineering, biopolymers (Chitosan, and Xanthan gum) and synthetic polymers (Polyethylene Oxide, PEO) were used instead of the traditional stabilizers to improve the engineering behaviors of fly ash-kaolinite mixtures. The effects of polymers on microstructure development and geotechnical properties (i.e., stiffness, stiffness anisotropy and strength) of fly ash-kaolinite mixtures were measured in the laboratory. Shear wave velocity (V_s) and V_s anisotropy of organically modified fly ash-kaolinite mixtures were investigated by a self-developed floating wall-type consolidometer bender element testing system. V_s results showed that PEO and chitosan increased V_s of the fly ash-kaolinite mixtures, while xanthan gum decreased V_s. V_s anisotropy of the fly ash-kaolinite mixtures was decreased by the addition of polymers. Critical-state friction angles of fly ash-kaolinite mixtures increased with the addition of PEO and chitosan, while decreased with xanthan gum. Polymer bridging and columbic interactions, and the subsequent changes in size and fabric of kaolinite are the major influencing mechanisms. Physicochemical effects and the fly ash ratio also contributed to the observed changes.

ACKNOWLEDGMENTS

I would like to especially thank my advisor, Dr. Bate, for his guidance and for inspiring me with his deep love of science. Also, I would like to express my great appreciation to my advisory committee, Drs. Yu-Ning Louis Ge, Ronaldo Luna, J. David Rogers, and Jianmin Wang for their valuable advice, comments, and suggestions.

I wish to thank the Missouri University of Science and Technology (S&T) and the Department of Civil, Architectural, and Environmental Engineering (CArE) for the assistantships I had during the course of my studies. I also wish to thank Missouri S&T Materials Research Center (MRC) and Center for Infrastructure Engineering Studies (CIES) for providing funds and equipment for this study.

I want to thank lab technicians Scott Parker for helping me building up the Floating Wall Consolidometer Type-Bender Element Testing System, and Gary Abbott for helping me calibrate the testing system. I also want to thank my graduate student colleagues: Junnan Cao, Michelle Deng, Songyi Liu, Kerry Magner, Audai Theinat, Xiaoyi Zhao, and Jack Zhu who gave me valuable suggestions during my study. Also, I would like to thank my undergraduate student researchers, Samantha Smith and Christopher Waldron, who helped me with the Atterberg limits and Proctor Compaction tests of the organically treated soils.

Finally, I wish to thank my family and friends for their unflinching support throughout my study in Missouri S&T.

TABLE OF CONTENTS

Page

ABSTRACT iii

ACKNOWLEDGMENTS iv

LIST OF ILLUSTRATIONS ix

LIST OF TABLES xiv

NOMENCLATURE xv

SECTION

1. INTRODUCTION 1

1.1. OVERVIEW 1

1.2. OBJECTIVES 3

1.3. DISSERTATION LAYOUT 4

2. LITERATURE REVIEW 6

2.1. BENEFICIAL REUSE OF FLY ASH 6

2.2. FLY ASH SOIL STABILIZATION 8

2.3. POLYMER SOIL STABILIZATION 10

2.4. THE STRENGTH, STIFFNESS, AND STIFFNESS ANISOTROPY OF POLYMER MODIFIED FLY ASH-KAOLINITE MIXTURES 13

2.4.1. Strength 13

2.4.2. Stiffness and Stiffness Anisotropy. 14

3. CHARACTERIZATION OF ORGANICALLY MODIFIED FLY ASH-KAOLINITE MIXTURES 18

3.1. INTRODUCTION 18

3.2. MATERIALS 19

3.3. METHODOLOGY 21

3.4. RESULTS AND DISSCUSSIONS 23

3.4.1. Scanning Electron Microscopy (SEM) Images 23

3.4.2. pH and Electrical Conductivity. 28

3.4.3. Atterberg Limits. 31

3.4.4. Proctor Compaction Characteristics and Thermal Conductivity 33

3.5. SUMMARY 34

4. MEASUREMENT OF STIFFNESS ANISOTROPY IN KAOLINITE USING BENDER ELEMENTS IN A FLOATING WALL CONSOLIDOMETER 38
4.1. INTRODUCTION 38
4.2. DESIGN OF THE FLOATING WALL CONSOLIDOMETER-TYPE BENDER ELEMENT TESTING SYSTEM 41
4.2.1. Bender Element 41
4.2.2. Floating Wall Consolidometer Cell Design 42
4.2.3. Chamber Controlling the Bulk Environment 44
4.2.4. Signal Generation, Filtering, and Data Acquisition System 44
4.2.5. Excitation Frequency, First Arrival Time, and Travel Distance. 45
4.3. MATERIALS AND EXPERIMENTAL METHODS 47
4.3.1. Materials 47
4.3.2. Sample Preparation 48
4.3.3. Calibration of the Wall-Soil Interface Friction 50
4.4. RESULTS 51
4.4.1. One-Dimensional Consolidation. 51
4.4.2. Typical Received Shear Wave Signals 52
4.4.3. Typical Shear Wave Velocity (V_s) versus Applied Stress Relationship. 54
4.5. DISCUSSIONS 55
4.5.1. Wall-Soil Interface Resistance. 55
4.5.2. Wall-Soil Interface Resistance Corrected Vertical Stress σ'_z 56
4.5.3. Comparison with Studies in the Literature 59
4.5.4. Stress Dependency of V_s 62
4.5.5. Stress-Induced Fabric Anisotropy 64
4.5.6. Void Ratio Dependency of V_s 65
4.5.7. Advantages of the Developed BE Testing System 65
4.6. CONCLUSIONS 68
5. SHEAR WAVE VELOCITY AND ITS ANISOTROPY OF ORGANICALLY MODIFIED FLY ASH-KAOLINITE MIXTURES 71
5.1. INTRODUCTION 71
5.2. MATERIALS 72
5.3. EXPERIMENTAL METHODS 74

5.3.1. Scanning Electron Microscopy (SEM) Imaging. 74
5.3.2. Effective Specific Gravity 74
5.3.3. Determination of the Shell Thickness of Fly Ash Cenospheres. 75
5.3.4. Sample Preparation by Slurry Consolidation Method 75
5.3.5. V_s Measurement with Bender Element Method. 76
5.3.6. Soil-Side Wall Interface Friction Correction. 77
5.4. RESULTS 78
5.4.1. Scanning Electron Microscope Images. 78
5.4.2. Fly Ash Cenosphere Shell Thickness 78
5.4.3. One-Dimensional Consolidation. 81
5.4.4. Typical V_s and V_s Anisotropy Results. 83
5.4.5. V_s and V_s Anisotropy of Organically Modified Soil. 87
5.5. DISCUSSIONS 90
5.5.1. Threshold Fly Ash Content (F_{th}). 90
5.5.2. Effect of Fly Ash Content on the V_s Anisotropy 92
5.5.3. Ionic Strength Effects on V_s Anisotropy. 96
5.5.4. Cross-Anisotropy 96
5.5.5. Effects of Polymers on the V_s and V_s Anisotropy 97
5.5.6. Stress Dependence of V_s 100
5.5.7. Porosity Dependency of V_s 102
5.6. CONCLUSIONS 102
6. LARGE STRAIN STRESS-STRAIN RESPONSES OF ORGANICALLY MODIFIED HIGH VOLUME CLASS F FLY ASH-KAOLINITE 106
6.1. INTRODUCTION 106
6.2. MATERIALS AND EXPERIMENTAL METHODOLOGY 107
6.2.1. Materials 107
6.2.2. Sample Preparation 109
6.2.3. Scanning Electron Microscopy Imaging 110
6.2.4. Consolidated Undrained (CU) Triaxial Compression Test 110
6.3. RESULTS 113
6.3.1. Microfabric and Particle Associations 113
6.3.2. The Coefficient of Consolidation (C_v) 115

6.3.3. Stress-Strain Responses 115
6.4. DISCUSSIONS 123
6.4.1. Effect of Salt on the Stress-Strain Behaviors of Kaolinite 123
6.4.2. Effect of Fly Ash Content on the Stress-Strain Behaviors 124
6.4.3. Effect of Polymers on the Particle Associations and Microfabric. 127
6.4.4. Effect of Polymers on the Stress – Strain Behaviors 128
6.5. CONCLUSIONS 130
7. CONCLUSIONS AND RECOMMENDATIONS 132
7.1. INTRODUCTION 132
7.2. CONCLUSIONS 132
7.3. RECOMMENDATIONS 136
APPENDIX 138
BIBLIOGRAPHY 140
VITA 151

LIST OF ILLUSTRATIONS

Figure 3-1 Grain size distributions of the kaolinite and fly ash..... 21

Figure 3-2 The chemical structures of PEO, Chitosan, and Xanthan gum. 22

Figure 3-3 (a) Decagon Devices KD2 Pro thermal properties analyzer; (b) Accument excel XL 60 dual channel pH/Ion/Conductivity/DO meter..... 24

Figure 3-4 SEM images of (a) fly ash, (b) pulverized fly ash, (c) untreated kaolinite, and kaolinite treated by organic polymers (d) PEO, (e) Chitosan, and (e) Xanthan gum. 26

Figure 3-5 SEM images of organically modified fly ash soil mixtures; (a) 30% fly ash + 70 % kaolinite without organic agents, (b) 60% fly ash + 40% kaolinite without organic agents, (c) 100% fly ash without organic agents, (d) PEO modified 30% fly ash-kaolinite mixture, (e) chitosan modified 30% fly ash-kaolinite mixture, and xanthan gum modified 30% fly ash-kaolinite mixture..... 27

Figure 3-6 Fly ash content versus the electrolyte electrical conductivity..... 29

Figure 3-7 Electrical conductivity versus the organic concentration of different solutions..... 30

Figure 3-8 The relationship between measured pH and organic concentrations 30

Figure 3-9 Liquid limit (LL), and Plastic Limit (PL), and Plasticity Index (PI) of fly ash-kaolinite mixtures at different fly ash mixing ratios..... 32

Figure 3-10 Liquid limit of kaolinite at different organic concentrations. 33

Figure 3-11 (a) Proctor compaction curves of kaolinite and fly Ash (30 %)-kaolinite (70 %) mixtures; (b) Thermal conductivity versus water contents of kaolinite and fly ash (30 %)-kaolinite (70 %) mixtures. 36

Figure 3-12 (a) dry unit weight versus organic content (b) thermal conductivity versus organic content of kaolinite and fly ash (30%)-kaolinite (70%) mixtures under the standard proctor compaction effort. 37

Figure 4-1 Floating wall consolidometer-type bender element testing system. Subset (a) newly-made vertical bender element. (b) vertical (left) and horizontal (right) bender elements after five tests. 42

Figure 4-2 Soil deformation-induced bending moment on horizontal bender elements in a) a fixed wall consolidometer and b) a floating wall consolidometer. 43

Figure 4-3 Schematic setup of the floating wall consolidometer cell. Left: side view, right: top view. 44

Figure 4-4 Determination of the first arrival time using single cycle sine wave as the input function. 46

Figure 4-5 Grain size distribution curves for Georgia kaolinite RP-2 (Active Minerals International, Hunt Valley, MD, USA, 2007) used in this study; Speswhite kaolin (Imerys Performance & Filtration Minerals, Cornwall, UK, 2008) used in Wang and Siu (2006), Viggiani and Atkinson (1995) and Jovicic and Coop (1998); Vanderbilt Peerless kaolin clay (R.T. Vanderbilt Company, Inc., Norwalk, CT, USA, 2011) used in Fam and Santamarina (1997) Fam and Santamarina (1995), and kaolin used in Shibuya et al. (1995) 47

Figure 4-6 (a) Wall-soil interface resistance test setup; (b) boundary conditions for applied 800 kPa vertical loading; (c) representative soil element at depth of z. 51

Figure 4-7 e-log $\sigma_v^{'}$ curves of kaolinite samples at different NaCl concentrations. 52

Figure 4-8 Typical received shear wave signals under different applied stresses (kaolinite sample with 0.005 mol/l NaCl solution, S-wave in hh Direction, arrows pointing at first arrival time) 53

Figure 4-9 Typical shear wave velocity versus applied vertical stress plot of kaolinite samples. (data was from a kaolinite sample with 0.005 mol/l NaCl)..... 54

Figure 4-10 Measured wall-soil interface resistance (in terms of cumulative force, unit: N) vs. applied vertical stress for tap water kaolinite sample. 57

Figure 4-11 Comparison of floating wall and fixed wall (hypothesized) consolidometer BE test setup for kaolinite sample in 1 mol/l NaCl under 800 kPa vertical stress. a) Soil-wall relative displacement, soil move downward relative to the wall is positive; b). vertical effective stress considering wall friction; c). friction along the sample height, upward friction is positive. 58

Figure 4-12 Comparison with stiffness of different kaolinites studied in the literature. (a) V_s versus applied vertical stress results; (b) G_{max} versus mean effective stress (friction corrected mean effective stress values in this study were used) 61

Figure 4-13 Typical values for α and β coefficients in this study. 64

Figure 4-14 Shear wave velocity versus interface resistance corrected mean effective stress on the polarization plane for kaolinite samples with 0.005 and 1.0 mol/l NaCl solutions. (a) loading; (b) unloading..... 66

Figure 4-15 Shear wave velocity versus void ratio in the hh direction during loading. ... 67

Figure 5-1 A sketch of the floating wall type consolidometer cell and the bender elements setup. 72

Figure 5-2 Grain size distributions of fly ash and kaolinite..... 73

Figure 5-3 The chemical structures of PEO, chitosan, and xanthan gum. 74

Figure 5-4 SEM images of fly ash (a), pulverized fly ash (b), untreated kaolinite (c), and fly ash-kaolinite mixtures at (d) 30% and (e) 60% fly ash content. 79

Figure 5-5 SEM images of kaolinite modified by (a) PEO; (c) chitosan; (e) xanthan gum, and SEM images of 30% fly ash-kaolinite mixtures modified by (b) PEO; (d) chitosan; (f) xanthan gum. 80

Figure 5-6 *e*-log p' curves of fly ash-kaolinite mixtures and organically modified 30% fly ash-kaolinite mixtures..... 82

Figure 5-7 V_s in *vh*, *hv*, and *hh* directions of 30% fly ash-kaolinite mixtures during loading and unloading stages. 84

Figure 5-8 V_s in *vh*, *hv*, and *hh* directions of fly ash-kaolinite mixtures during (a) loading; and (b) unloading stages. The symbols represent test data points and solid lines represent fitting results by Eq. 5-3 by least square method. Data during the loading and unloading stages were fitted separately and high R^2 values (0.9025-0.9970) were achieved. 85

Figure 5-9 V_{s-hh}/V_{s-vh} and V_{s-hv}/V_{s-vh} of fly ash-kaolinite mixtures at 10% and 60% fly ash contents during (a) loading; and (b) unloading conditions. 86

Figure 5-10 The $V_{s\text{-}vh}$ of organically modified fly ash-kaolinite mixtures during loading. 87

Figure 5-11 The V_s of PEO, Xanthan gum modified 30 % fly ash-kaolinite mixtures in vh, hv, and hh directions during (a) loading condition, and (b) unloading condition 88

Figure 5-12 V_{s-hh}/V_{s-vh} of 30% fly ash-kaolinite mixtures modified by different polymers during (a) loading; and (b) unloading conditions. 89

Figure 5-13 The shear wave velocity changes in *vh*, *hv*, and *hh* directions of fly ash-kaolinite mixtures at different fly ash mixing ratios at $\sigma_{corr}^{'} = 600kPa$; the insets illustrate the volumetric content of fly ash cenospheres in the fly ash-kaolinite mixtures. 92

Figure 5-14 V_{s-hv}/V_{s-vh} of fly ash-kaolinite mixtures at different fly ash contents (0% -100%) during (a) loading; and (b) unloading conditions. 94

Figure 5-15 Shear wave velocity ratio V_{s-hv}/V_{s-vh} of fly ash-kaolinite mixtures at different fly ash contents during (a) loading and (b) unloading conditions. . 95

Figure 5-16 Fitted values of α and β coefficients of (a) fly ash-kaolinite mixtures; and (b) organically modified 30% fly ash-kaolinite mixtures..... 103

Figure 5-17 V_{s-vh} of fly ash-kaolinite mixtures during loading as a function of porosity..... 104

Figure 6-1 Grain size distributions of kaolinite and fly ash..... 108

Figure 6-2 The chemical structures of PEO, Chitosan, and Xanthan gum 109

Figure 6-3 Scanning electron microscope images of: (a) Georgia RP-2 kaolinite particles, (b) fly ash particles, (c) 30 % fly ash-kaolinite mixtures, (d) Xanthan gum modified kaolinite, (e) PEO modified kaolinite, (f) Chitosan modified kaolinite, (g) PEO modified 30 % fly ash-kaolinite mixture, (h) Chitosan modified 30 % fly ash-kaolinite mixture, and (i) Xanthan gum modified 30 % fly ash-kaolinite mixture. 114

Figure 6-4 Consolidated undrained triaxial compression strength test results of pure kaolinite (a) stress-strain diagram; (b) pore-water pressure diagram; (c) $p^{'}-q$ diagram; and 1.0 mol/l NaCl treated kaolinite: (d) stress-strain diagram; (e) pore-water pressure diagram; (f) $p^{'}-q$ diagram. 117

Figure 6-5 Consolidated undrained triaxial compression strength test results of 30 % fly ash-kaolinite mixture (a) stress-strain diagram; (b) pore-water pressure diagram; (c) $p^{'}-q$ diagram; and 100 % fly ash samples: (d) stress-strain diagram; (e) pore-water pressure diagram; (f) $p^{'}-q$ diagram. 118

Figure 6-6 Consolidated undrained triaxial compression strength test results of PEO modified 30 % fly ash-kaolinite mixtures (a) stress-strain diagram; (b) pore-water pressure diagram; (c) $p^{'}-q$ diagram..... 119

Figure 6-7 Normal consolidated lines (NCL) and critical state lines (CSL) for test samples: (a) pure kaolinite and salt treated kaolinite; (b) fly ash kaolinite mixtures at different fly ash content; (c) organically modified fly ash kaolinite mixtures at 30% fly ash content. 122

Figure 6-8 (a) Peak and critical-state friction angles for tested specimens as a function of the fly ash content: (b) critical-state friction angle change induced by different salt and organic polymers for both kaolinite and 30% fly ash-kaolinite mixtures; (c) critical-state of fly ash-kaolinite mixtures in p'-q space; (d) deviatoric stress as a function of effective mean normal stress of fly ash-kaolinite mixture modified by different polymers. 123

LIST OF TABLES

Table 3-1 Chemical analysis results of RP-2 kaolinite and fly ash based on the X-Ray Diffraction (XRD) test 22

Table 4-1 Comparison of the properties of kaolinites used in different studies 48

Table 4-2 Friction corrected vertical effective stress calculation spreadsheet for 0.005 and 1 mol/l kaolinite samples 60

Table 5-1 Initial void ratio, compression, and recompression indices of fly ash-kaolinite mixtures and organically modified 30% fly ash-kaolinite mixtures 83

Table 6-1 Chemical analysis results of RP-2 kaolinite and fly ash from XRD Tests.. 107

Table 6-2 Physical and mechanical properties of tested samples 112

Table 6-3 Parameters of the NCL and CSL 121

NOMENCLATURE

Symbol	Description
α	is the velocity of a medium subject to 1 kPa confinement, m/s
β	fitting constant, it is related with the contact effects
$\sigma_z^{'}$, $\sigma_v^{'}$	vertical effective stress
$\sigma_m^{'}$	mean normal effective stress
$\sigma_{corr}^{'}$	friction corrected mean normal effective stress on the polarization plane
τ	shear stress
$\phi_p^{'}$	peak friction angle
$\phi_{cs}^{'}$	critical-state friction angle
$\varphi^{'}$	soil-wall interface friction angle
ρ	bulk soil density
ρ_w	density of water
γ	unit weight
κ	thermal conductivity
ξ	electrical conductivity
λ_i	shear wave length
ω	water content
c	cohesion
K_0	coefficient of lateral earth pressure at rest
d_{50}	median grain size
G_s	specific gravity

G_{max}	maximum shear modulus
R_d	a ratio of the shear wave travel distance over the wave length
L_i	shear wave travel distance, BE tip-to-tip distance
F_{th}	threshold fly ash content
R	radius of the fly ash cenospheres
S	fly ash cenospheres shell thickness
D	diameter
H	height
V_s	shear wave velocity
LL	liquid limit
PL	plastic limit
PI	plasticity index
OCR	over consolidation ratio

1. INTRODUCTION

1.1. OVERVIEW

Fly ash is a byproduct that generated from the coal fired thermal power plants. Generally, the fly ashes are disposed in the geological environment, such as fly ash ponds, impoundments, and landfills, which not only increase the fly ash transportation cost but also bring serious problems and pollution to the environment (Ferguson and Levorson 1999; White et al. 2005; Yeboah and Burns 2011; ACCA 2013). Beneficial reuse of fly ash, however, can produce positive environmental, economic, and product benefits. For example, fly ash reuse has been gradually gaining strength in geotechnical engineering applications in recent decades, such as deep soil mixing, soil replacing, and soil stabilization (Ferguson 1993). The addition of class C fly ash to soil could change the soil gradation (physically), bind soil particles together and modify the microstructure (pozzolanic reaction, chemically); therefore, improves the engineering properties. Due to its excellent pozzolanic properties, class C fly ash has been reused extensively in traditional geotechnical engineering applications, however, the reuse rate of class F fly ash is relatively low which is due to a number of practical reasons, i.e., little cementious effects (Yeboah and Burns 2011). The class F fly ash normally contains very limited amount of pozzolanic materials (i.e., calcium, silica and alumina), which needs binding agents (i.e., lime and cement) to activate the pozzolanic process (Ferguson 1993). However, the volume of the reused class F fly ash by traditional stabilizers (lime/cement) is normally less than 20 wt.% (Ferguson 1993; Zia and Fox 2000; White et al. 2005). In addition, the manufacture process of cement/lime will result in high volume of greenhouse gas emission (CO_2). Therefore, environmental friendly and sustainable

binding agents that can substitute traditional stabilizers and reduce greenhouse gas emission are highly needed for fostering high volume reuse of class F fly ash in geotechnical engineering.

Recent development of polymer science has brought revolutionary breakthrough to soil stabilization/modification in geotechnical engineering. A number of studies have been published discussing the use of organic polymers as soil conditioners and for improving soil structure and physical properties. Organic agents (organic cations, surfactants, synthetic polymers, and biopolymers) are found to have the abilities to enhance the bonding between adjacent soil aggregates, improve the stiffness, shear strength, and erosion resistance of geomaterials (Martin et al. 1996; Kavazanjian et al. 2009; Cabalar and Canakci, 2005; Khatami and O'Kelly 2013; Bate et al. 2013; Bate et al. 2014). The adsorbed polymers were able to reduce net surface charge (indicated by zeta potential) of the soil particles, condense the soil fabric, and increase the interparticle attractive forces and the interfacial frictional characteristics (Bate et al. 2013; Nugent et al. 2010; Orts et al. 2007). Furthermore, organic polymers were considered as environmental friendly and cost-effective binding agents that are capable of substituting traditional soil stabilizers (such as cement and lime) and reducing greenhouse gas emission and effect of global warming.

The advantages of organic polymers and successful cases reported in the literature have shown promising results, however, only a few studies were performed on modifying the fly ash-kaolinite mixtures with organic matters. Productive reuse of fly ash has significant meaning to the sustainable development. The interactions between fly ash particles/soil particles and polymers could provide additional bonding (i.e., polymer

bridging), which might also improve the engineering performance of the organically modified fly ash-soil mixtures. Therefore, in order to foster high volume reuse of class F fly ash in geotechnical engineering practice and provide in-depth understanding of the connections between mechanical and physicochemical properties of the organically fly ash-kaolinite mixtures, the effects of polymers on the geotechnical properties (i.e., stiffness and strength) of fly ash-kaolinite mixtures were investigated and the associated polymer-soil stabilization mechanisms were explored in this study.

1.2. OBJECTIVES

In order to foster high volume reuse of class F fly ash in geotechnical engineering practice and provide in-depth understanding of the connections between mechanical and physicochemical properties of the organically modified fly ash-kaolinite mixtures, the effects of organic agents (both synthetic polymers and biopolymers) on the geotechnical properties of Class F fly ash-kaolinite mixtures were investigated and the main objectives of this study are listed as follows:

(1) Characterize the microstructure of organically modified fly ash-kaolinite mixtures by using the scanning electron microscopy (SEM), and investigate their physicochemical properties (i.e., pH, conductivity) and geotechnical properties (i.e., Atterberg limits, proctor characteristics, compressibility and swelling potential and thermal conductivity).

(2) Design and manufacture a floating wall consolidometer-type bender element testing system which is able to measure the V_s of a soil sample in three orthogonal directions (i.e., *vh*, *hv*, and *hh*) under high stress levels. Investigate the salt effect and stress-induced V_s anisotropy of kaolinite samples during K_0 consolidation.

(3) Quantify the stiffness and stiffness anisotropy of fly ash-containing geomaterials and elucidates their dependency on the polymeric additives with self-developed floating-type consolidometer bender element testing system. The influencing factors on V_s and V_s anisotropy of a binary system (fly ash-kaolinite mixture), including the stress conditions, physicochemical conditions of polymer solutions, and the associated underlying mechanisms were evaluated and discussed.

(4) Investigate the large-strain stress-strain behaviors of organically modified fly ash-kaolinite mixtures by conducting consolidated undrained (CU) triaxial shear tests and evaluate the effects of polymers on the induced stress-strain behaviors of the fly ash-kaolinite mixtures.

1.3. DISSERTATION LAYOUT

This dissertation includes seven chapters. The first and second chapters are focused on the introduction and literature of the roles of fly ash and organic agents in stabilizing problematic soils and the bender element testing system and V_s anisotropy of geomaterials. The potential of organic agents to increase the stiffness and shear resistance is explored and a description of the studies of the organic effects was presented.

The objective (1) is achieved in Chapter 3 and which describes characterization of the research materials and some basic geotechnical properties of the organically modified fly ash-kaolinite mixtures. Focuses are given on the material properties, microfabrics (SEM images), Atterberg limits, thermal conductivity, and the proctor compaction behaviors of the organically modified fly ash-kaolinite mixtures.

Chapter 4 meets the objective (2) which shows the detailed design, development, and manufacture of the floating wall consolidometer-type bender element testing system,

and its capability to test the V_s and the V_s anisotropy of geomaterials. The floating wall design eliminated the detrimental bending moment that acted upon the horizontally installed bender elements due to soil settlement in a traditional fixed wall setup, which significantly improved signal quality and bender element reuse. One-dimensionally slurry-consolidated Georgia RP-2 Kaolinite samples, prepared with 0.005 and 1 mol/l NaCl solutions, were tested in this system. Stress and salinity influences on the stiffness and fabric anisotropy of kaolinite are discussed and related with the special microfabrics. In addition, a theoretical equation was derived to account for the soil-wall interface friction loss during large strain consolidation.

Chapter 5 meets the objective (3) which investigated the V_s and the V_s anisotropy of organically modified fly ash-kaolinite mixtures using the newly designed floating wall consolidometer type bender element testing system. The effects of stress, fly ash content, and polymers on the compressibility, the swelling potential, the V_s, and V_s anisotropy of fly ash-kaolinite mixtures were investigated. The cross-anisotropy of the organically modified fly ash-kaolinite mixtures has also been evaluated by using the novel designed bender element testing system.

Consolidated undrained triaxial shear test results on the organically modified soils are shown in chapter 6. This chapter addressed the objective (4) which focused on investigating the consolidated undrained stress-strain behaviors and the critical-state friction angles of organically modified fly ash-kaolinite mixtures.

Chapter 7 gives the conclusion of all the studies performed as part of this dissertation. Potential applications are proposed. Also, areas of future work are recommended.

2. LITERATURE REVIEW

2.1. BENEFICIAL REUSE OF FLY ASH

Every year, over 90% of the U.S. coal is burned in coal-fired power plants for electricity production, which inevitably generate large amount of coal combustion residuals (CCRs, which typically categorized as fly ash, bottom ash, and slag) (EIA, 2014). American Coal Ash Association (ACAA) reported that about 115 million metric tons of CCRs were produced annually in the U.S. (ACAA annual report, 2013), where fly ash is the dominant and accounted for 46% (53.4 million metric tons). At first glance, fly ash is very fine powders in grey to yellow color. Hydrometer test revealed that the fly ash particle distributions are generally in a range of silt to fine sand, i.e., Vempati et al. (1994) conducted a detailed research of the particle size distributions of class F fly ash and found that about 90% of the particle size was greater than 0.09 mm, and less than 1% of the fly ash particle was presented in the fine fraction (less than 0.075 mm). The microstructure of fly ash has been discovered under the help of the Scanning Electron Microcopy (SEM). Generally, fly ash particles are in spherical shape and varied in size. Most of the fly ash particles are smooth, while some relatively oversized particles have highly outlines (Kang et al. 2013; White et al. 2005). The liquid limit (LL) and plastic limit (PL) of fly ash are found to be very close to each other (Kang et al. 2013), thus it is usually considered as non-plasticity geomaterials. The mineralogical composition of fly ash is largely dependent on the geological factors that related to the formation and deposition of coal and its combustion conditions. According to the different chemical compositions, fly ash is generally classified into two types, the class C fly ash and the Class F fly ash, respectively (ASTM C618). Class C fly ash has high volume of calcium,

silica and alumina which exhibits good self-cementitious properties. On the contrary, class F fly ash has very weak pozzolanic effects. Some fly ashes may also contain heavy metals and even with radioactive substances.

The majority of the fly ash is disposed in geological environment, such as landfills and surface impoundments. The disposed fly ash is considered as a hazardous waste which poses great hazards to the environment (ACAA 2013; Ferguson and Levorson 1999; White et al. 2005; Yeboah and Burns 2011). For example, a huge coal ash spill was discovered on February 2, 2014 at the Duke Energy power plant in North Carolina. Approximately 82,000 tons of fly ash was flowed into the Dan River which caused significant damage to the riverbank and the residential neighborhood. The Dan River spill, however, is not the only recent spill of fly ash. A catastrophic failure of fly ash dike was happened at Tennessee Valley Authority's (TVA's) Kingston Fossil Plant on Dec. 22nd, 2008. About 1.1 billion gallons of coal ash was released and covered roughly 300 acres, directly impacted about 400 homes, destroyed a highway and railroad line, and closed the adjacent Emory River (Dotson et al. 2013). In addition, the trace amount of heavy metals and other substances in fly ash are often leached into underground water and aquifers by rainwater infiltration and seepage flow (Class F fly ash, Walker 2005), which pollute the environment and bring detrimental effects to the human health. In 2014, for instance, residents living near the Buck Steam Station in Dukeville, North Carolina, were told that "coal ash pits near their homes could be leaching dangerous materials into groundwater". Moreover, exposure to fly ash through skin contact, inhalation of fine particle dust, and drinking water may also present health risks. The National Academy of Sciences noted in 2007 that "the presence of high

contaminant levels in many CCR leachates may create human health and ecological concerns".

Although the disposed fly ash has been considered as hazardous waste, beneficial reuse of fly ash has significant meaning to the sustainable development and global energy market. The US Environmental Protection Agency (EPA) encourages beneficial reuse of fly ash in an appropriate and protective manner, because this practice can produce positive environmental, economic, and product benefits such as: reduced use of virgin resources, lower greenhouse gas emissions, reduced cost of fly ash disposal, and improved strength and durability of materials. Due to its excellent pozzolanic characteristics, the reuse of fly ash in soil stabilization, construction and building materials, and highway and subgrade soil replacement have brought important benefits to the environment and the economy when used in encapsulated forms. For example, one of the largest encapsulated use reported by the American Coal Ash Association (ACAA 2013) is reuse of fly ash in "concrete/concrete products/grout" (11.8 million tons), making up nearly 50 percent of the total amount of coal ash that is beneficially reused.

2.2. FLY ASH SOIL STABILIZATION

In geotechnical engineering, fly ash was found to be a good binding agent for soil stabilization. The addition of class C fly ash can improve soil workability; reduce segregation, compromises drying and shrinkage, decreases permeability and compressibility, and increase stiffness and strength (Ferguson 1993; Kang et al. 2013; Kang et al. 2015; Levorson 1999; White et al. 2005; Yeboah and Burns 2011). However, the coal combustion production and use survey report from American Coal Ash Association (ACAA 2013) indicated that the reuse rate of fly ash in geotechnical

applications is relatively low. For example, the percentage of fly ash reuse in structural fills/embankments, road base/sub base, and soil modification/stabilization only takes 1.2%, 0.6%, and 12.8% of the total amount of fly ash, which is far below the reuse rate of fly ash in concrete/productions (50%).

Soil stabilization by fly ash depends on the fly ash hydration (short term strength gain) and pozzolanic reactions (long term strength gain). The hydration of fly ash compresses the soil particle's DDL and promotes flocculation and aggregation, which results in the increased pore solution surface tension and producing an increase of the apparent cohesion between soil particles, thus improves the early strength of the fly ash-soil mixtures. The short term strength gain, however, is generally weak compared with the long term strength improvement resulted from pozzolanic reactions (White et al. 2005). Pozzolanic reaction happens when fly ash contains (or cement and lime are added) high volume of calcium oxide (CaO) / calcium hydroxide ($Ca(OH)_2$), during which the calcium silicate/aluminate hydrate (CSH/CASH) are produced. The pozzolanic products (CSH/CASH) will fill the capillary pores, bind soil particles together and densify the microstructure, thus increases the strength and stiffness of the stabilized soil (Janz and Johansson 2002). However, the hydration of cement and particularly that of lime plays an important role in initiating the pozzolanic reactions because the pozzolanic reaction rate and strength gain are promotional to the volume of $Ca(OH)_2$, therefore, the cost for soil stabilization will increase as more binding agents have been added.

Compared to class C fly ash, the reuse of class F fly ash in geotechnical engineering applications is relatively low (ACAA 2013) which is due to a number of practical reasons, including little cementitious effects, easy to be liquefied, drastic

mechanical drop due to small variation of water content, weak water retention capacity, lack of the guidelines to characterize fly ash, and environment concerns. Traditional stabilizers, such as lime and cement, are often used together with Class F fly ash to effectively enhance the pozzolanic reactions so as to improve the mechanical properties of the fly ash-soil mixtures. However the volume of the reused fly ash by traditional stabilizers is normally less than 20 wt.%, above which desiccation cracks might develop and significantly reduce the strength (White et al. 2005; Zia and Fox 2000). Besides, the costs of lime and cement are high and their manufacture process will result in high volume of greenhouse gas emission (CO_2) which is harmful to the environment. For example, every one ton of cement produced, about one ton of carbon dioxide is released and about 6.5 million BTUs (British thermal unit, 1 BTU=1055 joules) of energy is consumed which is enough electricity to power the average American home for almost a month (Natesan et al. 2003). Furthermore, the Class F fly ash-soil mixture's strength was found to increase as the class F fly ash content increased, however, the shear strength become quite constant when at high fly ash content (50 wt.%-80 wt.%, Kim et al. 2005; Rivard-Lentz et al. 1997). Therefore, in order to foster high volume reuse of class F fly ash in traditional geotechnical engineering, alternative stabilizers, such as organic polymers, are highly needed to replace the traditional stabilizers, improve the engineering properties of the fly ash-kaolinite mixture, and reduce the cost and environmental problems caused by the disposal of fly ash.

2.3. POLYMER SOIL STABILIZATION

Environmental friendly and sustainable binding agents, i.e., organic polymers, could not only substitute the traditional stabilizers (cement/lime) but also reduce the

greenhouse gas emission from Portland cement industry. A number of recent studies indicated that the organic polymers, such as surfactants and polymers, could effectively improve stiffness (Bate et al. 2013; Choo et al. 2015), shear strength (Al-Khanbashi and Abdalla 2006; Bate 2010; Bate and Burns 2010; Bate et al. 2013; Bate et al. 2014; Cabalar and Canakci 2005; Khatami and O'Kelly 2013; Martin et al. 1996; Newman and Tingle 2004), frictional resistance (Bate et al. 2013; Bate et al. 2014; Graber et al. 2006; Yoshizawa et al. 1993), wind and tide erosion resistance (Aase et al. 1998; Kavazanjian et al. 2009; Nugent et al. 2010; Orts et al. 2007; Williams et al. 2014), and permeability (Bouazza et al. 2009) of geomaterials due to the extensive polymer-clay interactions. For example, the addition of a surfactant with long carbon chain (C_{16}) onto montmorillonite can increase the friction angle up to 60^o, and increase the shear wave velocity (V_s) up to 154 m/s at a mean normal stress of 50 kPa (Bate et al. 2013; Bate et al. 2014). Furthermore, increasing number of studies on organically modified soils were reported in drilling slurry (Mazzieri et al. 2010), slurry wall, mineral separation (Chandraprabha et al. 2004), and geosynthetic clay liners (Lake and Rowe 2005).

The soil improvement mechanisms by polymers are more complicated, consisting of polymer bridging, Coulomb forces, and the interaction between the individual function group and the clay mineral surfaces. Fly ash is often negatively charged, the reuse of which in geotechnical engineering could also benefit from the addition of organics through polymer bridging and electrostatic forces. Polymer-soil interactions depend on the polymer charge or polarity; therefore, the cationic, neutral, and anionic polymers will have distinct interactions with the negatively charged clay surfaces (Theng 1982). In summary, Columbian interaction (electrostatic forces), intercalation into the interlayer

space of expandable clays, ion-dipole interaction, hydrogen boding, and van der Waals forces are the common mechanisms that govern the polymer-clay interactions (Israelachvili 2011; Theng 1982). Cationic polymers, such as polyacrylamide (PAM) and Chitosan, are normally attracted by the negatively charged sites along kaolinite surface through Coulombian attraction (charge neutralization). Once charge neutralization has reached, long-range van der Waals forces and short-range ion-dipole interactions become dominant (Kim and Palomino 2009; Kim and Yang 2012). For non-ionic polymers, hydrogen bonding is the dominant method of adsorption which usually takes place with different functional groups at the surface of the long chains of polymers, i.e., the oxygen and hydroxide functional groups on the kaolinite surface could form hydrogen boding with non-ionic polymers, like polyacrylamide and PEO (Mpofu et al. 2004; Theng 1982). The anionic polymers could interact with the positively charged edge of kaolinite via electrostatic attraction (Benchabane and Bekkour 2006; Tan et al. 2014; Zhang et al. 2013), however, limited adsorption may occur which is due to the relative small area of the "edge" of kaolinite and the strong electrostatic repulsion forces that exist among the negatively charged clay particles and polymers, thus the polymer chains are extended and repelled out with loops and tails (Labille et al. 2005). Higher molecular weight polymers will simultaneously adsorb to several clay particles, forming a three-dimensional matrix. The adsorption process is called "polymer bridging" where the adsorbed polymers serve as "bridges" to agglomerate the suspended particles together and cause flocculation and aggregation (Kim and Yang 2012; Mpofu et al. 2004; Nasser and James 2006; Theng 1982). Chemical properties which include the polymer weight, polymer structure, polymer surface charge, and solubility were all found to influence the polymer adsorption

processes (Kim and Palomino 2009; Nasser and James 2006) and effect of polymer bridging. Polymer clay interactions facilitate microscale fabric change of soil aggregates, which in turn lead to strengthen their macroscale engineering properties.

2.4. THE STRENGTH, STIFFNESS, AND STIFFNESS ANISOTROPY OF POLYMER MODIFIED FLY ASH-KAOLINITE MIXTURES

2.4.1. Strength. The soil stabilization mechanisms by polymers depend on the polymer-soil interactions. A recent study from Nath et al. (2009) showed that the tensile/axial strength of polymer coated (Class F) fly ash was increased up to 33%. Polymers will interact with both the fly ash and kaolinite; however, their effects and mechanisms on the mechanical properties of fly ash-soil mixtures are not well documented in the literature. A detailed literature review indicated that the strength improvement of polymer modified coarse grained soils is mainly attributed to the polymer induced "cohesion" (Cabalar and Canakci 2005; Khatami and O'Kelly 2013; Martin et al. 1996), where the stiffness of polymer "bonds" between sand grains could reach up to 3.8 GPa (Cole et al. 2012). For polymer modified fine grained soils, the strength improvement is attributed to the reduce the net surface charge (indicated by zeta potential) and increase of the interparticle attractive forces due to polymer bridging, Coulombian forces, polymer crosslinking, and formation of the polymer-soil interwoven network (Mitchell and Santamarina 2005; Newman and Tingle 2004; Nugent et al. 2010; Orts et al. 2007; Podsiadlo et al. 20007; Ringelberg et al. 2014; Zhang et al. 2013). The increase of interparticle attractive force by polymer bridging could lead to a flocculated and aggregated interconnected clay-water-polymer network, which condense the soil, increase the aggregate size and effective consolidation pressure, and decrease the pore volumes and water content (Mitchell and Soga 2005), and finally contribute to the

increase of shear strength. On the contrary, dispersion polymers treated soil showed reduction in shear strength which is mainly due to the decrease of attractive forces between clay particles and the polymer induced loose-open microfabric with high double layer repulsion force and exhibited lower internal friction angle (Delage and Lefebvre 1984; Di Maio 1996; Mitchell and Soga 2005; Ringelberg et al. 2014; Santamarina et al. 2001; Wang and Siu 2006; Zhang et al. 2013; Zumsteng et al. 2013).

2.4.2. Stiffness and Stiffness Anisotropy. In recent decades, bender element (BE) has become a standard tool in geotechnical engineering that has been incorporated into conventional triaxial devices, direct shear devices, oedometers, simple shear devices, and model tests to measure the stiffness ($G_{max} = \rho V_s^2$) of geomaterials (Dyvik and Madshus 1985; Lee and Santamarina 2005; Shirley 1978; Thomann and Hryciw 1990; Viggiani and Atkinson 1995). The bender element (piezo-ceramic bending actuator) is an electrical mechanical transducer which can convert mechanical energy either to or from electrical energy. When a voltage is applied to the bender element, one plate will elongate and the other will shorten, thus a net bending displacement is resulted. On the other hand, when a bender element is forced to bend, one layer of the ceramic plate will undergo tension and the other layer will be in compression, and then an electrical signal will be generated. A voltage pulse will cause the entire bender element to bend and generate a “pulse” (shear wave) that can transmit from bender element tip to its adjacent contact soil particles when the bender element is protruded into opposite ends of a soil specimen. The soil particles are vibrated by the transmitting of shear wave. When the shear wave reaches the other bender element (receiver), the distortion of the receiver bender element produces another voltage pulse. The time difference between the two

voltage pulses is measured with an oscilloscope and divided into the distance between the tips of the bender elements to give the shear wave velocity (V_s) of the specimen. A floating wall consolidometer-type bender element testing system was designed in this study which is capable to test the V_s and the V_s anisotropy (V_s in three orthogonal directions) of geomaterials under high stress levels. Compared with the previous designs of bender element testing system (Lee et al. 2008; Leong et al. 2009), the floating wall design eliminated the detrimental bending moment that acted upon the horizontally installed bender elements due to soil settlement in a traditional fixed wall setup, which significantly improved signal quality and bender element reuse. The detailed design, advantages and limitations of floating wall consolidometer-type bender element testing system are presented in Chapter 4.

Geomaterials often have strong anisotropy properties; therefore, the V_s is dependent on the structure of the soil fabric and the measuring directions, for example, in longitudinal or transverse (Jovicic and Coop 1998; Kang et al. 2014; Ng and Leung 2007; Ng et al. 2009; Pennington et al. 1997; Roesler 1979; Santamarina and Cascante 1996; Santamarina et al. 2001; Stoke et al. 1985; Wang and Mok 2008;). The V_s anisotropy of soils is usually evaluated by comparing the V_s in three orthogonal directions, i.e., V_{s-hh}, V_{s-hv}, and V_{s-vh}; where the first subscript letter denotes the direction of the shear wave propagation direction and the second subscript letter represents the direction of the soil particle vibration (v = vertical, and h= horizontal). The V_{s-hh}, V_{s-hv}, and V_{s-vh} are compared during loading and unloading stages which yields significant insight into the V_s anisotropy of soils.

In general, the anisotropic characteristics of soils are related to the applied stress, the inherent soil fabric, and the physiochemical conditions (ionic strength and pH, Kang et al. 2014). Stress anisotropy could cause V_s anisotropy of geomaterials composed of non-angular particles, such as round sand/spherical fly ash/glass beads (Stoke et al. 1985), because the V_s anisotropy of coarse grained soils is majorly dependent on the stress components in the direction of shear wave propagation and polarization, but relatively independent of the out-of-plane stress component. Due to geological sedimentation process or higher overburden stress (Bellotti et al. 1996), platy-clay particles often possessed preferential alignment which contributes to the fabric anisotropy, therefore, the V_{s-hh} is always higher than the V_{s-hv} and V_{s-vh} (Bellotti et al. 1996; Kang et al. 2014; Pennington et al. 1997). Anisotropic initial state of stress, interparticle contact orientation, stress history of the medium, micro-cracks inside the materials, inclusions, and laminated media could also contribute to the fabric anisotropy of clays, thus leads to the V_s anisotropy, i.e., K_0 consolidation induces preferential alignment of clay fabric in a direction that is normal to the applied loading (Kang et al. 2014; Santamarina and Cascante 1996; Santamarina et al. 2001; Wang and Mok 2008). Studies of stiffness anisotropy of organic matter modified clays indicated that the organoclays have inherent anisotropy and cross anisotropy, which are comparable to that of the inorganic soils (Choo et al. 2015). The preloading effect of organoclays was found to decrease with increasing of the total organic content (Choo et al. 2015), which is mainly due to the decrease of the permanent fabric change and the release of the lateral stress locking. Although organic polymers were found to influence the stress induced fabric anisotropy of clays, few studies have investigated the effects of polymers on the V_s

anisotropy of the fly ash-clay mixtures. Spherical particles (i.e., Fly ash) have less inherent anisotropy and less stress induced fabric anisotropy compared with plate-like particles (i.e., clay, Wang and Mok 2008). The V_s anisotropy of the organically fly ash-clay mixture, however, would be neither similar to organic clay, nor similar to coarse grained soil (fly ash), which would be largely dependent on the organic type, initial fabric, fly ash mixing ratios, and the associated stress states of the fly ash-clay mixture.

3. CHARACTERIZATION OF ORGANICALLY MODIFIED FLY ASH-KAOLINITE MIXTURES

3.1. INTRODUCTION

Owning to the chemically active surfaces of clays, polymers can extensively interact with the clay particles via polymer bridging, hydrogen bonding, and electrostatic forces (Israelachvili 2011; Theng 1982). The adsorption process is usually taken place with different functional groups at the surface of the long chains of polymers, as a result, the interparticle forces are altered by the polymer-clay-fly ash interactions, which lead to the rearrangement of clay particle associations, change of the microfabric, and eventually influence the macroscale soil properties (i.e., Atterberg limits, compressibility, stiffness, and strength). For example, positively charged polymers could neutralize the clay's negative surface charge (reflected by zeta potential) and compress the thickness of the diffuse double layer (DDL), which alter the interparticle forces and lead to the microfabric change (flocculation and aggregation) (Bate and Burns 2010; Kim and Palomino 2009; Nabzar et al. 1984).

The addition of organics to fly ash could also improve the strength properties by polymer bridging and electrostatic forces (Nath et al. 2009); however, the effects of polymers on the geotechnical properties of fly ash-soil mixtures are not well documented in the literature. Fly ash hydration could change the soil's pore fluid chemistry, which modifies the physicochemical properties of soil particles, breaks the balance of interparticle forces, and finally leads to the microfabric change (Ferguson 1993; Janz and Johansson 2002; Kang et al. 2013; Yeboah and Burns 2011). Mixing of polymers in soil could also induce flocculation and aggregation (Huang and Chen 1996; Kim and

Palomino 2009; Mpofu et al 2004). Therefore, the geotechnical properties such as friction, contact angles, wettability, compressibility, permeability, and strength, would be largely dependent on the flocculated and aggregated interconnected clay-water-polymer-fly ash network (Mitchell and Soga 2005; Nasser and James 2006; Nugent et al. 2010; Santamarina et al. 2001).

This chapter performs characterization of organically modified fly ash-kaolinite mixtures. Sedimentation tests were carried out in batches to screen out the potential polymers and optimum dosage in flocculation and aggregation (Kang et al. 2013). Three different organic agents, which include both biopolymers (Chitosan and Xanthan gum) and synthetic polymers (PEO), were selected to modify the fly ash-kaolinite mixtures. Theses selected polymers could reflect the influence of molecular weight, surface charge, and polymer type on the mechanical properties and microstructure of the organically modified soil. The microfabric, physicochemical properties, and engineering properties (include the particle size distribution, Atterberg limits, thermal conductivity, and dry unit weight) of the organically modified fly ash-kaolinite mixtures were characterized with scanning electron microscopy (SEM) test, electrical conductivity test, pH measurements, grain size distribution test, Atterberg limit test, thermal conductivity test, and proctor compaction test.

3.2. MATERIALS

Georgia kaolinite (RP-2, Active Minerals International) was used in this study. The grain size distribution curve of the Georgia kaolinite is shown in Figure 3-1. The kaolinite was an air-float processed clay, with a specific gravity G_s = 2.6 and an average aggregates diameter (d_{50}) of 0.0004 mm. Fly ash from Lafarge power plants, Wisconsin,

USA, was used in this study. The fly ash is classified as Class F (ASTM standard C 618) which has little self-cementious properties, thus. The grain size distribution curve of the fly ash is also shown in Figure 3-1, with an average diameter (d_{50}) of 0.028mm and specific gravity G_s = 2.7. Compared to kaolinite, the fly ash particles are 70 times larger whose particle sizes are in a range of silt (25%) to fine sand (75%). The chemical components of the fly ash and kaolinite are tabulated in Table 3-1. The major chemical components of kaolinite are Al_2O_3 (45.60%) and SiO_2 (38.40%). Large volume of amorphous chemical component (63.5%) was detected in the fly ash sample, and the aluminum oxide (Al_2O_3) and mullite ($Al_6Si_2O_{13}$) are the major crystal components.

Three polymers were selected to improve the strength of fly ash-kaolinite mixtures: Nonionic Polyethylene Oxide ($(-CH_2CH_2O-)_n$, PEO), positively-charged Chitosan **(**$(C_6H_{11}NO_4)_n$**)**, and negatively charged xanthan gum ($(C_{35}H_{49}O_{29})_n$)**.** Theses selected polymers reflected the influence of molecular weight, surface charge, and polymer type on the mechanical properties and microstructure of the organically modified soils. The chemical structures of the selected polymers are shown in Figure 3-2. PEO is perceived as a "flexible" polymer, with a structure described as a random coil and can change conformation dynamically in solution (Mpofu et al. 2004). The PEO polymer used in this research has a molecular weight (M.W.) of 600,000 g mol^{-1}. Chitosan is produced commercially by deacetylation of chitin, which is the structural element in the exoskeleton of crustaceans (such as crabs and shrimp) and cell walls of fungi. Chitosan adopted in this research has a M.W. of 100,000-300,000 g mol^{-1}. Xanthan gum is an anionic polysaccharide, derived from the bacterial coat of Xanthomonas campestris, which usually used as rheology modifier and soil conditioner.

The xanthan gum used in this research has a M.W. of 90,000-160,000 g mol^{-1}. All chemicals were purchased from Fisher Scientific, and were used as received.

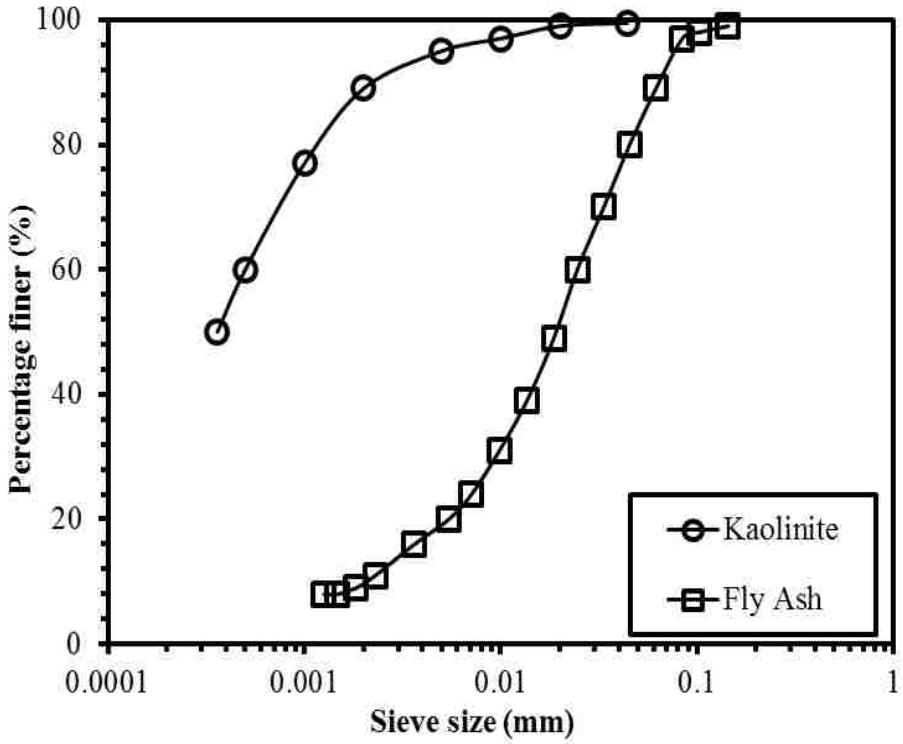

Figure 3-1 Grain size distributions of the kaolinite and fly ash.

3.3. METHODOLOGY

Scanning Electron Microscopy (SEM) test was performed on kaolinite, fly ash, and organically modified kaolinite and fly ash-kaolinite samples with SEM S-4700 (Hitachi Inc.). Sample surfaces were coated with a conductivity material, gold, using a sputter-coater (Hitachi E 1030) so as to increase the surface electrical conductivity and ensure high quality images. For each sample, four to six images were taken and compared, and then a representative image was reported.

Table 3-1 Chemical analysis results of RP-2 kaolinite and fly ash based on the X-Ray Diffraction (XRD) test

Kaolinite		**Fly Ash**		
Chemical Component	Percentage		Chemical Component	Percentage
SiO_2	45.60%	Crystal	Al_2O_3	16.2%
Al_2O_3	38.40%		SiO_2	6.4%
Fe_2O_3	0.88%		Fe_2O_3	3.9%
TiO_2	1.69%		$Al_6Si_2O_{13}$	10.1%
CaO	0.05%			
MgO	0.02%			
K_2O	0.15%	Amorphous		63.5%
Na_2O	0.21%			
LOI	13.70%			

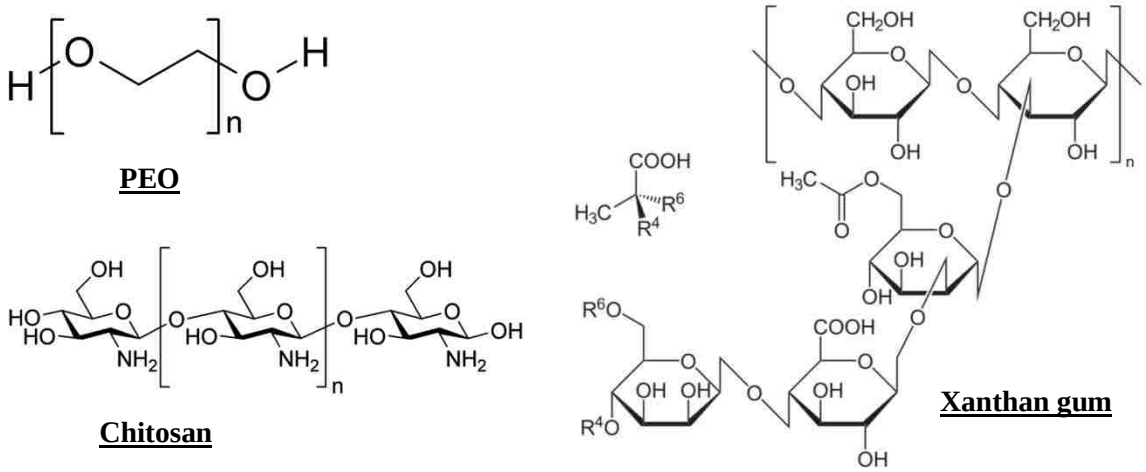

Figure 3-2 The chemical structures of PEO, Chitosan, and Xanthan gum.

Liquid limit (LL) tests were performed using the Casagrande cup method following the procedures specified in the ASTM standard D 4318 (ASTM 2006). The

tests were performed by adding a small amount of biopolymer solution to dry kaolinite powder and hand mixing the clay and biopolymer solution together until a homogenous paste was formed. Then the clay and biopolymer mixture was tested in a Casagrande cup. Some of the mixture in the Casagrande cup was used to measure the water content of the mixture, according to ASTM standard D 2216 (ASTM 2006). The Casagrande cup test was repeated, and four points were collected to determine each liquid limit.

Standard proctor compaction test was carried out on the organically treated soils in accordance with ASTM D 698. After the proctor compaction, thermal conductivity measurement was carried out immediately on the compacted samples with Decagon Devices KD2 Pro Thermal Properties Analyzer (Figure 3-3). The KD2 Pro Thermal Properties Analyzer consists of a handheld controller and sensors that can be inserted into subject soil specimen. A dual-needle SH-1 sensor was used to obtain all the thermal conductivity data in this study.

pH is the measurement of the acidity or basicity of an aqueous solution. Electrical conductivity is the measurement of a material's ability to accommodate the transport of an electric charge. In this study, all the pH and electrical conductivity measurements were conducted with the Accument Excel XL 60 Dual Channel pH/Ion/Conductivity/DO meter (Figure 3-3), purchased from Fisher Scientific. The room temperature was approximately at $24 \pm 2^0 C$.

3.4. RESULTS AND DISSCUSSIONS

3.4.1. Scanning Electron Microscopy (SEM) Images. Both the original fly ash particles and the broken fly ash particles are shown in Figures 3-4a and 3-4b. The fly ash particles are primarily in spherical shape with different diameters (Figure 3-4a). Small fly

ash particles are attached to large particles with the contact area varies significantly. The majority of the fly ash particles are smooth, while some large particles have irregular shapes. The broken fly ash particles indicated that most of the fly ash particles were cenospheres with hollow inside (Figure 3-4b). The shell thickness of the fly ash cenospheres is determined from a statistics analysis of the SEM images (i.e., Figure 3-4b) of the broken fly ash particles by assuming normal distribution.

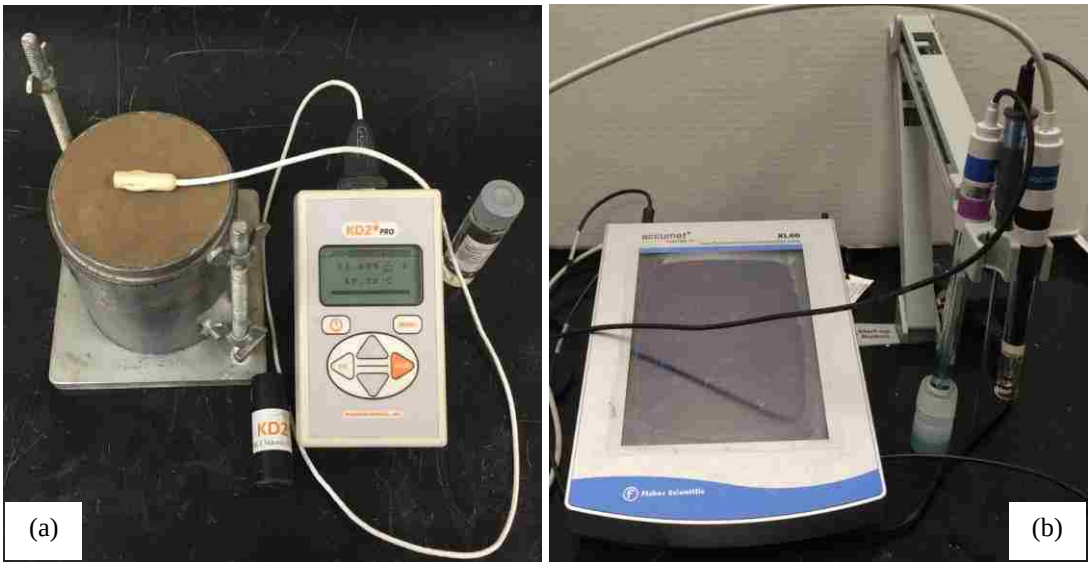

Figure 3-3 (a) Decagon Devices KD2 Pro thermal properties analyzer; (b) Accument excel XL 60 dual channel pH/Ion/Conductivity/DO meter.

The platy-shaped Georgia RP-2 kaolinite particles can be seen in Figure 3-4c, where kaolinite particles were randomly arranged with no observable fabrics.

SEM images of kaolinite treated by three different organic agents were presented in Figures 3-4d, 3-4e, and 3-4f. The polymer dosage were controlled at 1.0g/l for all the

specimens. Based on the test observation, PEO was found to induce higher degree of Face-to-Face (FF) aggregations to the kaolinite (Figure 3-4d). On the other hand, more Edge-to-Edge (EE) and Edge-to-Face (EF) particle associations were observed in both chitosan and xanthan gum treated kaolinite (Figures 3-4e and 3-4f). Compared with PEO induced aggregates, the xanthan gum and chitosan induced kaolinite aggregates are much smaller (indicated by the measurement bar).

SEM images of 30% fly ash + 70% kaolinite mixture, 60% fly ash + 40% kaolinite mixture, and 100% fly ash samples are shown in Figures 3-5a, 3-5b, and 3-5c. As fly ash mixing ratio increases, the contacts from kaolinite-to-kaolinite gradually shift to fly ash-to-kaolinite contact, and finally change to the fly ash-to-fly ash contact (fly ash particles were indicated by the red circles).

The SEM images of organically treated fly ash-kaolinite mixtures at a fixed ash to soil weight ratio of 30% to 70% were presented in Figures 3-5d to 3-5f. Compared with unmodified fly ash-kaolinite mixtures (see Figure 3-5d), the addition of the polymers have induced flocculation (EF) and aggregation (FF) to the soil and formed a dense microfabric (Figures 3-5d and 3-5e). In general, the fly ash particles are found surrounded by the polymer induced highly compacted kaolinite aggregates.

The organic polymers have induced a dense packing by interconnecting fly ash particles and kaolinite aggregates together. Owning to the large aggregates and dense microfabric induced by the addition of polymers, the geotechnical properties, such as shear strength, stiffness, and compressibility at macroscale, would be influenced correspondingly.

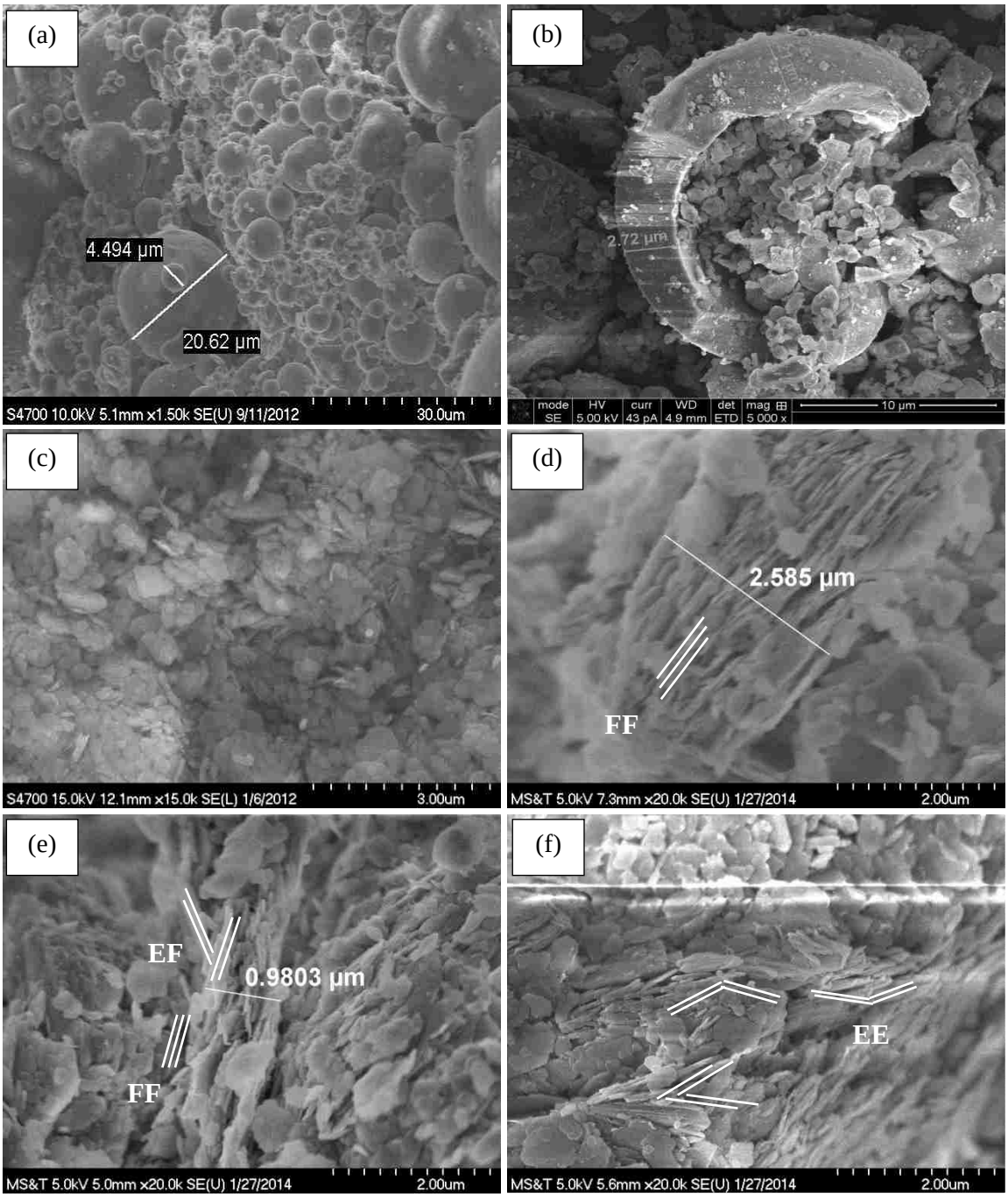

Figure 3-4 SEM images of (a) fly ash, (b) pulverized fly ash, (c) untreated kaolinite, and kaolinite treated by organic polymers (d) PEO, (e) Chitosan, and (e) Xanthan gum.

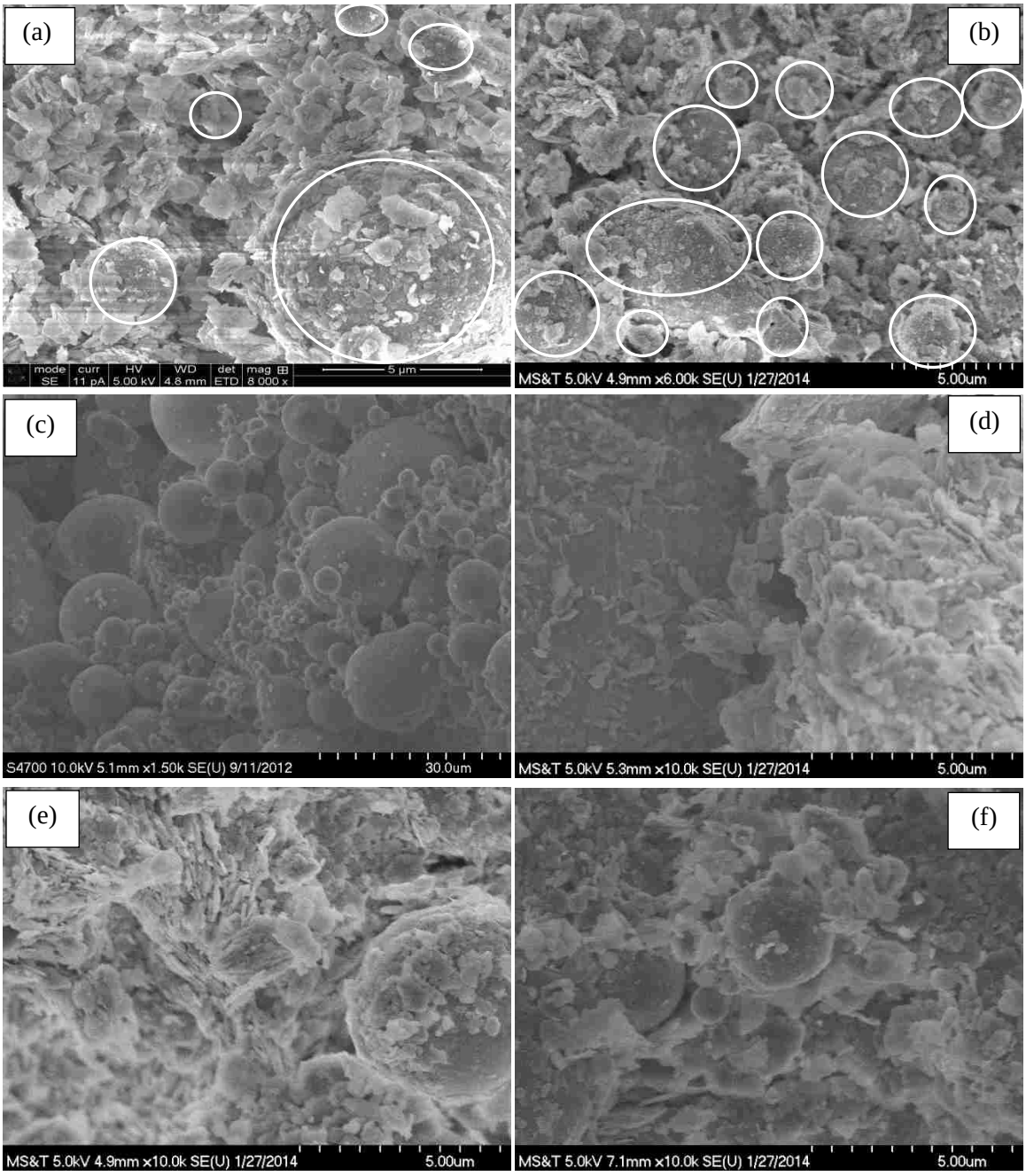

Figure 3-5 SEM images of organically modified fly ash soil mixtures; (a) 30% fly ash + 70 % kaolinite without organic agents, (b) 60% fly ash + 40% kaolinite without organic agents, (c) 100% fly ash without organic agents, (d) PEO modified 30% fly ash-kaolinite mixture, (e) chitosan modified 30% fly ash-kaolinite mixture, and xanthan gum modified 30% fly ash-kaolinite mixture.

3.4.2. pH and Electrical Conductivity. When fly ash is added to the soil, fly ash particles will react with the moist and start hydration. Figure 3-6 shows the electrical conductivity (ξ) change of the fly ash-water system with various fly ash contents. The electrical conductivity was found to increase as the fly ash content increased (Figure 3-6). After 200 g/l fly ash, however, the electrical conductivity of the system becomes almost constant.

During fly ash hydration, large amount of minerals such as lime (CaO), anhydrite ($CaSO_4$), Periclase (MgO), Quartz and Tricalciumaluminate would be dissolved, which increased the solution's electrical conductivity. Therefore, the electrical conductivity increased as the fly ash content increased initially (Figure 3-6). As the solution approaches to its saturation state, the speed of dissolution and precipitation of minerals gradually come to an equilibrium state, thus the curve flattens at high fly ash concentrations (Figure 3-6).

Hydrogen ions can easily dissociate from the carboxylic acid group on the surface of polymer chains and form a carboxylate anion in water, thus hydrated polymers normally positively or negatively charged. In this study, all three organic agents were found to increase the electrical conductivity of kaolinite, where the electrical conductivity was found to follow approximately a log-linear relationship with the polymer concentrations (as shown in Figure 3-7). The increase of the electrical conductivity indicates that the addition of polymers to soil could alter the pore-water chemistry. Furthermore, charge neutralization and polymer hydration might happen simultaneously, therefore, the electrical conductivity of the polymer modified kaolinite may vary and dependent on the types of organic polymers. For example, xanthan gum modified

kaolinite showed the highest electrical conductivity while PEO modified kaolinite exhibited the lowest conductivity under the same polymer dosage.

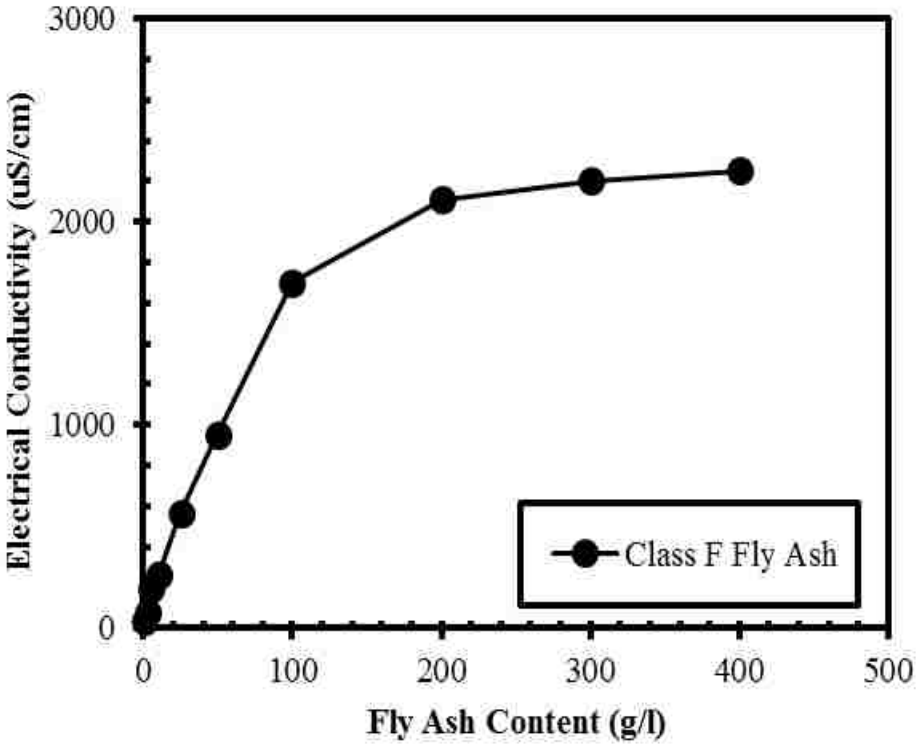

Figure 3-6 Fly ash content versus the electrolyte electrical conductivity.

In this study, all the pH measurements were conducted with the Accument Excel XL 60 Dual Channel pH/Ion/Conductivity/DO meter. The pH measurements of organically modified kaolinite solutions at various concentrations were illustrated in Figure 3-8. Except xanthan gum (acidic polymer) modified kaolinite, all the other organically modified soils were found to possess an alkalinity environment, and their pH slightly increased as the organic concentration increased.

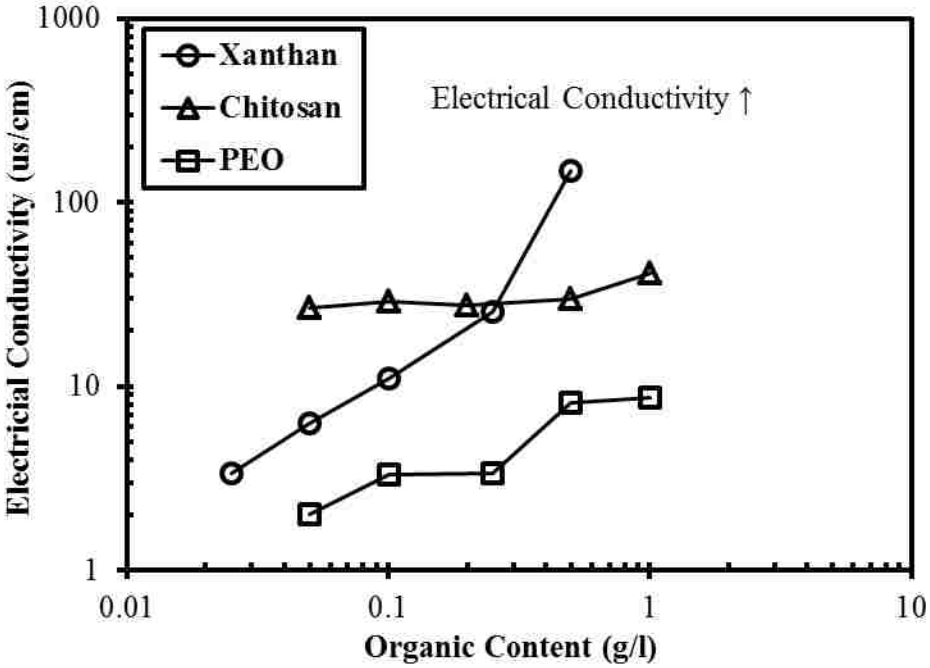

Figure 3-7 Electrical conductivity versus the organic concentration of different solutions.

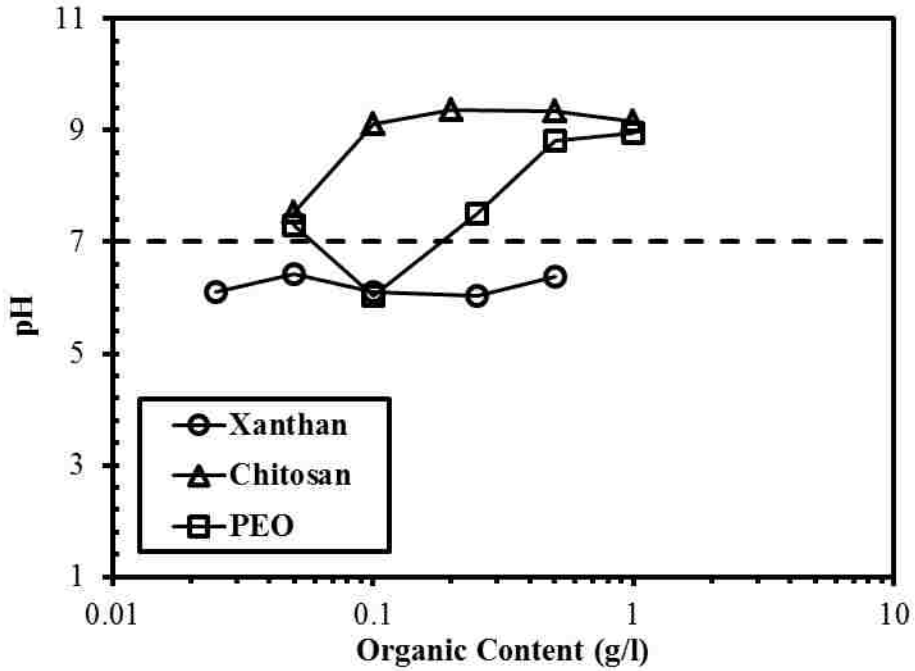

Figure 3-8 The relationship between measured pH and organic concentrations.

3.4.3. Atterberg Limits. The Atterberg limits change of fly ash - kaolinite mixtures are shown in Figure 3-9. In general, the addition of fly ash was found to reduce both the liquid limit and plastic limit of the fly ash-kaolinite mixtures, where the liquid limit and plasticity index continued to decrease as the fly ash content increased (Figure 3-9). This indicates that the fly ash is able to dry wet soils and provide an immediate strength gain, which is useful during construction in wet and unstable ground conditions. In addition, the fly ash could also reduce the swell potential of expansive soils by replacing some of the volume held by clay minerals and by compressing the double layers and changing soil gradations (Ferguson 1993). The liquid limit of the organically modified kaolinite was plotted in Figure 3-10. In general, the liquid limit of organically modified kaolinite increased as the polymer concentration increased. The liquid limit of pure kaolinite is approximately at 55.4 ± 1 (indicated by the shaded area in Figure 3-10). By adding xanthan gum, the liquid limit increased to about 58.8. Compared with xanthan gum, the liquid limit of PEO modified kaolinite only increased slightly. Although the liquid limit of Chitosan modified kaolinite fluctuated, it kept almost constant with the increase of chitosan concentrations (Figure 3-10).

The addition of fly ash could effectively reduce the liquid limit (LL), plastic limit (PL), and plastic index (PI) of the fly ash kaolinite mixtures. When fly ash is added to soil, the fly ash particles will absorb moist and start hydration. This process would release metallic ions into the pore fluid and increase the electrical conductivity the fly ash-soil-water system (Kang et al. 2013). Lower valence cations (H^+, Na^+ and K^+) would be replaced by higher valence cations (Ca^{2+}, Fe^{3+}, Al^{3+}) during the cation exchange process. The electrolyte concentration in the soil matrix is thus increased and the electrical diffuse

double layer at the kaolinite particle-liquid interface is compressed. The reduction of the thickness of the EDL promotes the kaolinite particles to flocculate. Flocculation results in a highly compacted and dense microfabric with lower void ratio and water content. At macro-scale, the liquid limit and plastic limit are decreased (Mitchell and Soga 2005).

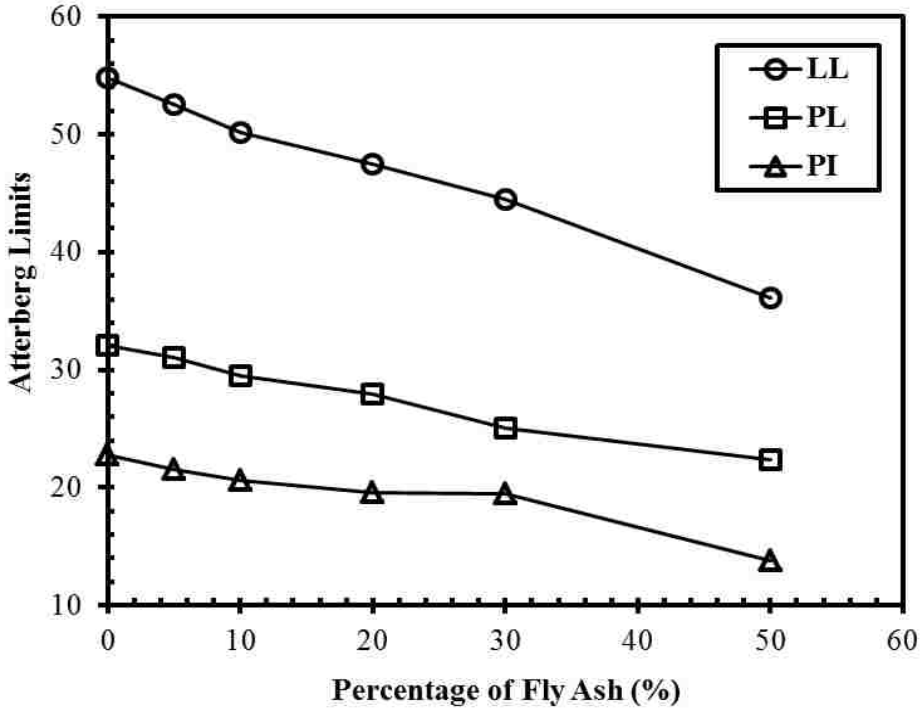

Figure 3-9 Liquid limit (LL), and Plastic Limit (PL), and Plasticity Index (PI) of fly ash-kaolinite mixtures at different fly ash mixing ratios.

Kaolinite has oxygen and hydroxide functional groups on the face surface. Both the oxygen and hydroxide on the kaolinite surface sites could form hydrogen bonds with organic polymers due to the effect of polymer bridging, where the long chains of the organic polymers would be adsorbed onto several adjacent particles simultaneously, and

creating highly linked clay-polymer network with three-dimensional void spaces between polymers and clay particles (Podsiadlo et al. 2007). The formation of highly linked clay-polymer network will result in large open pores between the kaolinite aggregates (Figure 3-5), where more free water might be trapped in, thus lead to a slightly increase of the liquid limit (Figure 3-10).

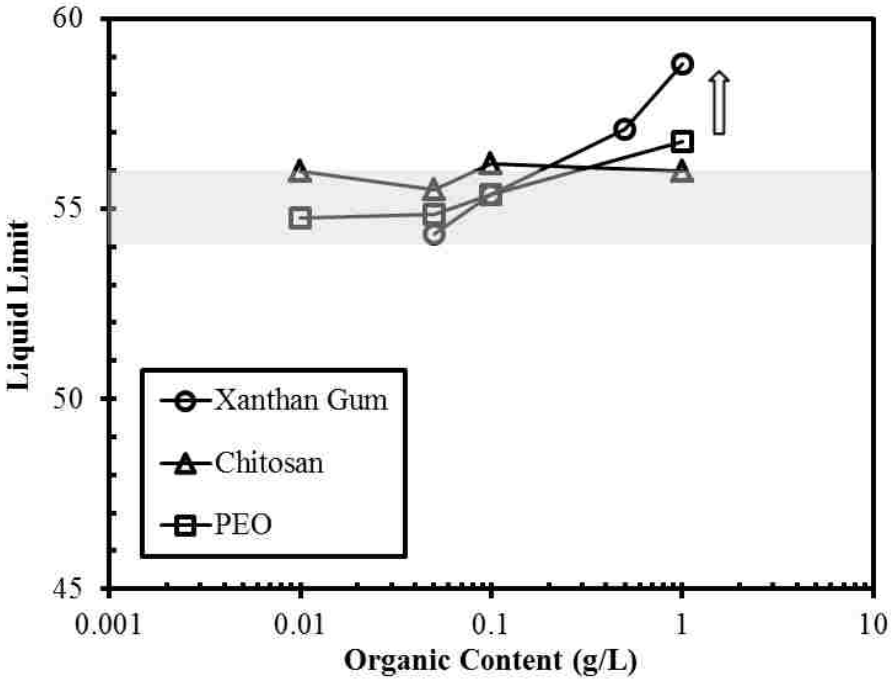

Figure 3-10 Liquid limit of kaolinite at different organic concentrations.

3.4.4. Proctor Compaction Characteristics and Thermal Conductivity. Standard proctor compaction tests were carried out on PEO and Xanthan gum modified kaolinite and fly ash-kaolinite mixtures and the results are presented in Figures 3-11 and 3-12. Pure kaolinite samples exhibited relatively low dry density compared with 30% fly ash-kaolinite mixtures. Based on the proctor compaction curves, the optimum water

content of kaolinite and 30% fly ash-kaolinite mixtures are determined, which are 29.5 % and 23.0 %, respectively.

Thermal conductivity, κ, is the property of a material to conduct heat. Figure 3-11b shows the correlation between thermal conductivity and water content of the compacted specimens. Compared with the proctor compaction curves, the thermal conductivity data also exhibited the same trend ("backbone"), where there is an optimum water content at which the thermal conductivity showed its maximum value. However, the optimum water content obtained from the thermal conductivity data of kaolinite and 30% fly ash kaolinite mixtures were slightly lower than that of optimum water content obtained from standard proctor compaction test, which are 27% and 21%, respectively.

Different amount of PEO and Xanthan gum polymers were added to kaolinite and 30% fly ash-kaolinite mixtures which prepared at the optimum water content condition and compacted under the standard proctor compaction energy. By adding the organic polymers, the dry unit weight was found to increase as PEO and Xanthan gum was added (Figure 3-12a). However, as the organic dosage passed over 0.1 wt.%, the measured dry unit weight began to decrease as the organic content increased. Similarly, a "back bone" trend was found for the measured thermal conductivity of organically modified fly ash-kaolinite mixtures as shown in Figure 3-12b. For the organically modified kaolinite, however, the thermal conductivity decreased as the organic content increased.

3.5. SUMMARY

Organic polymers, which include polyethylene oxide (PEO), xanthan gum and chitosan, were used to modify the kaolinite and fly ash-kaolinite mixtures in this study. The geotechnical properties such as the grain size distribution, Atterberg limits, pH and

electrical conductivity, moisture density relationship, and thermal conductivity of the organically modified kaolinite and fly ash-kaolinite mixtures were investigated. Based on the experimental results, the following conclusions could be drawn:

(1) The microfabric of polymer modified kaolinite and 30% fly ash-kaolinite mixtures was clearly seen under the SEM. PEO and chitosan were found to induce flocculation (EF) and aggregation (FF) to the kaolinite while xanthan gum was found to de-flocculate the soil fabric and disperse kaolinite particles away from each other.

(2) The addition of fly ash could largely reduce the liquid limit and plastic limit of kaolinite, which would in turn result in a decrease of the PI. Organic agents, such as xanthan gum was found to increase the liquid limit of kaolinite, however, the liquid limit only increased slightly for PEO and Chitosan modified soils.

(3) The addition of fly ash was found to increase the maximum dry unit weight but decrease the optimum water content of kaolinite. Polymers slightly increased the dry unit weight of both kaolinite and the mixture at lower concentration (< 0.1%), however, the dry unit weight decreased as the organic content increased further (> 0.2%).

(4) The thermal conductivity of kaolinite and fly ash kaolinite mixtures was reduced by the addition of fly ash and organic polymers.

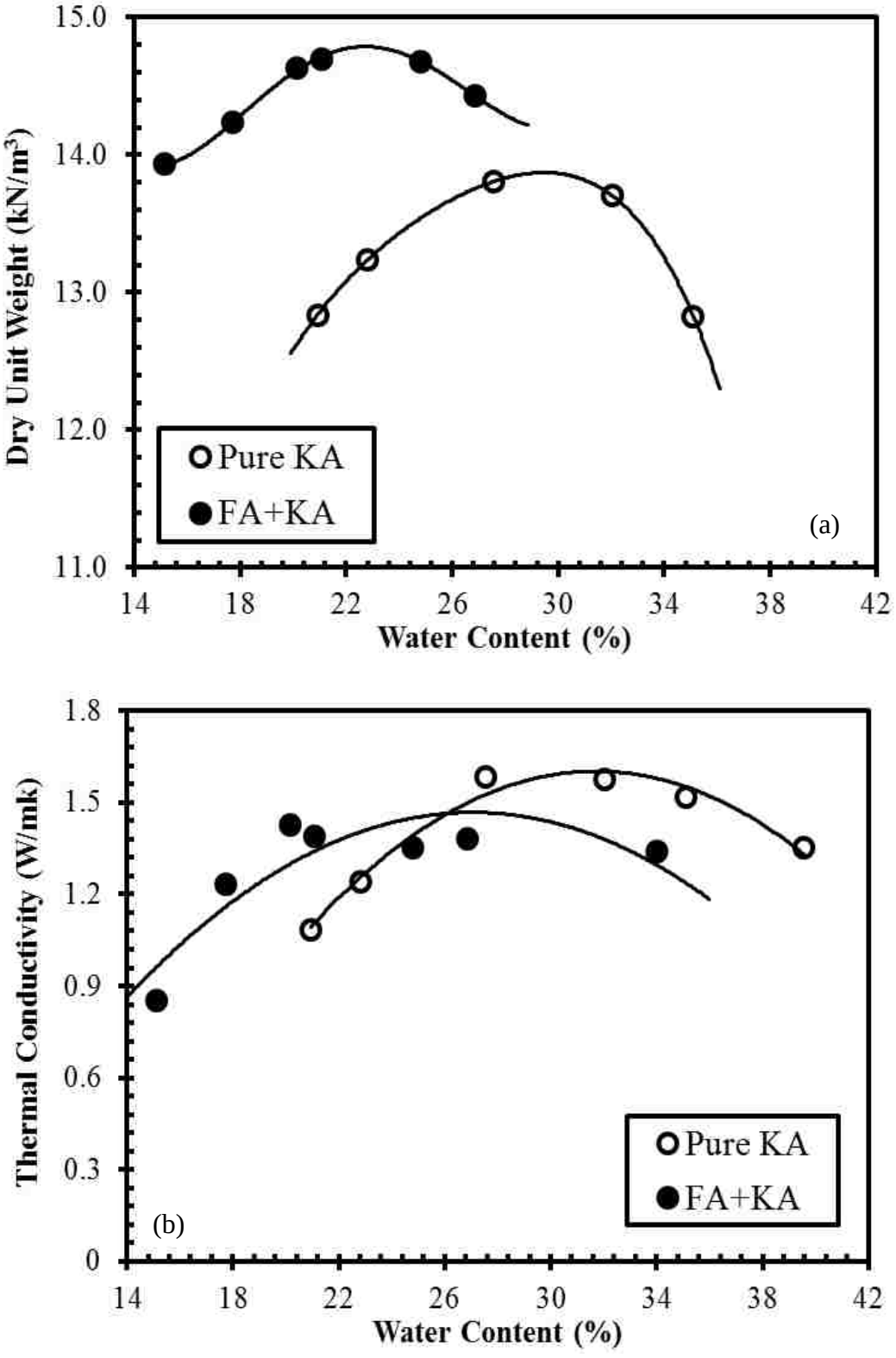

Figure 3-11 (a) Proctor compaction curves of kaolinite and fly Ash (30 %)-kaolinite (70 %) mixtures; (b) Thermal conductivity versus water contents of kaolinite and fly ash (30 %)-kaolinite (70 %) mixtures.

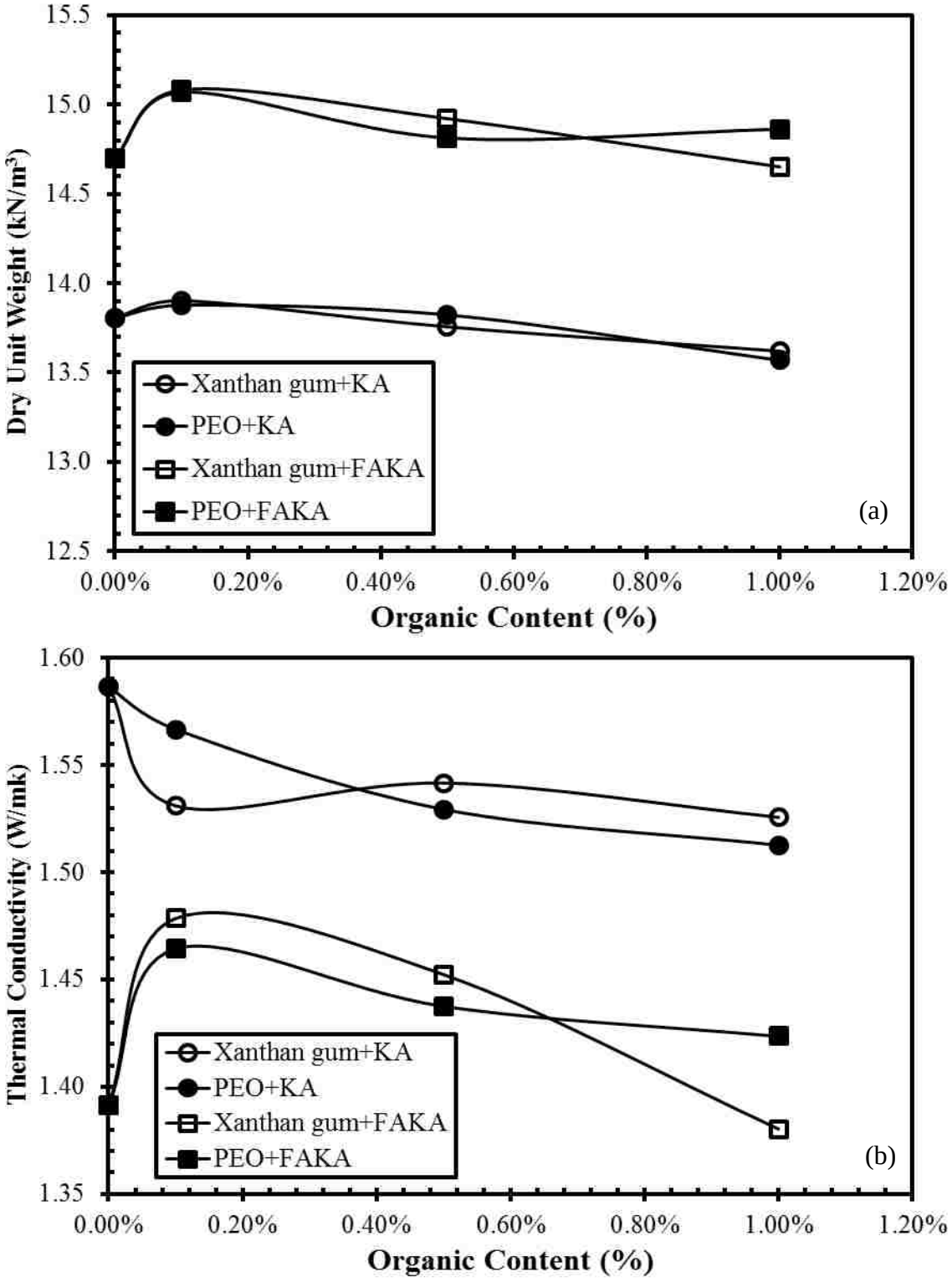

Figure 3-12 (a) dry unit weight versus organic content (b) thermal conductivity versus organic content of kaolinite and fly ash (30%)-kaolinite (70%) mixtures under the standard proctor compaction effort.

4. MEASUREMENT OF STIFFNESS ANISOTROPY IN KAOLINITE USING BENDER ELEMENT TESTS IN A FLOATING WALL CONSOLIDOMETER

4.1. INTRODUCTION

Small strain stiffness of geomaterials is an important design parameter for geotechnical structures subjected to dynamic loadings, such as earthquake; pile driving, traffic, machine vibrations, and wind. Small strain stiffness of a soil can be quantified by the initial shear modulus (G_{max}), which can be related to shear wave velocity by $G_{max} = \rho V_s^2$, where ρ is the bulk soil density.

The stiffness of soils, in terms of shear wave velocity, is often anisotropic due to two main factors. The first factor is the preferential alignment of the angular soil particles due to geological sedimentation process or higher overburden stress (Bellotti et al. 1996; Jiang et al. 1997), or fabric anisotropy. The second factor is stress anisotropy, where the three principal effective stresses of a soil element are not equal. It was found that only stresses on the plane of wave propagation and particle vibration had significant effects on shear wave velocity (Allen and Stokoe 1982; Knox et al. 1982; Lee and Stokoe 1986; Ni 1987; Roesler 1979; Wang and Mok 2008; Yu and Richart 1984). This plane is termed a polarization plane (Santamarina et al. 2001), which is denoted by two letters, v and h, with the first letter indicating wave propagation direction, and the second letter indicating particle vibration direction. Given other factors equal, higher mean effective stress on the polarization plane generally leads to higher shear wave velocity of the geomaterials (Lee et al. 2008; Santamarina et al. 2001). Geomaterials composed of non-angular particles, such as round sand, can also be anisotropic due to stress anisotropy. Although stress anisotropy depends only on the stress state of the soil, anisotropic loading could cause

fabric anisotropy. For example, anisotropic K_0-consolidation induces preferential alignment of clay fabric in a direction that is normal to the applied loading (Santamarina et al. 2001). This is termed stress-induced fabric anisotropy (Santamarina et al. 2001). Furthermore, Lee et al. (2008) observed that higher consolidation pressure led to more apparent V_s anisotropy. However, few high pressure (> 400 kPa) experimental results of V_s anisotropy are available in the literature (Fam and Santamarina 1995; Fam and Santamarina 1997; Jovicic and Coop 1998; Piriyakul 2006). This is partially due to equipment limitations, as excess soil deformation under high pressure damages bender elements in a conventional fixed ring consolidometer (Bate et al. 2013). Installing bender element in a triaxial testing setup has the advantage of being able to apply complicated stress paths, pore water and pore air pressures. Therefore it was widely used in recent decade (Ezaoui and Di Benedetto 2009; Fioravante and Capoferri 2001; Leong et al. 2009; Marjanovic and Germaine 2013). However, bender element testing in a triaxial sample has several disadvantages for evaluating stiffness anisotropy of a soil. (i) The installation of horizontal bender element is not easy. To circumvent installing horizontal bender elements, a single pair bender element (top and bottom) installation in a triaxial testing setup was used to measure V_s anisotropy. Three cylindrical triaxial samples, cut from a large anisotropically consolidated soil sample in three orthogonal directions (Jovicic and Coop 1998; Wang and Siu 2006), will be tested individually, which prevents concurrent monitoring of stiffness evolution, and requires more time and materials for sample preparation. (ii) In addition, due to the height of a triaxial test sample is often twice the size of the diameter, faster P-wave could bounced off sample side and reach to the end receiving bender element earlier than S-wave. This makes accurate determination

of the first arrival time of S-wave difficult (Marjanovic and Germaine 2013) . (iii) Frictional bender element technique was used to overcome the difficulties of installing horizontal bender elements in a triaxial soil sample (Fioravante and Capoferri 2001; Piriyakul 2006). However, this technique inevitably introduces P-wave transmitting directly to the receiving bender due to the unrestrained BE vibration. (iv) In addition, R_d ratio, the ratio between wave transmitting distance and wave length, for horizontally transmitting shear waves is constrained by the limited diameter size of a triaxial sample, which is usually 3.56 cm (1.4 inch) or 7.11 cm (2.8 inch). This could lead to less optimal quality signals.

Salt type and concentration have significant effects on the geotechnical properties of fine-grained soils (Bate and Burns 2010; Mitchell and Soga 2005; Santamarina et al. 2001). Studies have been made of the effects of salt type and concentration on swelling/compressibility (Arasan et al. 2010; Di Maio 1996; Di Maio 1998), consolidation (Di Maio 1996; Di Maio 1998; Gajo and Maines 2007), and shear strength (Bate et al. 2013; Di Maio and Fenelli 1994; Mesri and Olson 1970; Moore and Mitchell 1974). However, few studies on the effects of salt type and concentration on soil stiffness and its anisotropy are available in the literature.

The objectives of this research are to: (1) Design and manufacture a new floating wall consolidometer-type bender element testing system to measure shear wave velocity in three orthogonal directions, i.e., vh, hv, and hh, at high stresses. (2) Investigate the stress-induced fabric anisotropy during K_0 consolidation that affects the anisotropic V_s properties of kaolinite samples at applied vertical pressure up to 800 kPa. In addition,

effect of salt concentration on V_s anisotropy will be tested by using high (1 mol/l) and low (0.005 mol/l) NaCl solutions as bulk fluid.

4.2. DESIGN OF THE FLOATING WALL CONSOLIDOMETER-TYPE BENDER ELEMENT TESTING SYSTEM

The floating wall consolidometer bender element testing system consists of a floating wall consolidometer with its cell placed inside a fluid chamber, three pairs of bender elements, and the accompanying signal generation and sampling system (Figure 4-1). Details of each component will be elaborated below.

4.2.1. Bender Element. The bender element in this study was made from piezoceramic plates (Piezo Systems, Inc.). The piezoceramic plate was cut to dimensions of 12.7 × 8.0 × 0.6 mm (length × width × thickness). A parallel-type connection was adopted to minimize the electronic coupling between the source and the receiver, and could generate stronger signal than series-type connection (Lee and Santamarina 2005). The piezoceramic plate was directly connected to a coaxial cable, coated with polyurethane as the electrical isolator and moisture shield, electrically shielded with conductive paint, and grounded to the floating wall that was submerged into the salt solution in the chamber (Figure 4-1).

The tip of the bender element was extended 5 mm from the nylon screw (for vertical BE) or socket (for horizontal BE) (Subset b in Figure 4-1). Great care was taken while coating to obtain a casing free from open seams, cracks, and air bubbles. The details of the bender element design and manufacturing, including the wiring of the electric connections, water proofing, housing into soil specimens through the side walls of the floating wall and grounding could be found in the literature (Lee and Santamarina 2005).

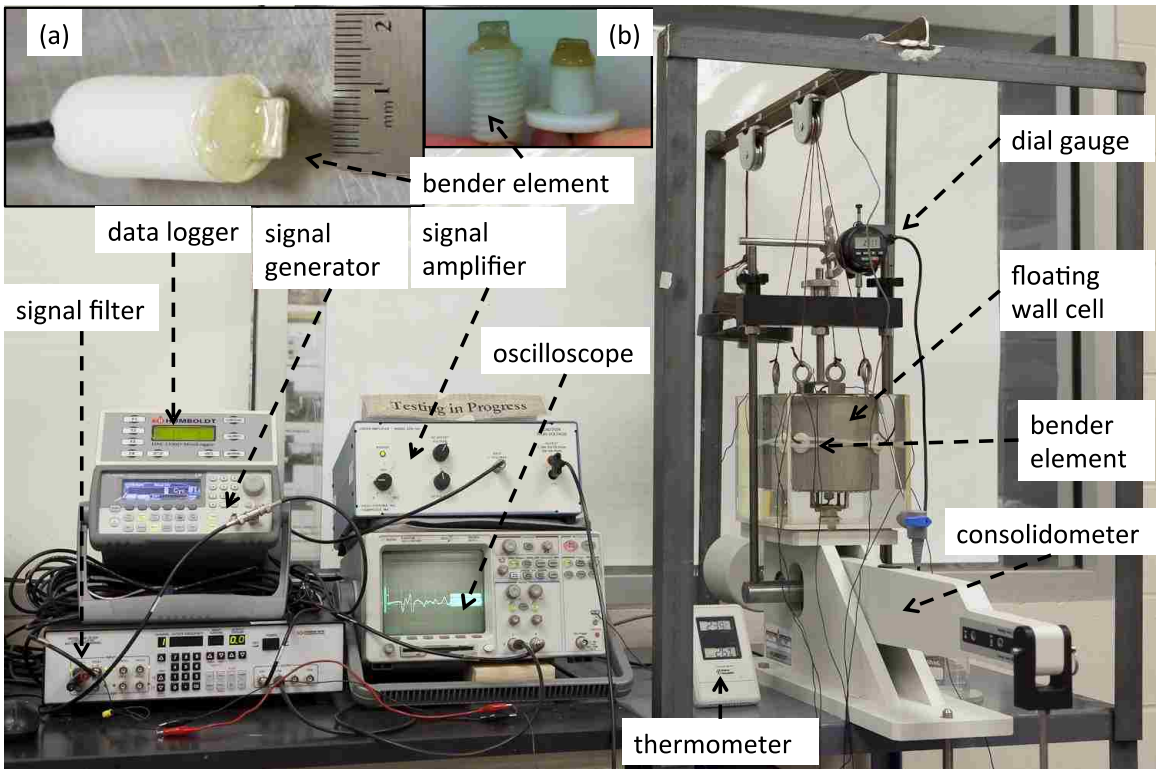

Figure 4-1 Floating wall consolidometer-type bender element testing system. Subset (a) newly-made vertical bender element. (b) vertical (left) and horizontal (right) bender elements after five tests.

4.2.2. Floating Wall Consolidometer Cell Design. A bender element installed horizontally on the sidewall in a traditional fixed ring consolidometer was subjected to a large bending moment (Figure 4-2), which was induced by excessive settlement of the soil, especially fine-grained soil (Bate et al. 2013). In this study, a floating wall consolidometer cell (Figures 4-1 and 4-3) was adopted to eliminate the detrimental bending moment imposed upon the benders installed on the sidewall. When vertical loading was applied, both the top and bottom platens moved symmetrically toward the midsection of the wall, where the horizontal bender elements were installed (Figure 4-2a) (more in Discussion). This effectively reduced the bending moment so that the reaction

on the benders was negligible. Counter weights, through a pulley system, were used to prevent the bending moment on the horizontal bender elements by the self-weight (5.2 kg) of the stainless steel floating wall (Figure 4-1). The floating wall served as a confinement ring so that the K_0 condition of the soil was maintained. The inner diameter of the consolidometer cell was 11.4 cm (4.5 in), and the height was 12.7 cm (5 in). The thickness of the wall was 1.3 cm (0.5 in). The wall and the top and bottom platens were made of type 304 stainless steel, which can withstand the corrosive environment of a high salt concentration and an extreme pH condition.

A pair of bender elements was screwed in vertically in the center of the top and bottom platens (vh direction). A U-shaped steel (Figures 4-1 and 4-3) was used to house the benders, and to transfer the vertical load. Four horizontal bender elements were pushed into the sample through the predrilled holes on the sidewall, 90 degrees apart, on the midsection of the floating wall (Figure 4-3). One pair of the horizontal bender elements, facing each other, was aligned parallel to the horizontal direction (hv direction), while another pair was aligned vertically (hh direction). Wall thickness of 1.3 cm (0.5 in) guaranteed the alignment of the benders.

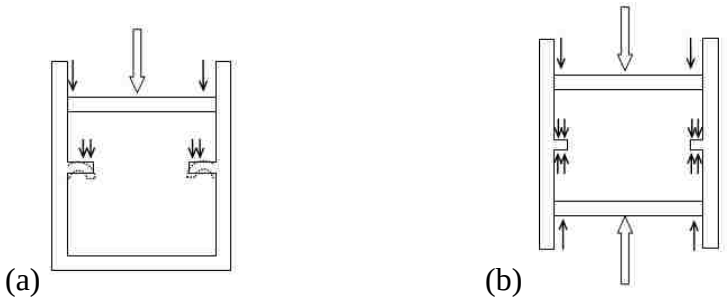

Figure 4-2 Soil deformation-induced bending moment on horizontal bender elements in a) a fixed wall consolidometer and b) a floating wall consolidometer.

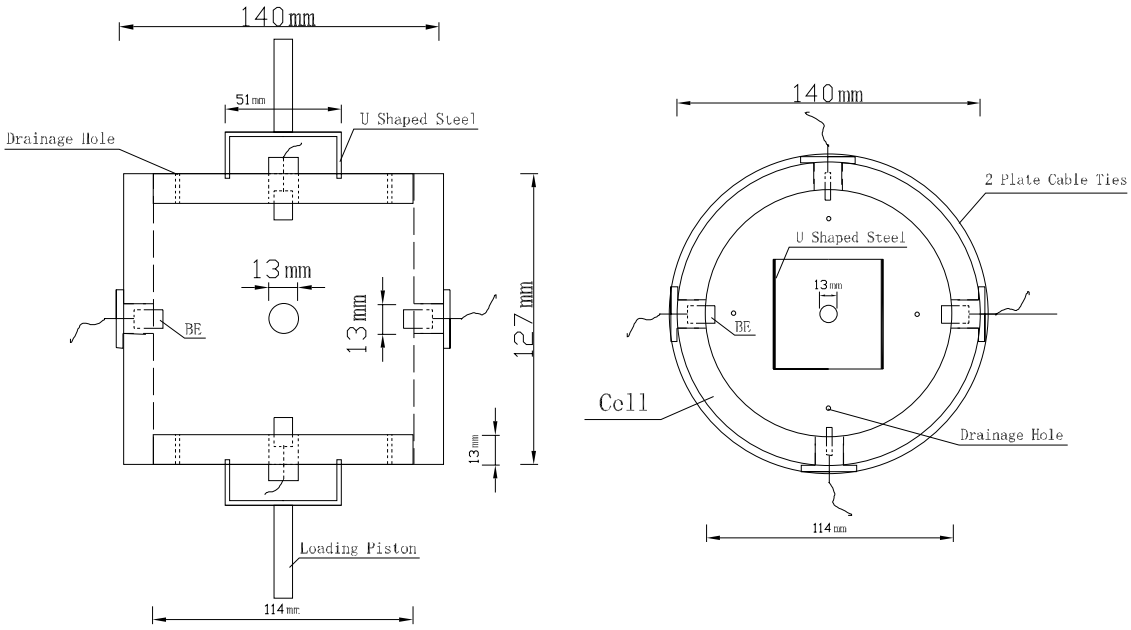

Figure 4-3 Schematic setup of the floating wall consolidometer cell. Left: side view, right: top view.

4.2.3. Chamber Controlling the Bulk Environment. The floating wall type consolidometer bender element device was completely submerged in a chamber during operation (Figure 4-1). It maintains saturation of the sample, and controls the physicochemical conditions of the bulk fluid, including pH, temperature, and salt concentration.

4.2.4. Signal Generation, Filtering, and Data Acquisition System. Signal generation, filtering, and the data acquisition system consist of a function/arbitrary waveform generator (33210A, Agilent), a filter/signal conditioner (3364, Krohn-Hite), and an oscilloscope (54622A, Agilent). The transmitter bender was excited by a single cycle sine wave with a frequency ranging from 2 – 10 kHz, and amplitude of 10 V by the function generator. Frequency was adjusted to obtain stronger responses and lower

noises. The receiver bender was connected to the filter, which was connected to the oscilloscope with a sampling rate of 2000 data points.

4.2.5. Excitation Frequency, First Arrival Time, and Travel Distance. The selection of an input signal frequency was subject to the following considerations. Jovicic et al. (1996) and Kawaguchi et al. (2001) reported that the shear wave response was enhanced if the frequency of the input sine signal approached the resonant frequency of the bender element-soil system. The first arrival was not affected by the excitation frequency; however, the ability to detect the arrival time can change dramatically (Lee and Santamarina, 2005). The near-field waves affected the shape of the receiver signal and caused uncertainty in determining the arrival of shear waves in the bender element tests (Brignoli et al. 1996; Jovicic et al. 1996; Viggiani and Atkinson 1995). A ratio, $R_d = L_i / \lambda_i$ (l_i is the distance between the sender and receiver bender elements; λ_i is the wave length), that can be used to assess the degree of attenuation due to geometric damping, was introduced by Sanchez-Salinero et al. (1986). Using sufficiently high frequency could reduce the near field effect (Jovicic et al. 1996; Leong et al. 2005; Pennington et al. 2001; Sanchez-Salinero et al. 1986). Different input frequencies were used in this study, and the frequency corresponding to an Rd value of slightly larger than 2.0 yielded the best quality signals. It is worth noting that the stiffness (shear wave velocity) changed at different loads, so the input frequency varied as well.

There are several different interpretations of the first arrival time, such as cross correlation method in frequency domain, peak-to-peak and start-to-start method in time domain (Arulnathan et al. 1998; Jovicic et al. 1996; Lee 2003; Leong et al. 2005; Pennington et al. 2001; Yamashita et al. 2009), and the "half peak" interpretation (Lee

and Santamarina 2005; Viggiani and Atkinson 1995). In "half peak" method the first arrival time was between points b and c of the half peak, before the first major peak of the received signal (Figure 4-4) (Lee and Santamarina, 2005). In this study, the first arrival time was manually picked at the first zero-crossing of the first major peak (point c in Figure 4-4) by cursor function in Math CAD (PTC, Needham, MA). This could lead to a slight underestimation of V_s (Viggiani and Atkinson 1995). Different travel distance between sender and receiver was used in the literature, such as base to base, mid-section to mid-section, and tip to tip distance (Dyvik and Madshus 1985; Fernandez 2000; Kim and Kim 2010; Viggiani and Atkinson 1995). In this study, tip-to-tip distance was selected as the shear wave propagation distance.

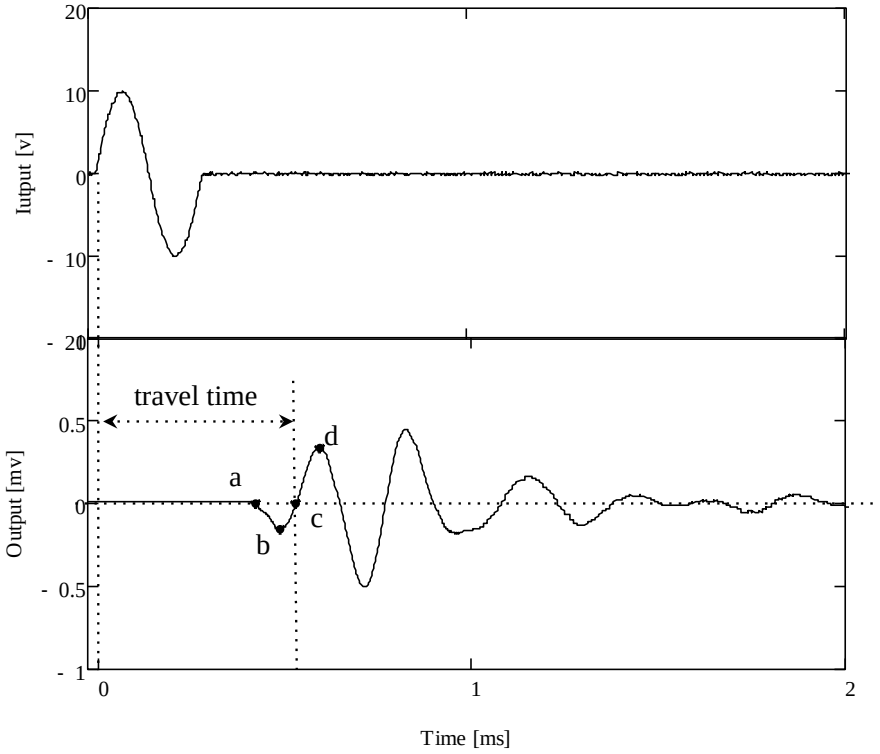

Figure 4-4 Determination of the first arrival time using single cycle sine wave as the input function.

4.3. MATERIALS AND EXPERIMENTAL METHODS

4.3.1. Materials. Georgia kaolinite (RP-2, Active Minerals International) was used in this study. The grain size distribution curve and the properties of Georgia kaolinite were shown in Figure 4-5 and Table 4-1, respectively.

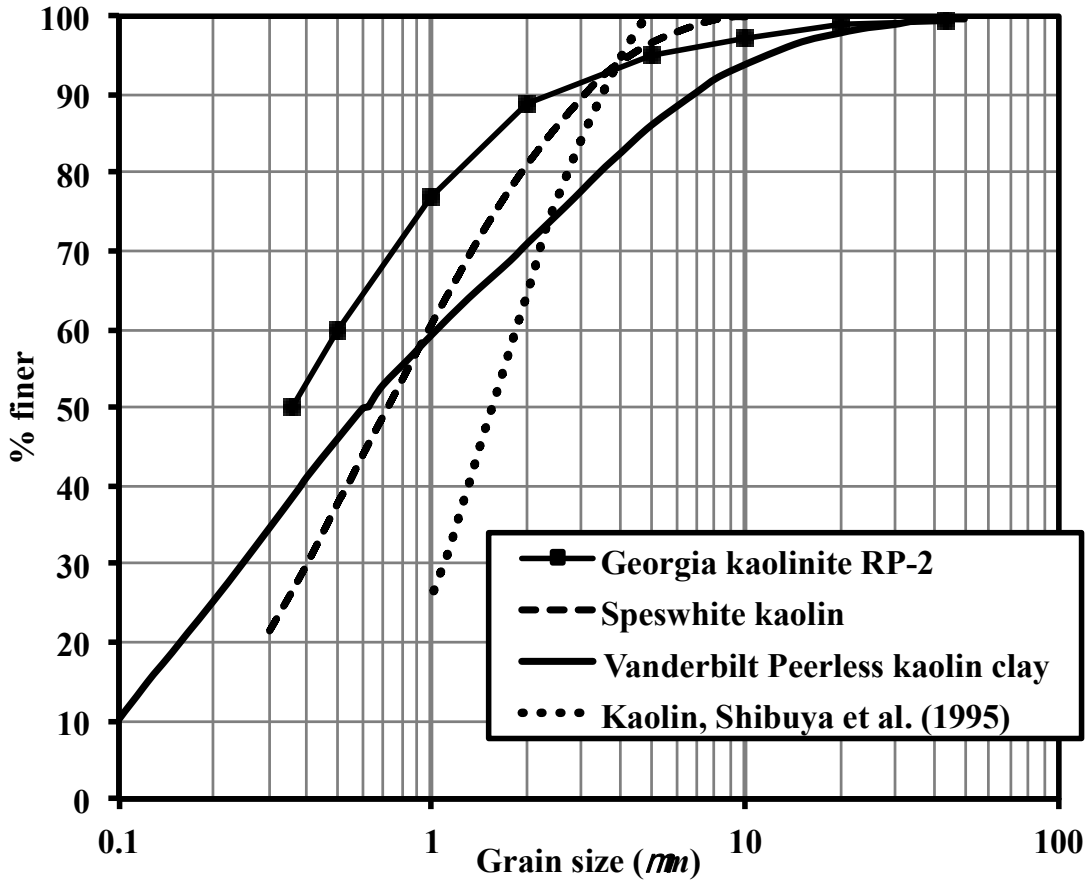

Figure 4-5 Grain size distribution curves for Georgia kaolinite RP-2 (Active Minerals International, Hunt Valley, MD, USA, 2007) used in this study; Speswhite kaolin (Imerys Performance & Filtration Minerals, Cornwall, UK, 2008) used in Wang and Siu (2006), Viggiani and Atkinson (1995) and Jovicic and Coop (1998); Vanderbilt Peerless kaolin clay (R.T. Vanderbilt Company, Inc., Norwalk, CT, USA, 2011) used in Fam and Santamarina (1997) Fam and Santamarina (1995), and kaolin used in Shibuya et al. (1995).

Table 4-1 Comparison of the properties of kaolinites used in different studies

	Chang et al. (2006)	Fam and Santamarina (1995)	Fam and Santamarina (1997)	Wang and Siu (2006)	Jovicic and Coop (1998)	Viggiani and Atkinson (1995)	Meng (2003)	Shibuya et al. (1995)	This study
Soil type	-	kaolinite	kaolinite	kaolin	reconstituted kaolin	kaolin	pure kaolin	kaolin	Georgia kaolinite
Source	-	Vanderbilt Co., Los Angles, CA, USA	Vanderbilt Co., Los Angeles, CA, USA	Imerys Minerals Ltd., UK	-	-	-	-	Active Minerals International, Hunt Valley, MD, USA
Trade name	-	Peerless clay	Peerless clay	Speswhite kaolin	Speswhite kaolin	Speswhite kaolin	-	-	ACTI-MIN RP-2
Color	-	light cream	light cream	-	-	-	-	-	cream
Specific gravity	-	2.6	2.6	2.6	2.6*		-	2.78	2.6***
Liquid limit	-	50	50	57.9(pH5)	-	-	67	40	54.8
Plastic limit	-	35	35	29.7(pH5)	-	-	33	24	32.1
Main cation	-	Sodium	-	-	-	-	-	-	Sodium
CEC (mequiv./100 g)	-	20-30	20-30	-	-	-	-	-	-
pH	-	4.8 (10% solids)	4.8 (10% solids)	5.0 +/- 0.5	-	-	-	-	neutral
Conductivity (mS/cm)	-	0.04 (10% solids)	-	-	-	-	-	-	0.07 (10% solids)
d50 (micron)	-	0.62**		0.72 (from GSD curve)*			-	1.4 (from GSD curve)	0.36***
Surface area, m2/g	-	-	-	14	14*		-	-	22 - 35****
Max moisture content (mass %)	-	-	-		1.5%*		-	-	1%***
Oil absorption (ASTM D 281) (g/100g clay)	-	30**			42*		-	-	40***
Slurry consolidation pressure (kPa)	-	50	-	100	70	-	173 - 483	150	100
Vertical effective stress (K0 loading) (kPa)	0 - 46.2	0 - 610	0 - 610	-	-	-	-	-	0 - 800
Mean effective stress (triaxial loading) (kPa)	-	70 - 140	-	0 - 250	0 - 600	0 - 400	173 - 483	300	-
Void ratio	2.54 - 1.51	-	1.57 - 0.94	1.599 - 1.075	-	-	1.15 - 1.04	1.336 - 1.076	1.278 - 0.933
Compression index, Cc	-	-	0.46		-	-	-	-	0.49 (0.005 mol/l); 0.38 (1 mol/l)
Critical state effective friction angle (degree)	-	-	25 +/- 5	27.5	-	-	-	-	19.8
Testing technique	BE	BE	BE	RC	RC	BE	RC	Torsional shear	BE

* from Speswhite data sheet, Imerys Performance & Filtration Minerals (2008)

** from Kaolin clay data sheet, R.T. Vanderbilt Company, Inc. (2011)

*** from ACTI-MIN RP-2 data sheet, Active Minerals International (2007)

**** from Santamarina et al. (2002)

4.3.2. Sample Preparation. Kaolinite samples were first mixed with 1 mol/l NaCl solution at a solid to solution weight ratio of approximately 1:10. The mixture was then thoroughly mixed manually and left to stand for 24 hours to allow hydration of kaolinite particles. For 0.005 mol/l sample, the supernatant was siphoned out, and the slurry was diluted with de-ionized water. This procedure was repeated until the electrical conductivity of the supernatant reached a value close to the electrical conductivity of 0.005 mol/l NaCl solution ($474.1\ \mu s/cm$) (Bate 2010). 1 mol/l sample was not diluted.

Then the slurry was carefully poured into an aluminum consolidation tube with top and bottom drains and the dimension of 45.7 x 11.7 cm (18 x 4.5 in) (height x diameter). Care was taken not to entrap air by pouring slowly and contacting slurry to the side of the tube. The slurry was one-dimensionally consolidated with similar procedures described in Bate et al. (2013). Axial load was placed on the slurry in load steps of 7, 14, 28, 62, 100, 62, 28, 14, and 7 kPa. End of primary consolidation was reached (judged by Taylor's method) at each load step. P5 filter paper (Fisher Scientific) and a nonwoven geotextile were placed on the top and bottom of the sample to facilitate drainage. The bulk solution was drained from the top and bottom. The salt concentration of the pore fluid was maintained by submerging the outlets in the NaCl solution at the same concentration as the predetermined concentration of the slurry. After the slurry consolidated, the soil sample was extruded from the consolidation tube, wrapped with food-wrap, placed in two zip lock bags, then in a sealed PVC container, and stored in a moisture room until used. Typical height of the soil samples after slurry consolidation ranged from 12.7 to 17.8 cm (5 – 6 in).

To install the soil sample in the floating wall bender element cell, the following steps were followed. 1). The pair of bender elements were screwed in the top and bottom platens. 2). The soil sample was carefully pushed into the cell wall using a flat round surface to avoid deformation of the soil sample. Polished inner wall of the cell and vacuum grease was adopted to reduce the friction. 3). The cell was mounted on top of the base platen. 4). Then the top cap was placed on soil sample. 5). All horizontal bender elements were then pushed into the sample, and fixed in place by cable ties to avoid being pushed out by lateral earth pressure when the vertical load increased. The cell was

connected to the pulley system to avoid bending moments on the horizontal bender elements. 6). Then, the outer chamber was filled with salt solution of predetermined concentration. A seating load of about 8 kPa was applied. Consolidation stress was added in increments of 16, 48, 96, 192, 416, 800, and then reduced in decrements of 416, 192, 96, 48, 16, and 8 kPa. The deformation of the consolidometer was monitored, and Taylor's method was used to judge the end of the primary consolidation for each loading step. The weight of NaCl in the bulk solution was considered when calculating void ratios. Compression index, C_c, was calculated by void ratios at stresses of 192, 416, and 800 kPa during loading, while recompression index, C_r, was calculated by void ratios at stresses from 800 kPa to 8 kPa during unloading. The shear wave velocity in vh, hv, and hh directions were measured at the end of each loading step. pH, conductivity, and temperature of the electrolyte in the water bath were monitored with an Accumet Excel XL60 meter (Fisher Scientific). In this study, all tests were conducted in neutral pH environment. The monitored pH values fluctuated around 7.1 ± 0.8. The conductivity was stable with a slight increase due to evaporation. The temperature of the water chamber was 24 ± 2^0C.

4.3.3. Calibration of the Wall-Soil Interface Friction. To evaluate the friction between wall-soil interface, a wall-pulling test was performed. Kaolinite samples were prepared with the same procedure as used in BE tests. The initial height of kaolinite sample is 5 cm (2 inch), which is about half of those used in BE tests. The same floating wall as adopted in the BE tests were used to evaluate the same wall interface. The test setup was shown in Figure 4-6a. Kaolinite sample was placed in the top portion of the floating wall to avoid the predrilled holes for BE installation. Kaolinite sample was

consolidated in K_0 condition at vertical stresses of 16, 48, 96, 192, 416, 800, 416, 192, 48, 16, and 8 kPa, and its settlement was monitored with a dial gauge. After equilibrium of each loading step (judged by Taylor's method), the floating wall was pulled through the pulley by adding weights on the counter weight side. The weights that were used to initiate movement (> 1.0 mm) were recorded. At each loading step, the pulling test was repeated three times, and the average value was reported. Duplicate kaolinite samples were used in the friction test. The pulley friction was calibrated and corrected.

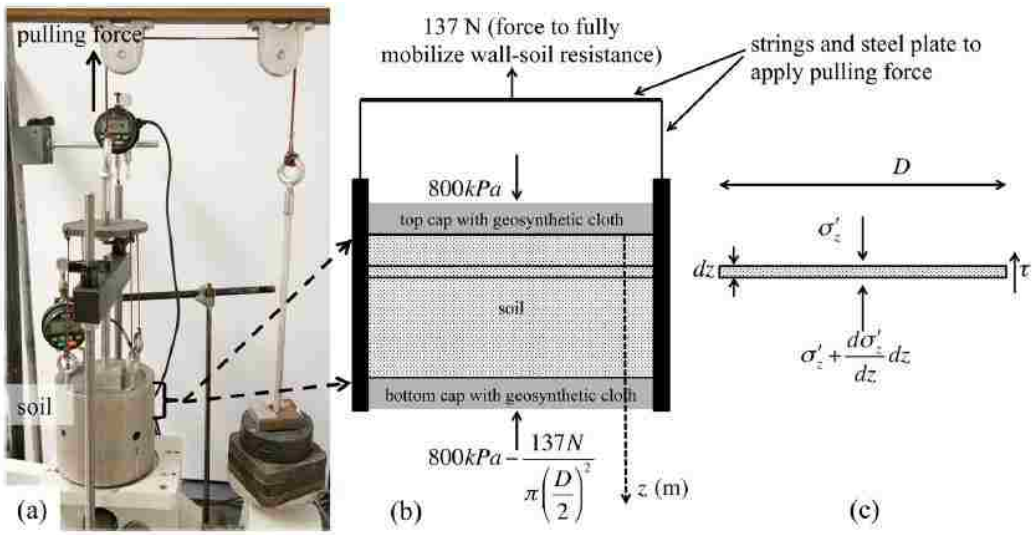

Figure 4-6 (a) Wall-soil interface resistance test setup; (b) boundary conditions for applied 800 kPa vertical loading; (c) representative soil element at depth of z.

4.4. RESULTS

4.4.1. One-Dimensional Consolidation. The 0.005 m/l kaolinite sample showed higher compressibility and swelling potential during unloading (C_c and C_r values of 0.49 and 0.09, respectively) than 1 mol/l kaolinite sample (C_c and C_r values of 0.38 and 0.07,

respectively) (Figure 4-7). This was due to the larger repulsive forces and thickness of electrical double layer (EDL) of low concentration kaolinite particles (Santamarina et al. 2001), which allows more interparticle space for particle realignment, and facilitates higher volume change.

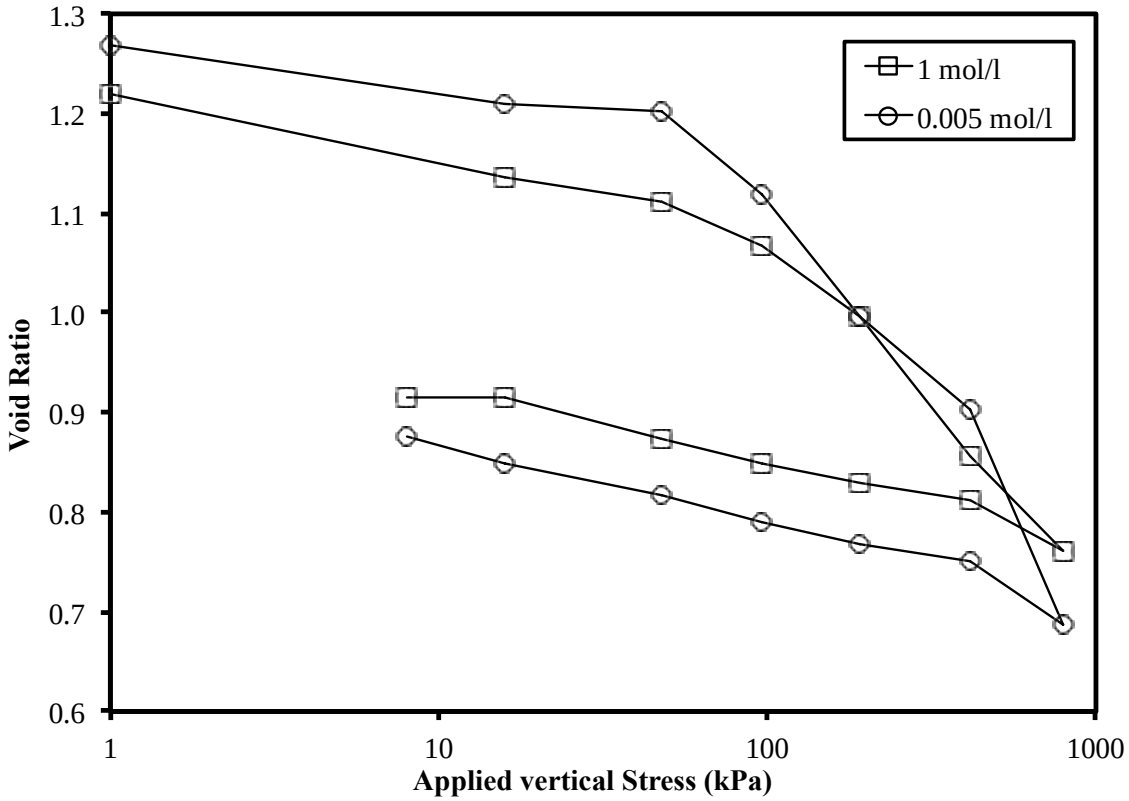

Figure 4-7 e-log $\sigma_v^{'}$ curves of kaolinite samples at different NaCl concentrations.

4.4.2. Typical Received Shear Wave Signals. Typical received shear wave signals exhibited significant differences in arrival times as the applied vertical stress increased, as shown by the S-wave signals at the hh direction for the kaolinite sample with a 0.005 mol/l NaCl solution (Figure 4-8). It was observed that the first arrival time

decreased as the applied vertical consolidation stress increased during the loading stage. At the unloading stage, the first arrival time increased, but was less than that with the same applied stress during the loading stage.

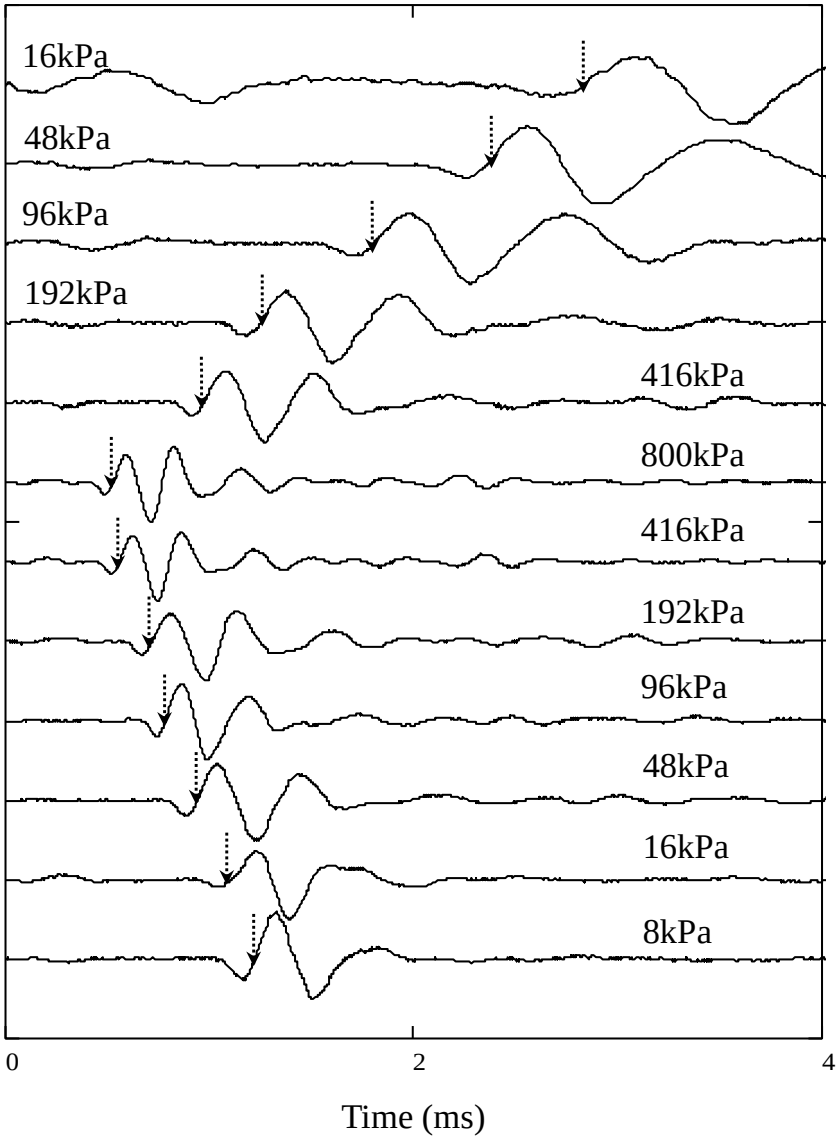

Figure 4-8 Typical received shear wave signals under different applied stresses (kaolinite sample with 0.005 mol/l NaCl solution, S-wave in hh Direction, arrows pointing at first arrival time).

4.4.3. Typical Shear Wave Velocity (V_s) versus Applied Stress Relationship.

Shear wave velocity versus applied stress relationship of a kaolinite sample consolidated from 0.005 mol/l NaCl solution in *vh*, *hv*, and *hh* directions were plotted and are shown in Figure 4-9. Several features were identified that were also true for kaolinite samples at other salt concentrations. 1) During loading, V_s increased as vertical applied stress increased. 2) At a loading less than 100 kPa, V_s in three orthogonal directions almost merged together. At a loading larger than 200 kPa, anisotropy of V_s started to appear (more discussion in Stress-induced fabric anisotropy section). The magnitude of V_s was on the order of hh > hv > vh. 3) At the same vertical stress, V_s during unloading was larger than V_s during loading. 4) The rates of reduction of V_s with respect to vertical stress in three orthogonal directions during unloading were similar.

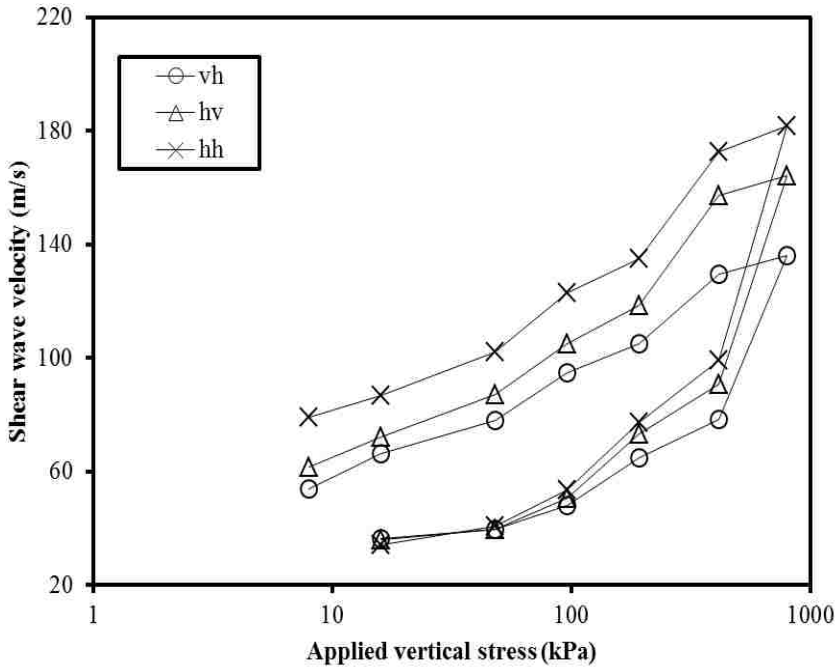

Figure 4-9 Typical shear wave velocity versus applied vertical stress plot of kaolinite samples. (data was from a kaolinite sample with 0.005 mol/l NaCl).

4.5. DISCUSSIONS

4.5.1. Wall-Soil Interface Resistance. Wall-soil interface resistance test results suggested that the wall-soil interface resistance consisted of cohesive and frictional components (Figure 4-10). For an 11.7 cm x 5.08 cm (diameter x height, D x H) sample, the cohesion (c), defined as the y-intercept in Figure 4-10 (19.257 N) in the linear fit on OCR = 1 data normalized by the contacting area (πDH), is 1.08 kPa. The frictional component was characterized by the effective wall-soil interface friction angle φ'. An analytical equation was derived to evaluate φ' as follows. To avoid the complexity introduced by overconsolidation, only 96, 192, 416, and 800 kPa loading steps were considered. Kaolinite sample under 800 kPa vertical stress was analyzed first. At end of each loading there was no excess pore water pressure, so effective stress equaled total stress.

Assuming K_0 was constant along z direction at 800 kPa and the self-weight of soil sample is negligible (considering self-weight will yield less than 1% change in φ' result), a representative soil element was taken for force-equilibrium analysis (Figure 4-6b):

$$\left[\left(\sigma'_z + \frac{d\sigma'_z}{dz}dz\right) - \sigma'_z\right] \cdot \pi\left(\frac{D}{2}\right)^2 + \tau \cdot \pi D \cdot dz = 0 \qquad \text{Equation 4-1}$$

where τ is the total interface resistance (in terms of stress):

$$\tau = c + K_0 \cdot \sigma'_z \cdot \tan\varphi' \qquad \text{Equation 4-2}$$

and D is the diameter of the sample. Equation 4-1 can be simplify to

$$\frac{1}{\left(K_0 \cdot \tan\varphi' \cdot \sigma_z' + c\right)} d\sigma_z' = -\frac{4}{D} dz \qquad \text{Equation 4-3}$$

Given boundary conditions: at z = 0 (top of sample), $\sigma_z' = 800$ kPa, at z = 0.0508 m (bottom of sample); The pulling force to initiate sliding between the wall and soil was 137 N (Figure 4-10). then $\sigma_z' = 800kPa - \frac{137N}{\pi \frac{D^2}{4}} = 786$ kPa. Integrating Equation 4-3 with those boundary conditions gave an implicit equation on $K_0 \cdot \tan\varphi'$, solving which yielded $K_0 \cdot \tan\varphi' = 0.0222$. K_0 of normally consolidated soils can be estimated by Jaky (1944):

$$K_0 = 1 - \sin\phi' \qquad \text{Equation 4-4}$$

where ϕ' is the critical-state effective friction angle, it was measured to be 19.8 degrees (zero cohesion) in this study. This yielded K_0 = 0.6613, then $\tan\varphi' = 0.0336$. Assuming K_0 and φ' are constant during loading, repeating above procedure for vertical stresses of 96, 192, 416 kPa yielded $\tan\varphi'$ values of 0.0489, 0.0398, 0.0299, respectively. An average value of 0.0381 will be used in the subsequent calculations for both normal consolidation and overconsolidation loads, and for different NaCl concentrations.

4.5.2. Wall-Soil Interface Resistance Corrected Vertical Stress σ_z'. For sample of kaolinite 800 kPa loading in a floating wall BE test, the relative displacement between soil and wall is symmetric to the center BE units (z = 0.04 m) (Figure 4-11a). Therefore, friction is upward (+) on the top half of the sample, and downward (-) on the bottom half. Integrating Equation 4-3 for the top half of the sample yielded σ_z' along sample height (total 0.080 m):

$$\sigma'_z = \frac{-c}{K_0 \cdot \tan\varphi'} + \left(800 + \frac{c}{K_0 \cdot \tan\varphi'}\right) \cdot e^{\left(-\frac{4K_0 \cdot \tan\varphi'}{D} z\right)} \qquad \text{Equation 4-5}$$

Similarly, σ'_z of the bottom half of the sample can be calculated. The distribution of σ'_z along the entire soil height was shown in Figure 4-11b. A linear fit to σ'_z on the top half yielded R^2 value of 0.99994. Therefore, for similar sample size and wall-soil interface resistance, σ'_z can be roughly estimated to be linear distribution along sample depth. Assuming mobilized at a strain larger than 1 mm, the wall-soil interface resistance distribution, calculated by Equation 4-2, was shown in Figure 4-11c.

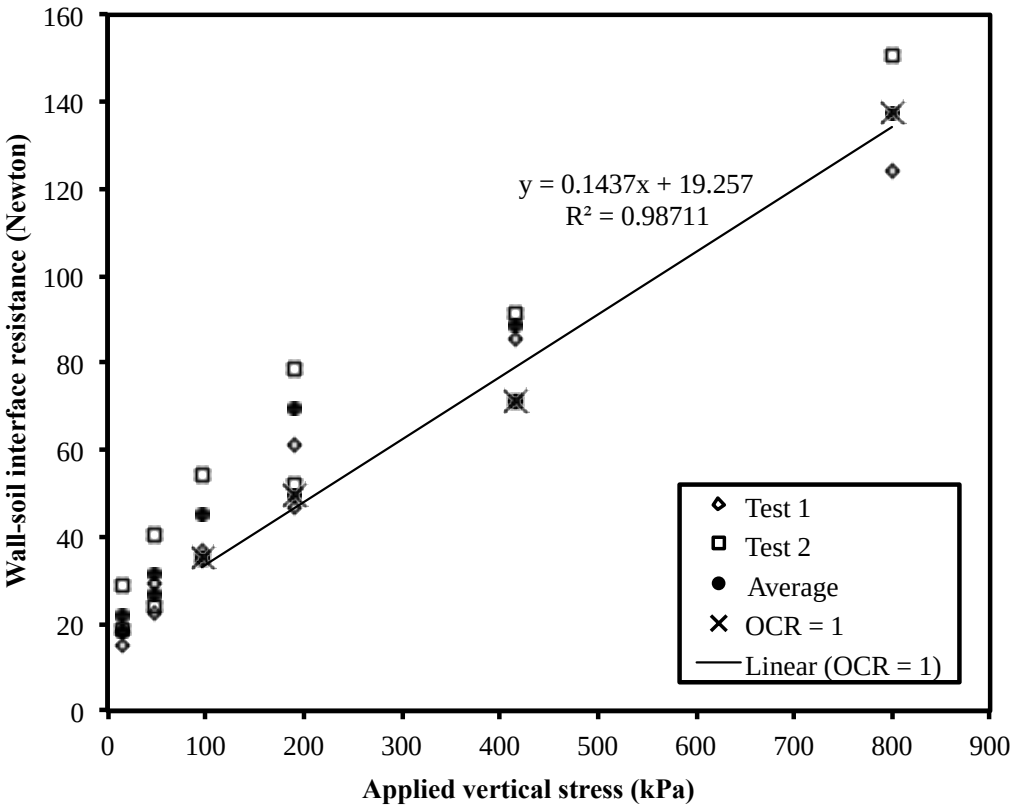

Figure 4-10 Measured wall-soil interface resistance (in terms of cumulative force, unit: N) vs. applied vertical stress for tap water kaolinite sample.

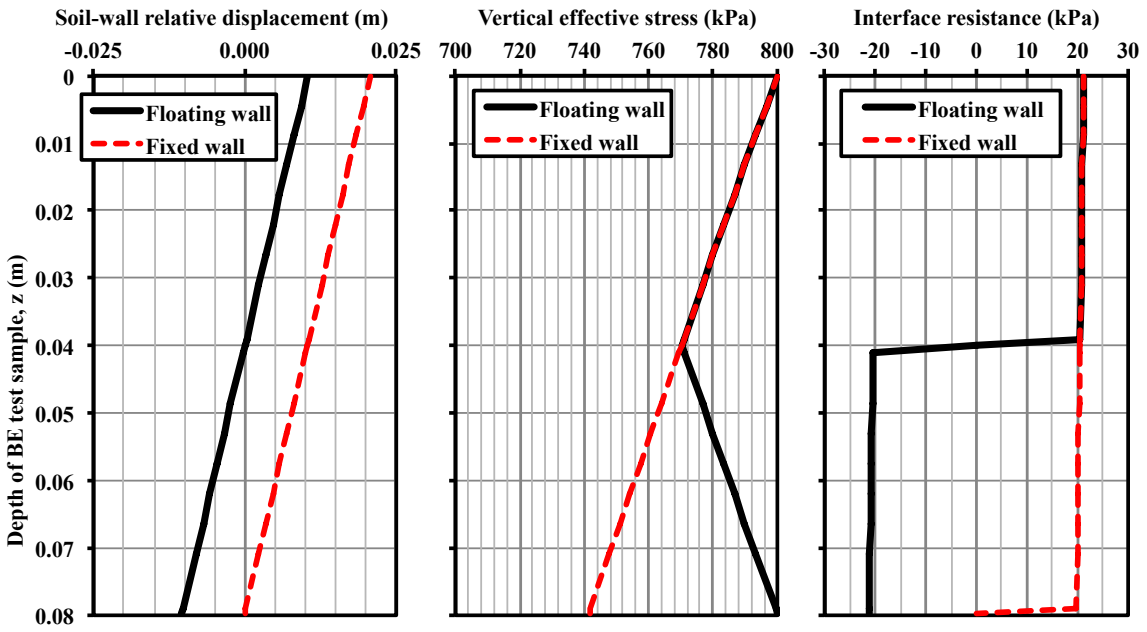

Figure 4-11 Comparison of floating wall and fixed wall (hypothesized) consolidometer BE test setup for kaolinite sample in 1 mol/l NaCl under 800 kPa vertical stress. a) Soil-wall relative displacement, soil move downward relative to the wall is positive; b). vertical effective stress considering wall friction; c). friction along the sample height, upward friction is positive.

Similar calculation can be performed on a hypothesized fixed wall consolidation sample with the same geometry as above floating wall bender element test. The sample in the fixed wall is always moving downward in reference to the wall during loading, which generates upward friction (+) (Figure 4-11a). The resulting σ_z' distribution was shown in Figure 4-11b. It was clearly shown that the floating wall setup is advantageous to the fixed wall setup in reducing friction: the average σ_z' value in a floating wall consolidometer is near 785 kPa, while that in a fixed wall consolidometer is around 770 kPa. In another word, floating wall setup allows thicker soil samples, which provide more flexibility to satisfy R_d ratio (wave propagating distance to wave length ratio)

requirement. Except for the mid-height of the floating wall sample and the bottom of the fixed wall sample, the majority of the soil will move relative to the wall, and therefore generate resistance. Using Equation 4-2, the wall-soil interface resistance profile of a fixed wall setup was shown in Figure 4-11c.

Using the above method, average friction corrected vertical effective stress for 1 mol/l kaolinite sample was calculated for each loading and unloading steps. For overconsolidation ratio (OCR) larger than 1, equation by Mayne and Kulhaway (1982).

$$K_0 = (1 - \sin\phi') \cdot (OCR)^{\sin\phi'} \qquad \text{Equation 4-6}$$

was used. Results were listed in Table 4-2. It was observed that vertical stress loss due to interface resistance is no more than 3% for normally consolidated cases. For high OCR cases, vertical stress decrement can be as high as 18.6% (at applied vertical stress of 8 kPa), because OCR leads to significant increase in K_0 (Table 4-2). Similar trends were observed for 0.005 mol/l kaolinite sample.

4.5.3. Comparison with Studies in the Literature. Measured stiffness of RP - 2 kaolinite, in terms of both V_s and G_{max}, was compared with published results (Figure 4-12) (Chang et al. 2006; Fam and Santamarina 1995; Fam and Santamarina 1997; Jovicic and Coop 1998; Meng 2003; Shibuya et al. 1995; Viggiani and Atkinson 1995; Wang and Siu 2006).

It was observed that the average the shear wave velocity of Georgia RP-2 kaolinite was lower than those published results. One of the major differences between these kaolinites was the grain size distribution (Figure 4-5). The grain size of RP-2 kaolinite is much smaller than those used in other studies (Figure 4-5). The 50% passing sieve size, d_{50}, of RP-2 kaolinite is 0.36 μm, which is only 26% to 58% of the d_{50} values

in other studies as listed in Table 4-1. Smaller particle size makes shear wave transmitting through longer and more tortuous force chains (chains of particle contacts), which yields lower stiffness. It is worth noting that small kaolinite particles seem to coincide with lower large-strain strength (Table 4-1). The critical state effective friction angle of Georgia RP-2 kaolinite (d_{50} = 0.36 μm), Peerless clay (kaolinite) (d_{50} = 0.62 μm), Speswhite kaolinite (d_{50} = 0.72 μm), and Georgia kaolinite used by Anandarajah and Zhao (2000) (d_{50} = 1.6 μm) are 19.8, 25 (± 5), 27.5, and 30 degrees, respectively.

Other factors, such as cation exchange capacity of clays, adsorbed ion type and quantity also influence the stiffness of fine-grained soils because these factors will influence interparticle contact properties through modifying the diffuse double layer (Bate et al. 2013).

Table 4-2 Friction corrected vertical effective stress calculation spreadsheet for 0.005 and 1 mol/l kaolinite samples

Applied σ_z' (kPa)	OCR	k_0	1 mol/l sample				0.005 mol/l sample			
			Friction Corrected σ_z' (kPa)	Height (mm)	$\Delta\sigma_z'$ (kPa)	$\Delta\sigma_z'/\sigma_z'$ (%)	Friction Corrected σ_z' (kPa)	Height (mm)	$\Delta\sigma_z'$ (kPa)	$\Delta\sigma_z'/\sigma_z'$ (%)
16	6	1.230	14.5	97	1.5	9.4%	14.7	79	1.3	8.0%
48	2	0.848	45.8	96	2.2	4.5%	46.2	79	1.8	3.8%
96	1	0.661	93.1	94	2.9	3.0%	93.6	76	2.4	2.5%
192	1	0.661	187.3	90	4.7	2.4%	188.1	71	3.9	2.0%
416	1	0.661	407.4	84	8.6	2.1%	408.7	68	7.3	1.8%
800	1	0.661	784.8	80	15.2	1.9%	787.8	60	12.2	1.5%
416	2	0.825	405.7	82	10.3	2.5%	407.6	63	8.4	2.0%
192	4	1.072	185.5	83	6.5	3.4%	186.7	63	5.3	2.8%
96	8	1.356	91.6	84	4.4	4.6%	92.4	64	3.6	3.7%
48	17	1.715	44.9	85	3.1	6.5%	45.5	65	2.5	5.3%
16	50	2.488	14.1	87	1.9	12.0%	14.4	66	1.6	9.7%
8	100	3.147	6.5	87	1.5	18.6%	6.8	67	1.2	15.2%

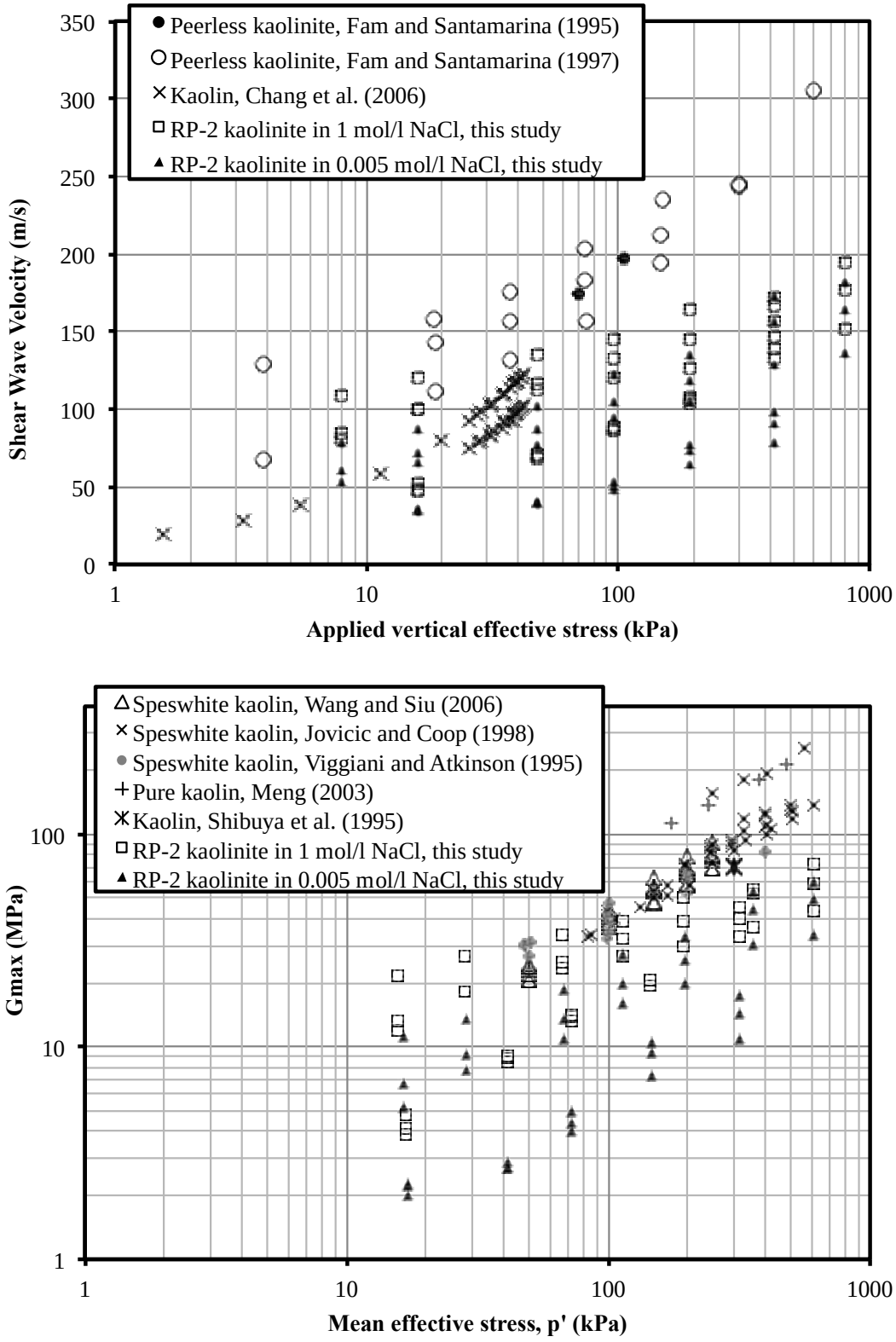

Figure 4-12 Comparison with stiffness of different kaolinites studied in the literature. (a) V_s versus applied vertical stress results; (b) G_{max} versus mean effective stress (friction corrected mean effective stress values in this study were used).

4.5.4. Stress Dependency of V_s. As stated in Introduction section, the shear wave velocity increases with the mean normal effective stress on the polarization plane. The stress dependence of V_s can be expressed by (Santamarina et al. 2001)

$$V_s = \alpha \left(\frac{\sigma_m^{'}}{1kPa} \right)^{\beta} \qquad \text{Equation 4-7}$$

where $\sigma_m^{'}$ is the mean normal effective stress on the polarization plane, α factor (m/s) is the velocity of a medium subject to 1 kPa confinement, exponent β represents the amount of stress-dependent effect. β value has been theoretically related to contact effects, with 1/6 for Hertzian contact (elastic spheres), 1/4 for cone-to-plane contacts (rough or angular particles) or for spherical particles with contact yield, and 3/4 for contacts governed by Coulombian forces (Johnson 1985; Santamarina et al. 2001). It can be seen that

$$\sigma_m^{'} = \frac{(1+K_0)}{2} \sigma_v^{'} \qquad \text{Equation 4-8}$$

for vh and hv directions, while in hh direction $\sigma_m^{'} = K_0 \sigma_v^{'}$, where $\sigma_v^{'}$ is the vertical effective stress, and K_0 can be obtained by Equation 4-4 or 4-6. The measured critical state effective friction angle by consolidated undrained triaxial compression test for Georgia RP-2 kaolinite is 19.8 degrees. Wang and Siu (2006) stated that critical state effective friction angle did not change with pore fluid concentration. Therefore, ϕ_{cs}' of 19.8 degree was assumed to be applicable for kaolinite samples in 0.005 and 1 mol/l NaCl solutions, and for both loading and unloading conditions. The calculated K_0 values at different loading stages were listed in Table 4-2. For kaolinite samples at each NaCl

concentration, the loading (OCR = 1) and unloading data were fitted separately with least square method. The relationship between fitted α and β are plotted in Figure 4-13.

It can be observed in Figure 4-10 that α values were larger during unloading than during the loading phase. During unloading, the maximum vertical stress in history of 800 kPa increased the soil density, yielding a more compact fabric, which gave higher V_s values. As concentration increased, α increased in general. This was due to the enhanced contacts by the shrinkage of EDL. The average β exponent during the unloading phase was 0.1752, which was close to the Hertzian contact value, 1/6 (0.1667). Thus, it could be postulated that the contact effects during unloading were more elastic (Hertzian contact). β was higher in the loading than in the unloading phase. This indicated a contact effect change from elastic (unloading) to where yielding and rough and angular particle interactions occurred (loading). Especially, at a low concentration (0.005 mol/l) β was approaching 0.65, which might indicate that Coulombian forces started to play an important role in contact behavior. It was also observed that, generally, as the concentration increased, β decreased. It was proposed that shrinkage of the thickness of a double layer reduced electrical interaction, and enhanced particle to particle contact forces.

Santamarina et al. (2001) proposed the relationship $\beta = 0.36 - \alpha/700$ for a series of laboratory data. Ku et al. (2011) summarized α and β values for an extensive amount of field data. Both results were plotted and are shown in Figure 4-13 as references. Although kaolinite results in this study bore a similar trend to those of Ku et al. (2011), and of Santamarina et al. (2001) during the unloading phase, they were lower. The lower

β values were postulated to be caused by the addition of NaCl, which compressed the EDL, decreased particle to particle distance, and enhanced direct contact behavior.

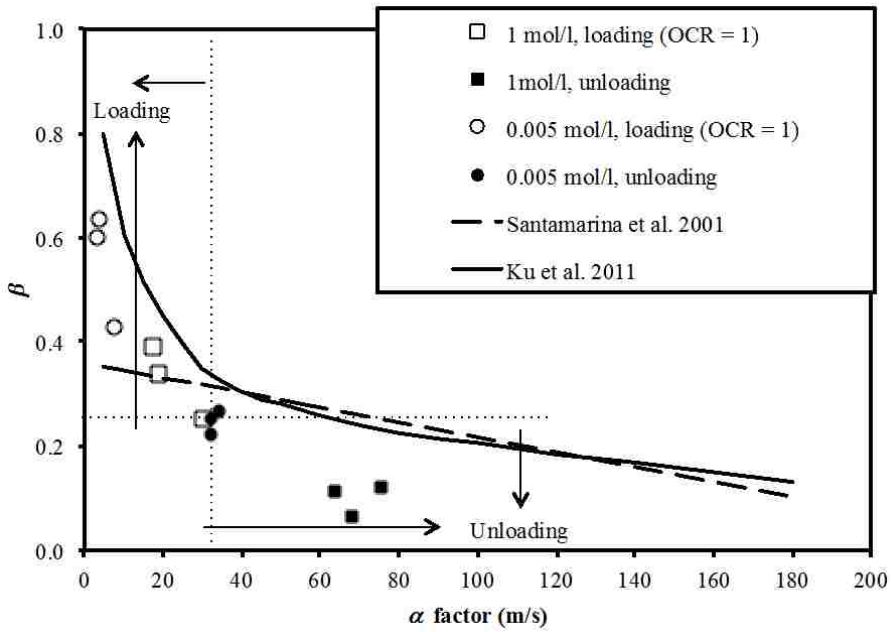

Figure 4-13 Typical values for α and β coefficients in this study.

4.5.5. Stress-Induced Fabric Anisotropy. Kaolinite particle was platy-shaped with a thickness of 1 nm and a length of 50 – 2000 nm (Mitchell and Soga 2005). If the wall resistance corrected mean effective stress in the polarization plane was higher than 50 – 100 kPa (Figure 4-14a), kaolinite plates were suppressed to align more horizontally. This induced preferential orientation in a horizontal direction for kaolinite plates, and led to fabric anisotropy. Stress-induced fabric anisotropy was manifested by the different magnitudes of V_s values in three orthogonal directions (hh, hv, and vh) (Figure 4-14a). Shear wave velocity at both 0.005 and 1 mol/l NaCl concentrations followed the same

order: hh > hv > vh. During unloading, V_s anisotropy decreased, but the hierarchy remains (Figure 4-14b).

Cross-anisotropy (or transversely isotropic fabric) materials, where the physical properties in the vh and hv directions were the same, was often assumed in soils in the literature (Bellotti et al. 1996; Chen et al. 2005; Graham et al. 1983; Wang and Mok 2008; Wood 1990; Yimsiri and Soga 2000). This suggested that V_s in the vh and hv directions were the same. While this arguably holds true for coarse-grained particles, such as sand, gravel, and rice, results in this study indicated that it was not the case for fine-grained soils. This hierarchy of V_s anisotropy in hv and vh directions of other fine-grained soils was also reported in the literature. Pennington et al. (1997) also reported that V_s in the hv direction was significantly higher than that in the vh direction for natural Gault clay. In addition, Lee et al. (2008) found $V_{s,hv} > V_{s,vh}$ for Incheon marine clay at stresses higher than 100 kPa.

4.5.6. Void Ratio Dependency of V_s. Figure 4-15 showed the shear wave velocity versus void ratio relationship in hh direction. Similar trends were observed for V_s in vh and hv directions. It was observed that given the same salt concentration, V_s decreased as void ratio increased. However, the same void ratio could yield different V_s values due to the applied stresses and salt concentration (Figure 4-15).

4.5.7. Advantages of the Developed BE Testing System. Comparing to a fixed wall type consolidometer setup, the floating wall type consolidometer bender element testing system has many advantages. One major advantage is that the damages to the bender element due to a soil deformation-induced bending moment were eliminated.

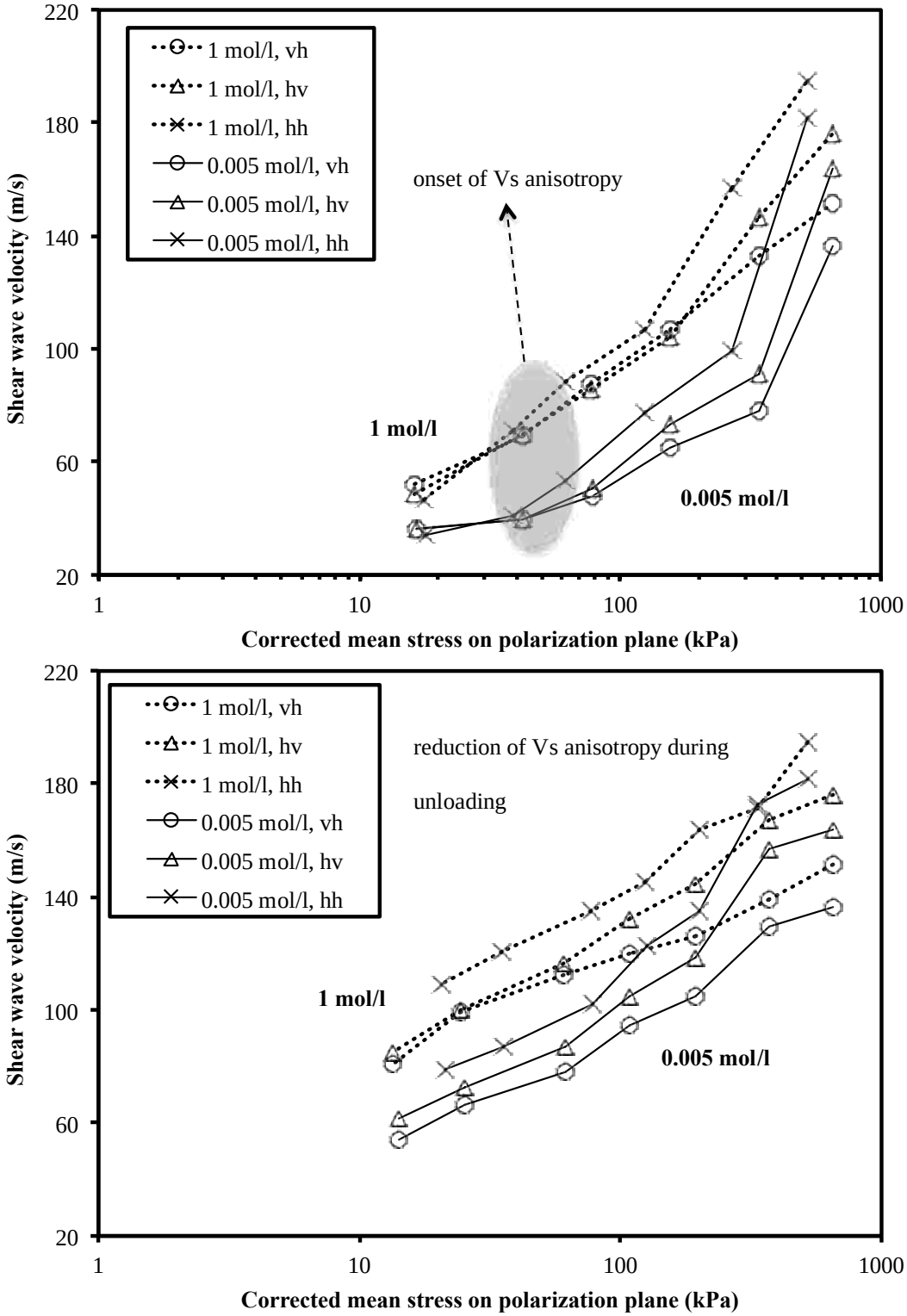

Figure 4-14 Shear wave velocity versus interface resistance corrected mean effective stress on the polarization plane for kaolinite samples with 0.005 and 1.0 mol/l NaCl solutions. (a) loading; (b) unloading.

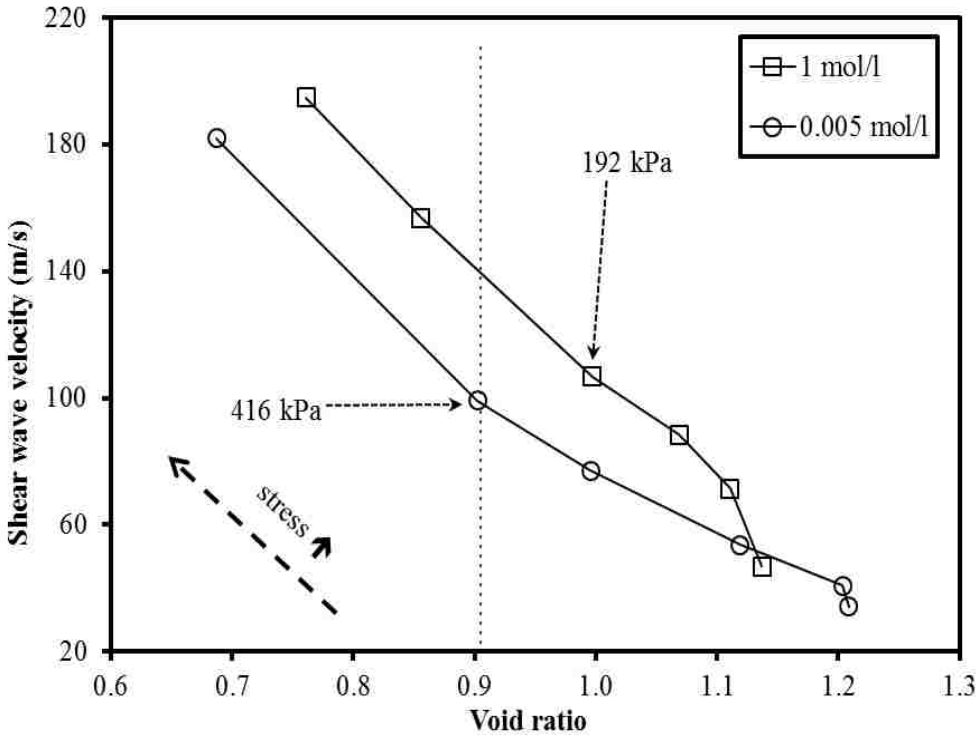

Figure 4-15 Shear wave velocity versus void ratio in the hh direction during loading.

The maximum normal consolidation stress applied to kaolinite samples was 800 kPa. Under such high stress, the maximum settlement ranged from 1.8 – 2.3 cm (0.7 – 0.9 in). However, the bender element was not damaged after five tests (subset b in Figure 4-1). In addition, there also many other advantages which include (i) The maximum load capacity of the consolidometer (Humboldt HM-1100A) (1425 kPa in this study, with a sample diameter of 11.4 cm (4.5 inch) and beam ratio of 10:1) can be applied to the sample, which facilitated the investigation of fabric anisotropy at high consolidation stresses. (ii) Full saturation of the soil sample was achieved by slurry consolidation and maintained by the water chamber. (iii) The water chamber maintained constant

physicochemical testing of the environment, including pH, salt concentration, and the temperature.

Comparing to bender element mounted in a triaxial sample, the benefits of the proposed floating wall BE testing system are as follows. (i) Installation of horizontal BE, through predrilled hole in the floating wall, is easy to realize. Concurrent measurement of V_s in three orthogonal directions in one sample is easy to realize as well. (ii) The height of a soil sample (less than 11 cm), i.e. the distance of vertically propagating S-wave (vh), is less than sample diameter (11.7 cm). This geometry elongated the bounced P-wave transmitting path, and reduced its interference. (iii) Due to the high stiffness (stainless steel) and thick floating wall (1.3 cm), horizontal bender will be tightly fixed in place, which significantly reduces P-wave transmitting directly to the receiving end. (iv) Because there is no limitation on the diameter or height of the sample in a floating wall setup, there is more flexibility of modifying the geometry to achieve optimal R_d ratio and signal quality, and to reduce near field effect (Lee and Santamarina 2005; Li et al. 2012).

4.6. CONCLUSIONS

A new floating wall consolidometer-type bender element testing system was developed to study stiffness anisotropy of clays at applied vertical stress up to 800 kPa. Higher vertical stress of up to 1425 kPa can be applied to a 114 cm (4.4 inch) sample. Georgia RP-2 Kaolinite samples with NaCl concentrations of 0.005 and 1.0 mol/l were measured in this testing system.

Floating wall–soil interface resistance was quantified with pulling tests. Analytical equations were then derived to calculate the wall resistance-corrected vertical effective stress.

The critical state effective friction angle for RP-2 kaolinite was measured as 19.8 degree. Using Equation 4-5 or 4-7, more accurate normal stresses can be obtained. As a result, stress-induced fabric anisotropy can be analyzed more precisely.

The shear wave velocity (V_s) (a term used to quantify the small strain stiffness of soils) of kaolinite was measured via the bender element test. Average V_s results for RP-2 kaolinite were less than those of other kaolinites reported in the literature. This was postulated to be primarily due to the longer and more tortuous chains of particle contacts associated with the smaller median diameter (d_{50}=0.36 lm) of RP-2 kaolinite samples. Bender element test results indicated that V_s increased with stress, density, and concentration.

The hierarchy of V_s in three orthogonal directions (i.e., hh > hv > vh) agreed with results in the literature. It was also illustrated that V_s anisotropy increased with applied stress and decreased during unloading.

A floating wall design eliminated the detrimental bending moment that acted upon the benders due to soil settlement, which greatly improved signal quality and bender reuse.

Floating wall-soil interface resistance was evaluated with both pulling tests and analytical equations, and was quantified with cohesion and friction components. In addition, the water chamber maintains saturation and pH, salt concentration of bulk fluid.

Several advantages of the newly developed device in measuring stiffness anisotropy over a triaxial test setup were discussed.

The benefit including easiness of installing horizontal bender elements, concurrent measurement of V_s in three orthogonal directions in one sample (compared to

single pair bender element setup), the flexible geometry in design that can improve the signal quality by limiting side-reflected P-waves and the near field effects (compared to three pairs bender element setup), and the reduction of directly transmitting P-waves (compared to frictional bender element setup).

5. SHEAR WAVE VELOCITY AND ITS ANISOTROPY OF ORGANICALLY MODIFIED FLY ASH-KAOLINITE MIXTURES

5.1. INTRODUCTION

Recent developments of using organic agents for soil stabilization have shed lights on the sustainably reuse of fly ash. The previous studies, however, were found majorly focused on the mechanical properties, such as strength, permeability, hydraulic conductivity, and compressibility. The effects of polymers and fly ash on the V_s and V_s anisotropy still remain not well documented in the literature, especially the V_s anisotropy of the organically modified fly-ash soil mixtures. Stiffness anisotropy is often presented in natural and engineered geomaterials. Stiffness anisotropy can be evaluated by shear wave velocities in three orthogonal directions (Figure 5-1), The ratio of the maximum (normally in *hh* direction) and minimum (normally in *vh* direction) G_{max} can be higher than 1.65 (or 1.29 in terms of V_{s-hh}/V_{s-vh} ratio) for Gault Clay (Pennington et al. 1997). Therefore, negligence of stiffness anisotropy can render errors in the design and simulations. In addition, cross-anisotropy, i.e., the geotechnical properties in *vh* and *hv* directions are the same, is often assumed in micromechanical models and theories (Yimsiri and Soga 2000). Many published works, however, presented that soils are not cross-anisotropy materials (Kang et al. 2014; Pennington et al. 1997; Wang and Mok 2008). The validity of this assumption for polymer modified fly ash-kaolinite mixtures has not been verified.

In this study, the small-strain stiffness of fly ash-kaolinite mixtures at fly ash contents of 0, 10, 20, 30, 60, and 100% was measured by bender element tests. Synthetic polymers (PEO) and biopolymers (xanthan gum and chitosan) were used to examine their

effects on the small-strain stiffness of the 30% fly ash-kaolinite mixtures. The influencing factors on V_s and V_s anisotropy of fly ash-kaolinite mixtures, including the stress conditions, physicochemical conditions of polymer solutions, and the associated underlying mechanisms were quantified.

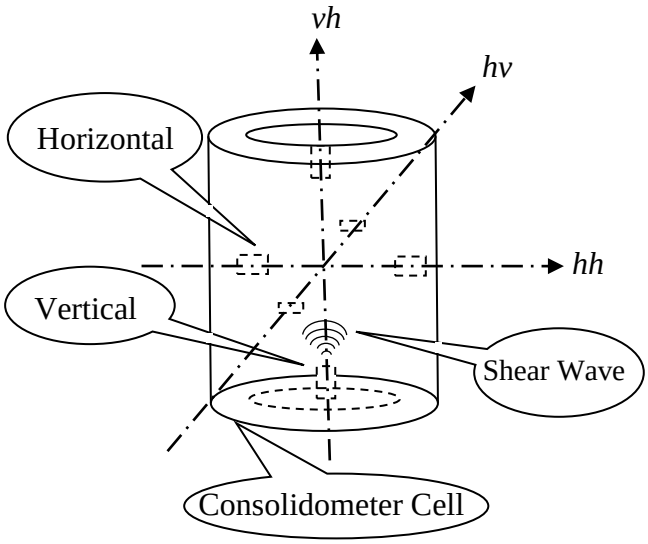

Figure 5-1 A sketch of the floating wall type consolidometer cell and the bender elements setup.

5.2. MATERIALS

Georgia kaolinite (RP-2, Active Minerals International) was used in this study. Georgia kaolinite has a specific gravity of 2.60 and d_{50} value of 0.4 micron (as shown in Figure 5-2). The fly ash used in this study was from Lafarge power plants (Wisconsin, USA). This fly ash is classified as Class F (ASTM standard C 618), which has very

limited self-cementing capability. The d_{50} of the fly ash is 50 times larger than that of the Georgia kaolinite (Figure 5-2).

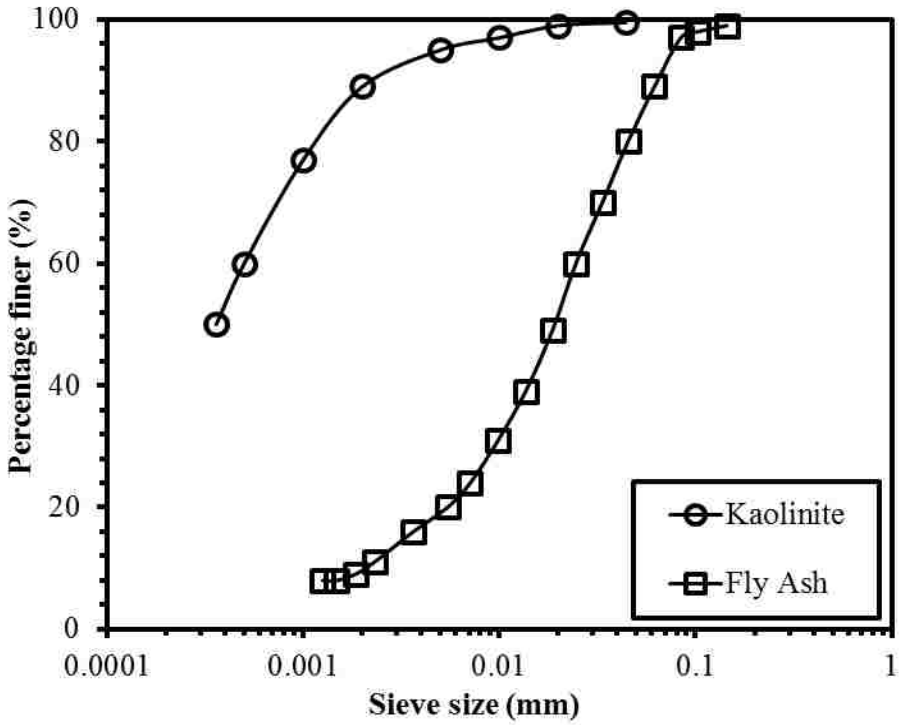

Figure 5-2 Grain size distributions of fly ash and kaolinite.

Three organic polymers were used in this study to modify the engineering properties of fly ash-kaolinite mixtures, namely, neutrally charged polyethylene oxide ($(-CH_2CH_2O-)_n$, PEO, M.W.= 600,000), positively charged Chitosan ($(C_6H_{11}NO_4)_n$), M.W. = 100,000 – 300,000), and negatively charged xanthan gum ($(C_{35}H_{49}O_{29})_n$, M.W.= 90,000-160,000). Their chemical structures are shown in Figure 5-3. All chemicals were purchased from Fisher Scientific and were used as received.

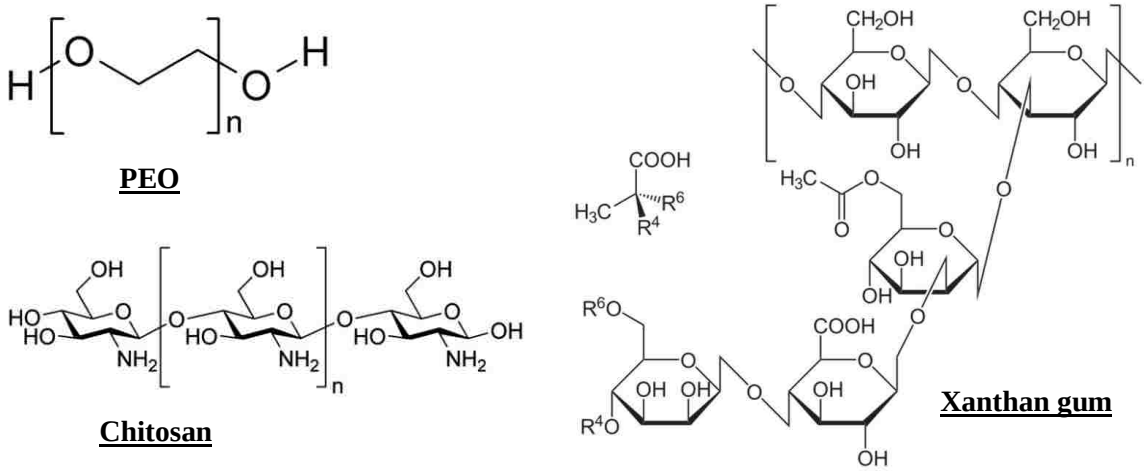

Figure 5-3 The chemical structures of PEO, chitosan, and xanthan gum.

5.3. EXPERIMENTAL METHODS

5.3.1. Scanning Electron Microscopy (SEM) Imaging. SEM tests were carried out on kaolinite, fly ash, and organically treated kaolinite and fly ash-kaolinite samples with SEM S-4700 (Hitachi Inc.). The samples were coated with gold powder using a sputter-coater (Hitachi E-1030) before testing. For each sample, four to six images were taken and compared, and then a representative image was reported.

5.3.2. Effective Specific Gravity. " Effective " specific gravity of the fly ash cenospheres measured from pycnometer test (ASTM D 854 - 14) is often used to calculate the void ratio of a fly ash sample (Bachus and Santamarina 2012). It is understood that the volume calculated by "effective" specific gravity is less than the true volume occupied by the fly ash cenospheres, assuming the hollow cenospheres are filled with pore fluid. In this study, the void ratio of the fly ash-kaolinite mixtures were calculated based on the "effective" specific gravity measured from pycnometer test.

5.3.3. Determination of the Shell Thickness of Fly Ash Cenospheres. In order to estimate the volume possessed by the cenospheres in the fly ash-kaolinite mixture so as to obtain a realistic cenospheres distribution, the shell thickness of cenospheres needs to be acquired. Statistical methods from interferometry or microscopy images were used to capture the characteristic scale of sub-micron geometries in the literature. Kumar et al. (2013) used vertical scanning interferometry 3D image with a scan rate of 70 fps (frames per second) to determine the surface roughness change of mineral surfaces driven by dissolution or precipitation. Kolay and Bhusal (2014) measured the shell thickness of the fly ash cenospheres with SEM pictures on a glued/ground surface. Similar statistic method was used in this study. Fly ash particles were ground with a pestle and a mortar for 120 minutes to break the cenospheres. Then the broken cenospheres were imaged with the SEM. A total of 36 images were taken at different locations from six powder samples. The shell thicknesses of cenospheres were measured directly from SEM images (Hitachi FE-SEM). Assuming a normal distribution, the mean value and standard deviation of the shell thickness were calculated.

5.3.4. Sample Preparation by Slurry Consolidation Method. Dry fly ash and at weight ratios of 0, 10%, 20%, 30%, 60% and 100% were mixed and submerged into 0.01 mol/l NaCl solutions or 1 g/l polymers (PEO, xanthan gum, or chitosan) solutions with a solid to water ratio of approximately 0.2 (± 0.05). The resulting slurry was then gently stirred by hand for 30 minutes and then let stand for 24 hours for the completion of the hydration process. The slurry was then transferred into an aluminum tube (height × diameter of 45.7 × 11.7 cm (18 × 4.5 in)) with double drainage conditions. Vertical loadings of 3.5, 7, 14, 28, 50, and 100 kPa, were applied to the slurry, followed by

unloading of 50, 28, 14, 7 and 3.5 kPa. Each loading step was maintained until the end of primary consolidation was achieved (judged by Taylor's method). After slurry consolidation, the sample was extruded and sealed with food-wrap and zip-lock bag, and was stored in a 100% moist room until use. The sample was trimmed down to a size of 11.4 $\times$ 10.2 cm (diameter by height) to mount into the floating wall-type consolidometer (11.4 cm $\times$ 12.7 cm; diameter by height) for bender element tests. The sample was completely submerged into a fluid chamber filled with water/salt solution (0.01 mol/l), where the pH, temperature, and ionic strength were monitored during the entire testing (up to 7 days long).

5.3.5. V_s Measurement with Bender Element Method. In this study, a floating wall consolidometer type-bender element testing system developed in a prior study (Kang et al. 2014) was used to measure the shear wave velocity in three orthogonal directions as shown in Figure 5-1. The key steps of the bender element test are outlined as follows. After applying a small seating load (~8 kPa) to the sample, vertical consolidation stress increased in the sequence of 16, 48, 96, 192, 416, 800 kPa and reduced in the reverse order. Taylor's method was used to determine the end of primary consolidation, after which shear wave velocities in *vh*, *hv*, and *hh* directions were measured. Tip-to-tip distance was used as the travel distance. The exciting frequency of the sinusoidal signal at the transmitter bender element was adjusted approximately to the resonance frequency (typically ranged from 2-10 kHz, 33210A, Agilent function generator), and the amplitude was set at 10 V. The input wave was amplified (5X to 10X) by a linear amplifier (EPA-104, Piezo System Inc, Cambridge, MA), and the received signal was filtered by a filter/signal conditioner (3364, Krohn-Hite, Brockton, MA) with a fixed band pass filter

at 200-50,000 Hz. Square signal was also used for each measurement to check repeatability.

5.3.6. Soil-Side Wall Interface Friction Correction. To accurately calculate the effective vertical stress, the soil-wall interface friction was corrected by wall pull-out test following the procedures proposed by Kang et al. (2014). The average friction corrected vertical effective stress applied on the sample is (Kang et al. 2014):

$$\sigma_v^{'} = \frac{-c}{K_0 \tan\varphi'} + \frac{\left(\sigma_{applied} + \frac{c}{K_0 \tan\varphi'}\right)D}{2HK_0 \tan\varphi'}\left(1 - e^{\left((2K_0 \tan\varphi')H/D\right)}\right) \qquad \text{Equation 5-1}$$

where the OCR is the over consolidation ratio of a soil, D is the diameter of the sample, and H is the height of the sample. The cohesion (c) and the interface friction coefficient ($\tan\varphi'$) between the soil and the side wall were determined by the wall pull out test. The effective critical state friction angle ϕ' was measured by consolidated undrained triaxial shear test (ASTM D4767) (Kang 2015). K_0 can be determined from Equation 5-2 (Mayne and Kulhawy 1982):

$$K_0 = (1 - \sin\phi^{'})(OCR)^{\sin\phi'} \qquad \text{Equation 5-2}$$

Consequently, the stress dependence of V_s can be expressed by Equation 5-3 (Santamarina et al. 2001):

$$V_s = \alpha\left(\frac{\sigma_{corr}^{'}}{1kPa}\right)^{\beta} \qquad \text{Equation 5-3}$$

where $\sigma_{corr}^{'}$ represents the side wall friction corrected mean normal effective stress on the polarization plane: $\sigma_{corr}^{'} = \frac{(1+K_0)}{2}\sigma_v^{'}$ for *vh* or *hv* directions and $\sigma_{corr}^{'} = K_0\sigma_v^{'}$ for *hh*

direction, α factor (m/s) is the velocity of a medium subject to 1 kPa confinement, exponent β is related with the contact effects.

5.4. RESULTS

5.4.1. Scanning Electron Microscope Images. SEM images suggested that the majority of the fly ash particles used in this study are spheres with hollow inside (Figures 5-4a and 5-4b). The platy-shaped Georgia RP-2 kaolinite aggregates can be seen in Figure 5-4c. SEM images of 30% and 60% fly ash-kaolinite mixture are shown in Figures 5-4d and 5-4e. Approximately continuous contacts between fly ash particles for 60% fly ash-kaolinite mixture were observed in Figure 5-4e. SEM images of kaolinite and 30% fly ash-kaolinite mixture treated with PEO, chitosan and xanthan gum were presented in Figures 5-5a and 5-5f. Figure 5-5a indicated that PEO has induced larger face-to-face (FF) aggregations (aggregate size on the order of 2.6 μm) than the aggregate size of unmodified kaolinite (on the order of 0.6μm, indicated by the SEM image). Besides FF fabric, edge-to-edge (EE) and edge-to-face (EF) particle associations were observed in chitosan and xanthan gum treated kaolinite and 30% fly ash-kaolinite mixtures (Figures 5-5c and 5-5e).

5.4.2. Fly Ash Cenosphere Shell Thickness. The shell thickness values of 67 fly ash cenospheres (such as shown in Figure 5-4b) from 36 SEM images were measured. Assuming a normal distribution, the mean value and the standard deviation were 0.0033 mm and 0.0019 mm, respectively. Although the mean shell thickness and standard deviation could not represent the true characteristics of the fly ash cenospheres, a reasonable and approximation of the fly ash distribution by assuming normal distribution is still considered to be validated.

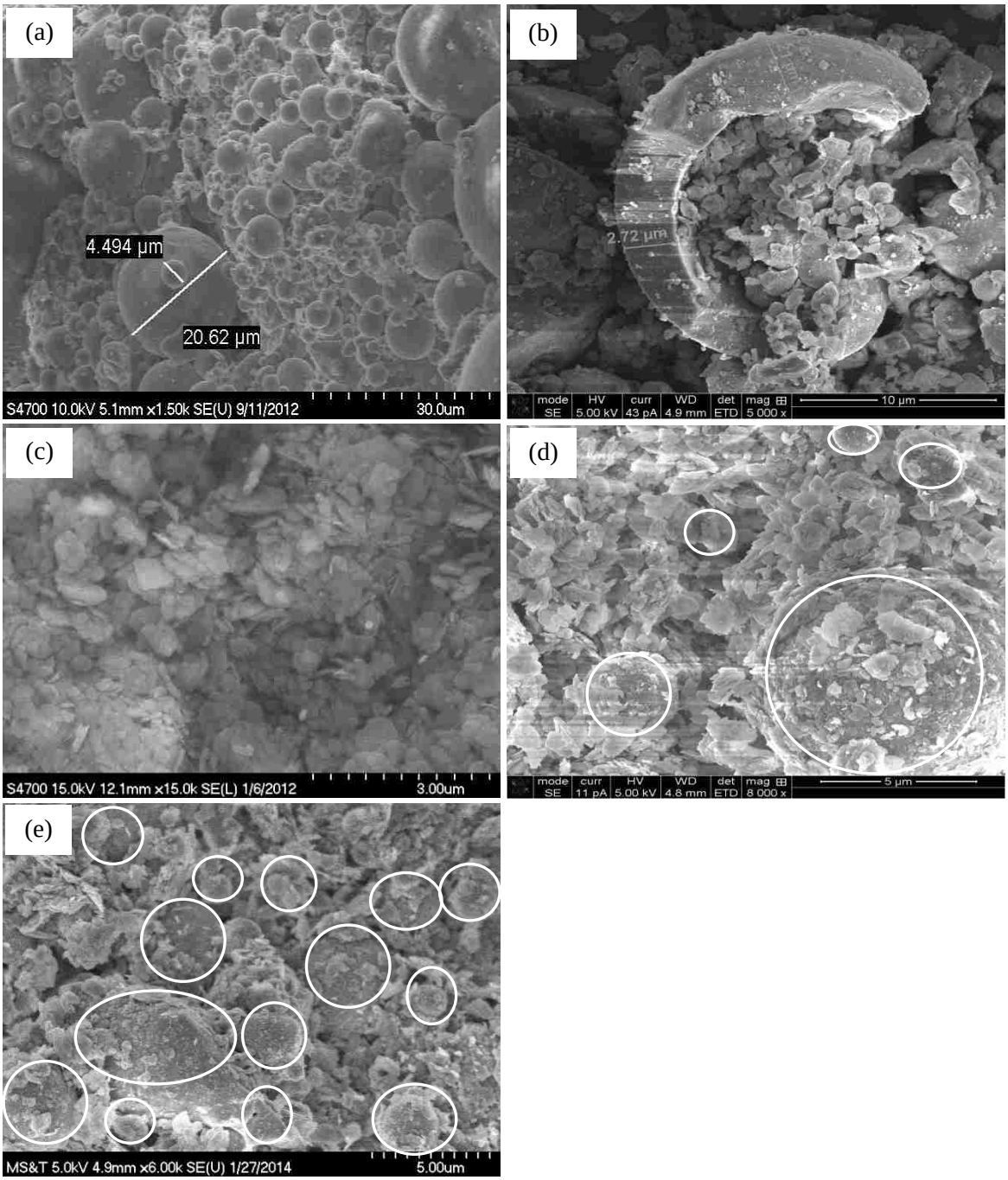

Figure 5-4 SEM images of fly ash (a), pulverized fly ash (b), untreated kaolinite (c), and fly ash-kaolinite mixtures at (d) 30% and (e) 60% fly ash content.

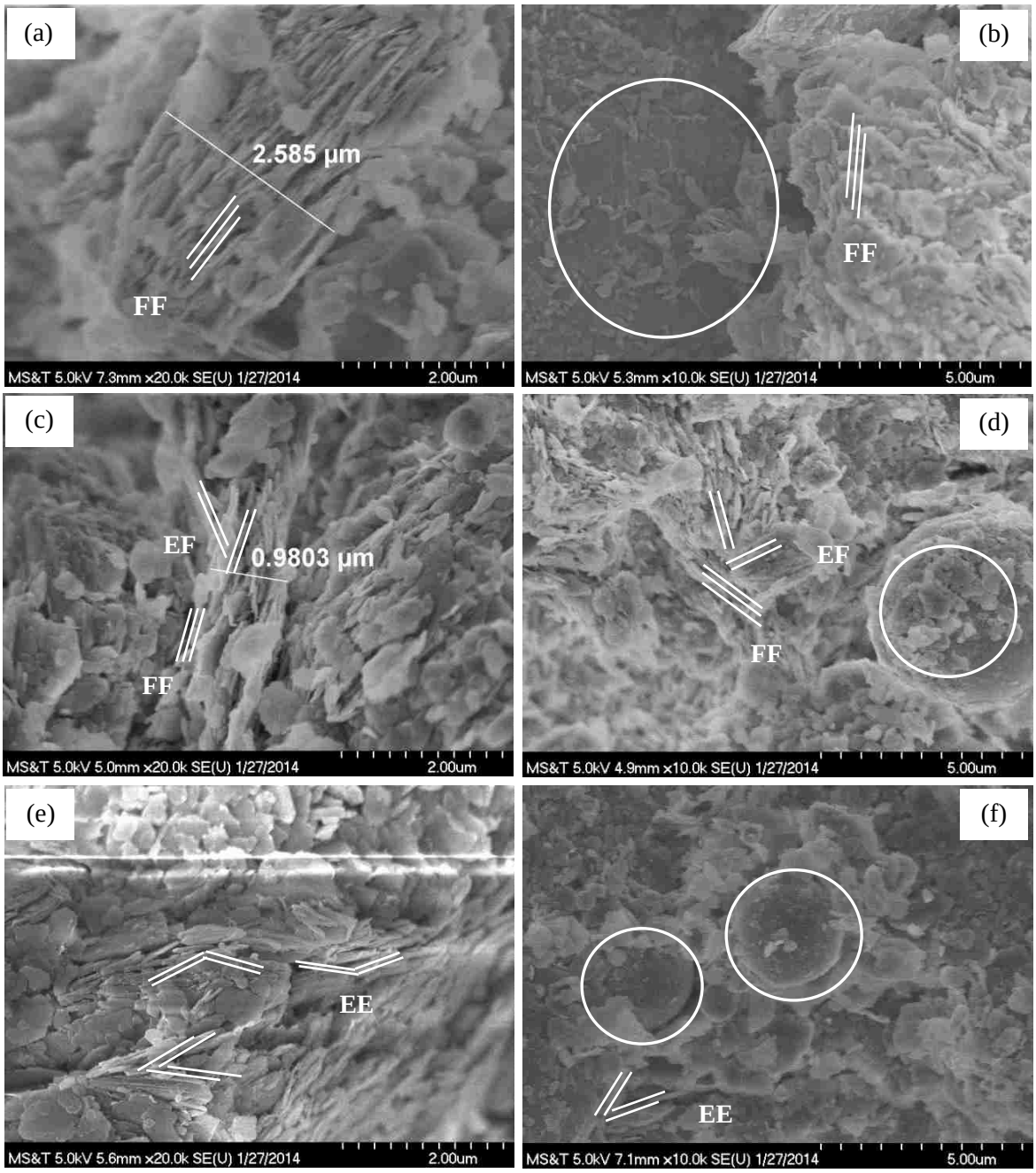

Figure 5-5 SEM images of kaolinite modified by (a) PEO; (c) chitosan; (e) xanthan gum, and SEM images of 30% fly ash-kaolinite mixtures modified by (b) PEO; (d) chitosan; (f) xanthan gum.

5.4.3. One-Dimensional Consolidation. The effective specific gravity of the fly ash, which was subsequently used to calculate the void ratios of fly ash-kaolinite mixtures, was measured to be 2.7 which agrees with the literature data (1.20 to 3.10) by Bachus and Santamarina (2012), Lacour (2012), and Foster et al. (2014). The initial void ratios (e_0) of the fly ash-kaolinite specimens at the first loading step (applied vertical stress of 16 kPa; friction corrected mean normal effective stress in the range of 10.4 - 12.5 kPa) were listed in Table 5-1. As fly ash content increased from 0% to 60% then to 100%, e_0 first decreased then remained constant (Figure 5-6a). The addition of xanthan gum induced higher initial void ratio (increased from 1.07 to 1.34), while the addition of PEO and chitosan induced lower initial void ratio (Figure 5-6b, and Table 5-1).

The compression index (C_c) and recompression index (C_r) of unmodified kaolinite sample are 0.37 and 0.12, respectively (Table 5-1). As fly ash content increased, the compression and recompression indices decreased gradually (Table 5-1, Figure 5-6a). The addition of chitosan and PEO did not change the compression index of 30% fly ash-kaolinite mixture but slightly reduced the recompression index (Table 5-1). On the other hand, the addition of xanthan gum largely increased the compression index (from 0.33 to 0.45) and recompression index (increased from 0.05 to 0.06, Figure 5-6b, and Table 5-1). Preconsolidation stresses ($\sigma_c^{'}$) of the mixtures, interpreted using the Casagrande's method, were ranged from 95-110 kPa, which agreed with the actual vertical loading during slurry consolidation (100 kPa). The addition of PEO and Chitosan did not change the preconsolidation stress of the mixtures, while the addition of xanthan gum reduced the preconsolidation stress to 85 kPa.

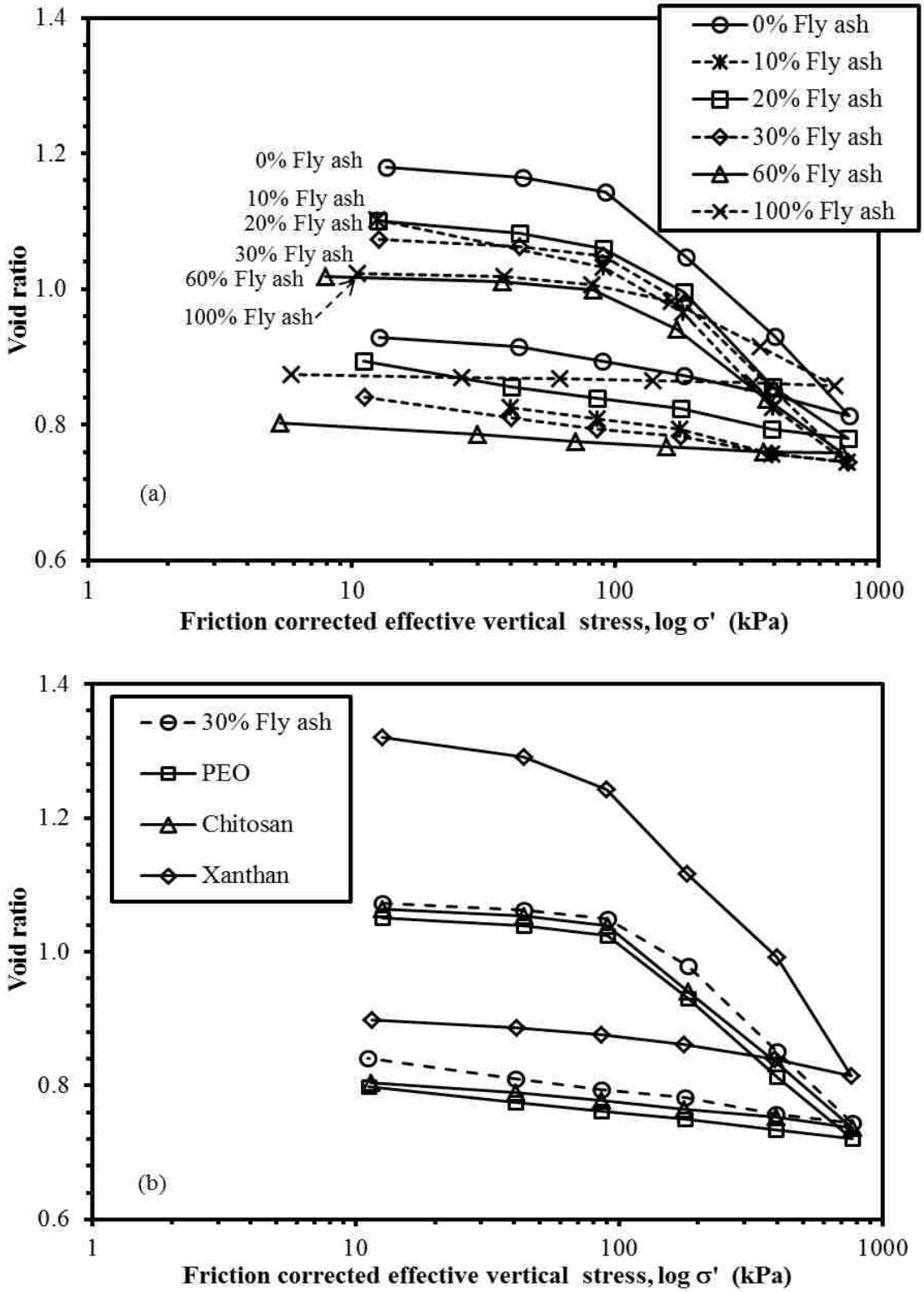

Figure 5-6 *e*-log p' curves of fly ash-kaolinite mixtures and organically modified 30% fly ash-kaolinite mixtures.

Table 5-1 Initial void ratio, compression, and recompression indices of fly ash-kaolinite mixtures and organically modified 30% fly ash-kaolinite mixtures

Fly ash ratio/Organic concentration	C_c	C_r	$\sigma_c^{'}$ (kPa)	e_0
0 % Fly ash (pure kaolinite)	0.37	0.12	95	1.19
10 % Fly ash-kaolinite	0.36	0.07	99	1.13
20 % Fly ash-kaolinite	0.35	0.06	105	1.11
30 % Fly ash-kaolinite	0.33	0.05	103	1.10
60 % Fly ash-kaolinite	0.26	0.02	105	1.02
100 % Fly ash	0.17	0.01	110	1.03
PEO 1.0g/l + 30 % Fly ash-kaolinite	0.33	0.04	97	1.06
Chitosan 1.0g/l + 30 % Fly ash-kaolinite	0.32	0.04	98	1.07
Xanthan gum 1.0g/l + 30 % Fly ash-kaolinite	0.45	0.06	85	1.34

5.4.4. Typical V_s and V_s Anisotropy Results. Typical measured V_s versus the friction corrected mean normal effective stress in the polarization plane ($\sigma_{corr}^{'}$) relationship of the fly ash-kaolinite mixtures were shown in Figures 5-7 and 5-8. Several general observations were made: (1). V_s was found to increase during loading and decrease during unloading (Figures 5-7 and 5-8). (2). Under the same stress, V_s during unloading was higher than the V_s during loading (Figure 5-7). (3). As fly ash content increased, the measured V_s increased (Figure 5-8).

Addition of fly ash to kaolinite significantly affected its V_s anisotropy. By plotting the shear wave velocity ratios of V_{s-hh}/V_{s-vh} and V_{s-hv}/V_{s-vh}, V_s anisotropy of fly ash-kaolinite mixtures is clearly shown in Figure 5-9. The following trends were identified: (1) As $\sigma_{corr}^{'}$ increased, V_s anisotropy increased (indicated by the increase of the ratios of V_{s-hh}/V_{s-vh} and V_{s-hv}/V_{s-vh}; Figure 5-9a). (2) The ratio of V_{s-hh}/V_{s-vh} (i.e., 10% fly ash-

kaolinite sample, V_{s-hh}/V_{s-vh} =1.59 at $\sigma'_{corr} = 624kPa$) in general is higher than the ratio of V_{s-hv}/V_{s-vh} (i.e., 10% fly ash-kaolinite sample, V_{s-hv}/V_{s-vh} =1.22 at $\sigma'_{corr} = 624kPa$) during both loading and unloading stages. (3) As the fly ash content increased, the V_s anisotropy decreased (Figures 5-9a and 5-9b). Under the highest σ'_{corr}, for example, the ratio of V_{s-hh}/V_{s-vh} and V_{s-hv}/V_{s-vh} of the 60% fly ash-kaolinite mixture are 1.10 and 0.99, respectively. The ratio of V_{s-hh}/V_{s-vh} and V_{s-hv}/V_{s-vh} of 10% fly ash-kaolinite mixture, however, were 1.55 and 1.22. (4) During unloading, the V_s anisotropy of 60% fly ash-kaolinite mixture almost vanished as the stress removed, however, the V_s anisotropy of 10% fly ash-kaolinite mixture retained.

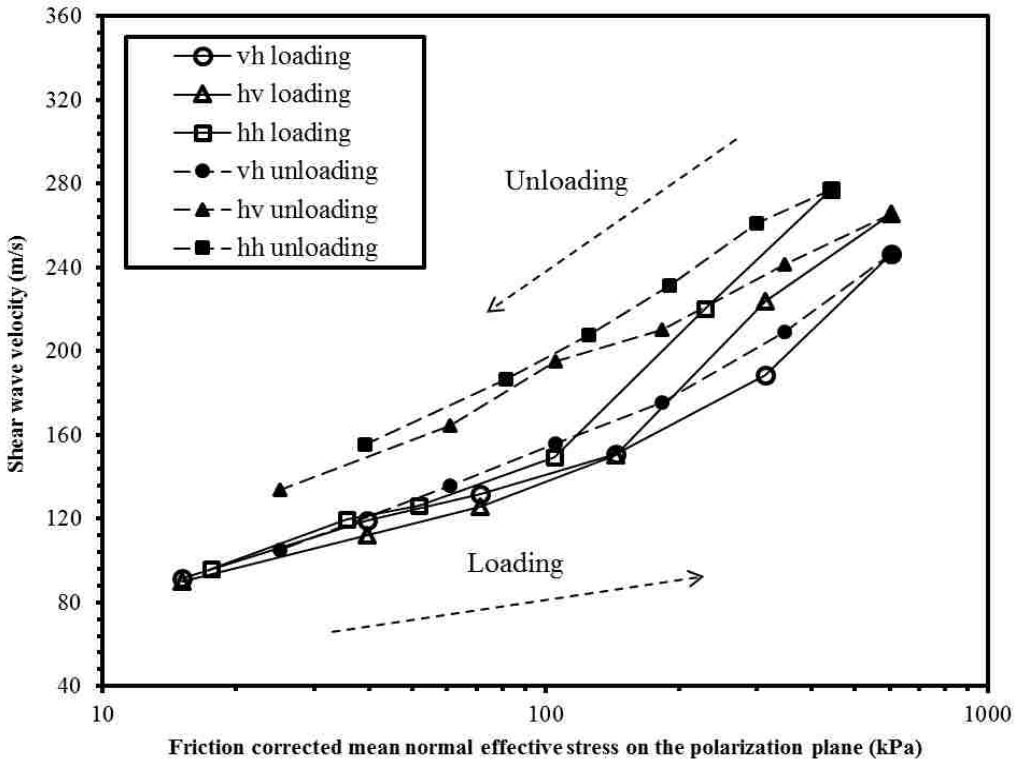

Figure 5-7 V_s in *vh*, *hv*, and *hh* directions of 30% fly ash-kaolinite mixtures during loading and unloading stages.

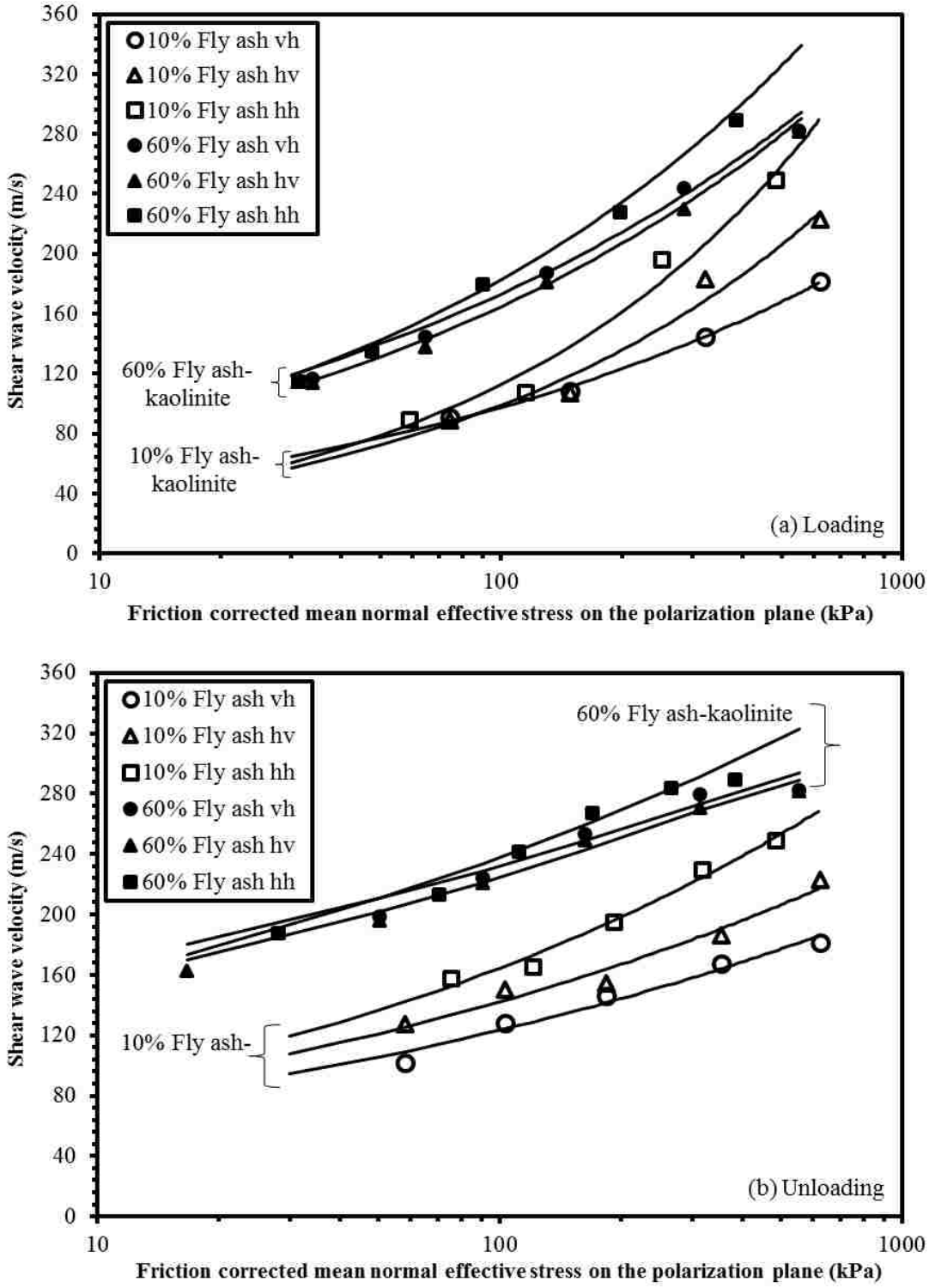

Figure 5-8 V_s in *vh*, *hv*, and *hh* directions of fly ash-kaolinite mixtures during (a) loading; and (b) unloading stages. The symbols represent test data points and solid lines represent fitting results by Eq. 5-3 by least square method. Data during the loading and unloading stages were fitted separately and high R^2 values (0.9025-0.9970) were achieved.

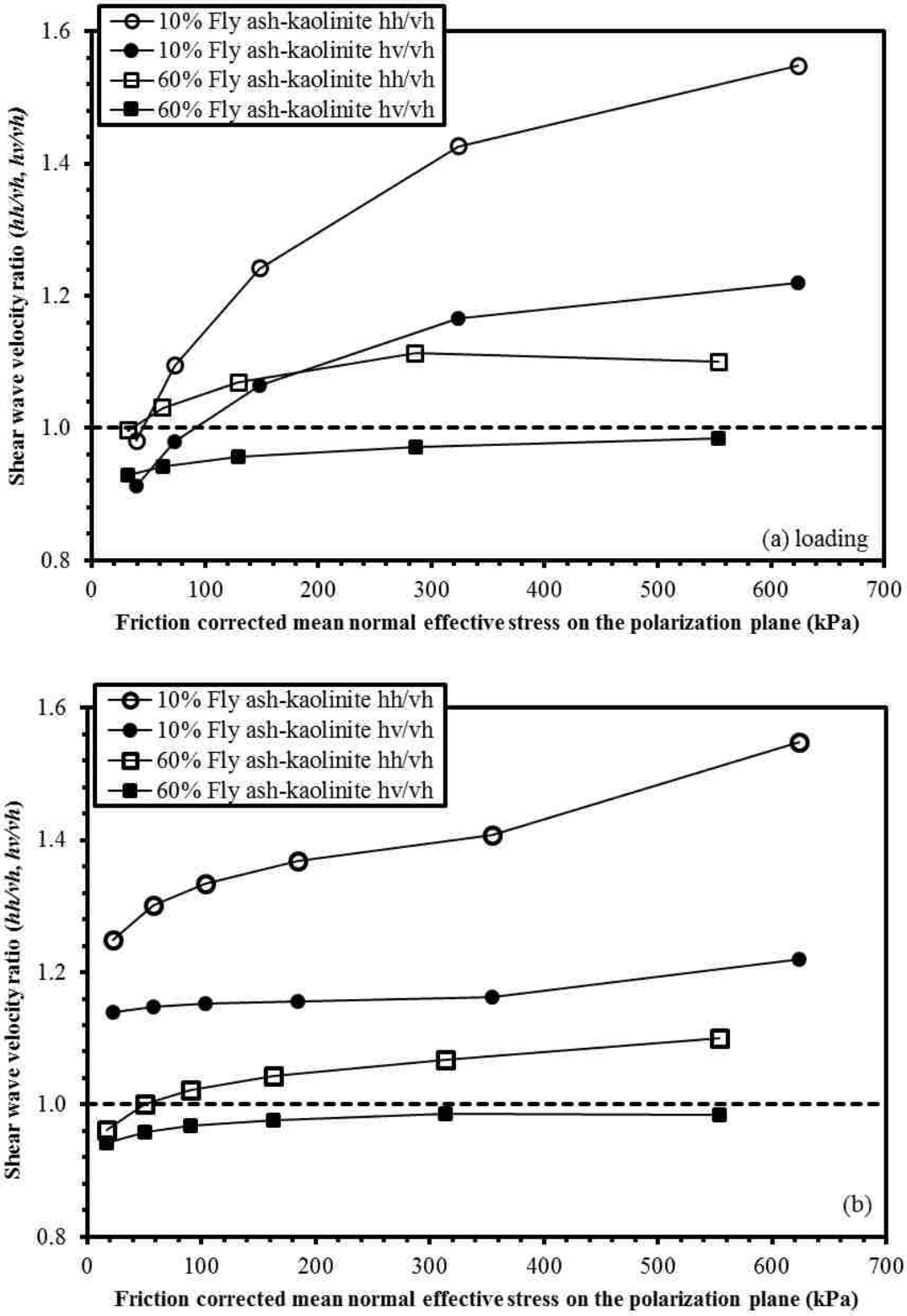

Figure 5-9 V_{s-hh}/V_{s-vh} and V_{s-hv}/V_{s-vh} of fly ash-kaolinite mixtures at 10% and 60% fly ash contents during (a) loading; and (b) unloading conditions.

5.4.5. V_s and V_s Anisotropy of Organically Modified Soil. Shear wave velocity behavior of polymer modified 30% fly ash-kaolinite mixtures (Figures 5-10 and 5-11) followed the same trends as those of unmodified fly ash-kaolinite mixtures. However, the V_s anisotropy behaviors have been significantly influenced by the addition of polymers (Figures 5-12a, and 5-12b).

The addition of PEO and Chitosan increased V_s by as much as 16%. On the contrary, the addition of xanthan gum decreased V_s by as much as 23%. The differences among the V_{s-hh}, V_{s-vh}, and V_{s-hv} for both PEO and xanthan gum treated soil increased as loading increased, while they kept approximately constant as the load was removed (Figures 5-11a and 5-11b).

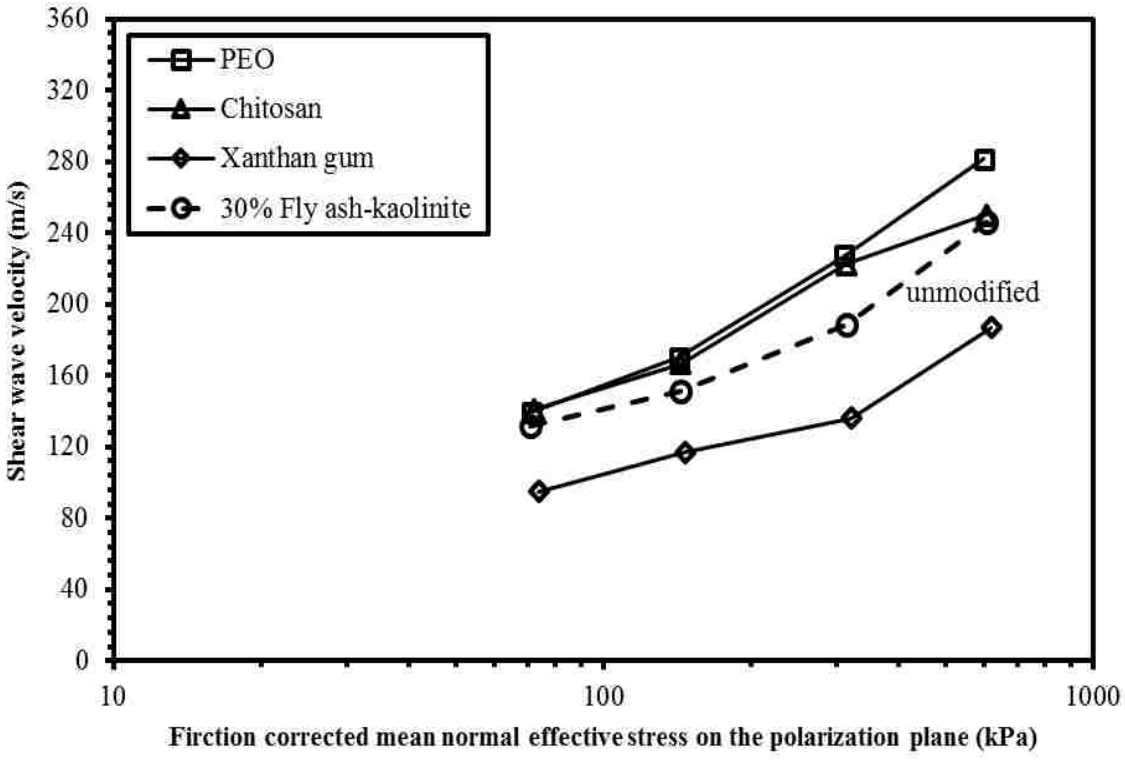

Figure 5-10 The V_{s-vh} of organically modified fly ash-kaolinite mixtures during loading.

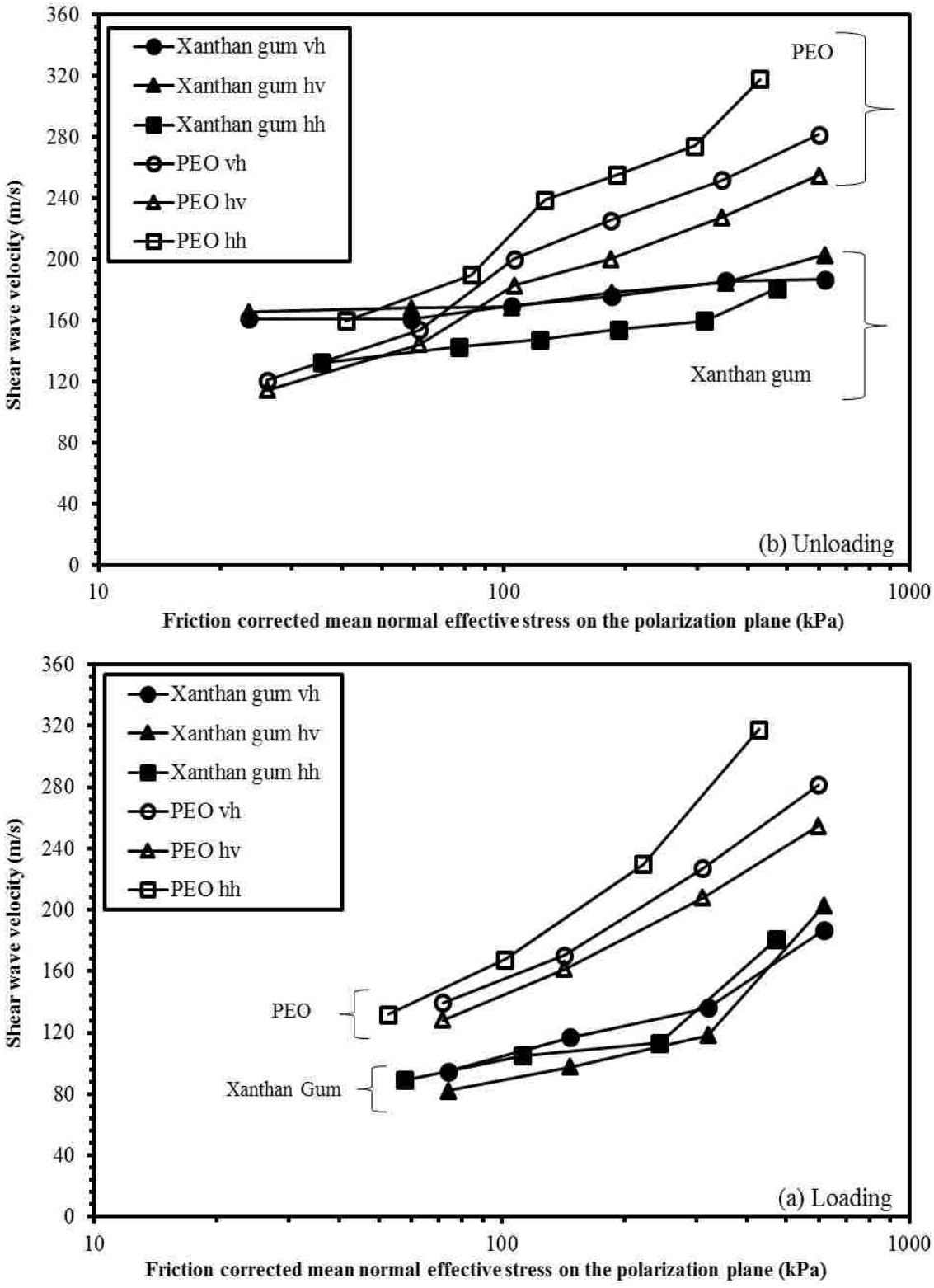

Figure 5-11 The V_s of PEO, Xanthan gum modified 30 % fly ash-kaolinite mixtures in vh, hv, and hh directions during (a) loading condition, and (b) unloading condition.

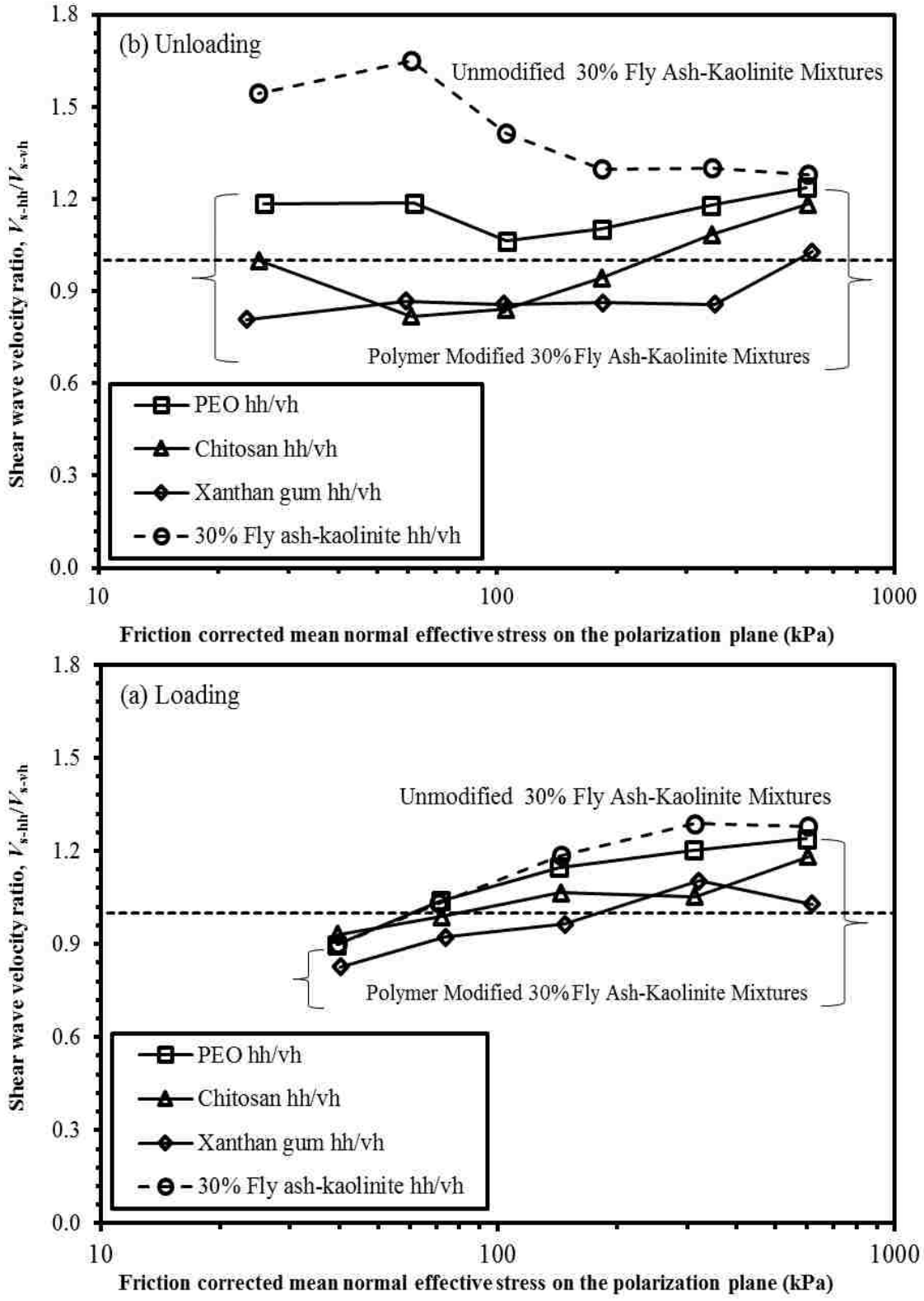

Figure 5-12 V_{s-hh}/V_{s-vh} of 30% fly ash-kaolinite mixtures modified by different polymers during (a) loading; and (b) unloading conditions.

Comparing to unmodified 30% fly ash-kaolinite mixture, the V_s anisotropy, in terms of V_{s-hh}/V_{s-vh} values, decreased by the addition of polymers (Figures 5-12). In general, the ability of reducing V_s anisotropy by polymers is ranked in the decreasing order of xanthan gum, chitosan and PEO (Figure 5-12). $V_{s\text{-}hh}/V_{s-vh}$ of xanthan gum and chitosan treated fly ash-kaolinite mixtures were lower than 1.0 during unloading (Figure 5-12b), which indicated that the V_s anisotropy has been reversed when the loading is reduced.

5.5. DISCUSSIONS

5.5.1. Threshold Fly Ash Content (F_{th}). A threshold fly ash content (F_{th}) at approximately 60% was identified, before and after which noticeable changes to the V_s values and V_s anisotropy behaviors of fly ash-kaolinite mixtures were observed (Figure 5-13). It is noted that V_s in *vh*, *hv*, and *hh* directions at σ'_{corr} of 600 kPa of fly ash-kaolinite mixtures at different fly ash contents in Figure 5-13 were obtained by fitting the measured V_s with Equation 5-3. This section focuses on V_s value changes, while the V_s anisotropy behaviors will be elaborated in a later section. As fly ash content increased from 10% to 60%, V_s values increased monotonically (Figure 5-13). As fly ash content increased from 60% to 100%, V_s values either reached a plateau or decreased slightly. It is hypothesized the observed threshold fly ash content is related to the onset of continuous fly ash particle contacts throughout the sample, exceeding which the external forces were mainly taken by the chains of fly ash particles. Packing models is proposed to estimate the value of this threshold fly ash content. It is assumed that (1) all fly ash particles are cenospheres of the same geometry with an outer diameter of 0.028 mm (i.e. d_{50}, Figure 5-2) and a shell thickness of 0.0033mm (from SEM results; see Shell

Thickness section); (2) at this threshold fly ash content, the inside of the cenospheres are filled with water only (i.e., no kaolinite), while the void space between cenospheres is filled with saturated kaolinite whose void ratio equal to that under the same stress. Based on above assumptions, simple cubic packing (the loosest state) and face-centered packing (the densest state) represent the lower and upper bounds of all the possible packing densities, respectively. The lower and upper bounds of the threshold fly ash contents at $\sigma'_{corr} = 600kPa$ were calculated to be 53.1% and 74.6% respectively (see appendix), which agrees well with the observed threshold fly ash content (around 60%) (Figure 5-13). This agreement validates the hypothesis that the threshold fly ash content corresponds to the onset of continuous fly ash particle contacts throughout the mixture. The shear wave velocity behavior with fly ash content can then be explained as follows. Because fly ash ($G_{\max}$ ranges from 38-156 MPa, σ_v =100-800 kPa) (Kang 2015) is stiffer than the saturated kaolinite ($G_{\max}$ ranges form 3-40 MPa, σ_v =100-800 kPa), addition of fly ash to kaolinite leads to increment of V_s until reaching the threshold fly ash content (approximately ranging from 53.1% to 74.6%). Exceeding the threshold fly ash content, V_s value is influenced by two mechanisms: (1) increase of the fly ash packing density, i.e. the number of fly ash cenospheres per unit volume, increases V_s and (2) decrease of kaolinite content, especially those at the contacts between fly ash particles (given the same fly ash packing density) decreases V_s. For example, the calculated packing density increases from 39176 cenospheres/ mm^3 to 63692 cenospheres/ mm^3 as fly ash content increases from 60% to 100%. However, due to the loss of kaolinite from 40% to 0%, the net effect is either decreased V_s (in *hh* direction) or constant V_s (Figure 5-13).

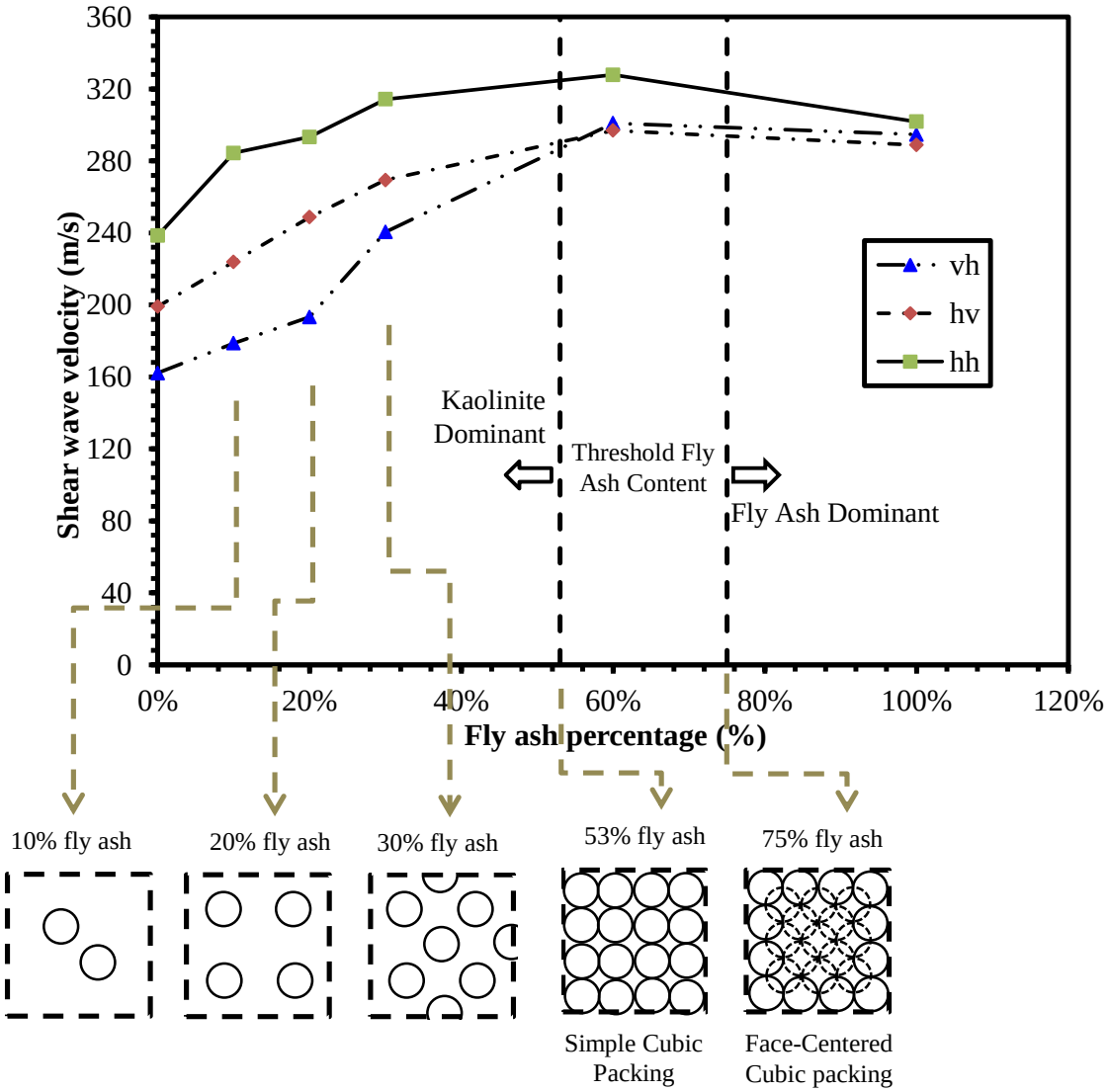

Figure 5-13 The shear wave velocity changes in *vh*, *hv*, and *hh* directions of fly ash-kaolinite mixtures at different fly ash mixing ratios at $\sigma'_{corr} = 600kPa$; the insets illustrate the volumetric content of fly ash cenospheres in the fly ash-kaolinite mixtures.

5.5.2. Effect of Fly Ash Content on the V_s Anisotropy. V_s anisotropy of a soil originates primarily from fabric anisotropy and stress anisotropy (Bellotti et al. 1996; Pennington et al. 1997; Santamarina et al. 2001; Wang and Mok 2008). The influence of

fly ash content on the V_s anisotropy of fly ash-kaolinite mixtures is quantitatively illustrated in Figure 5-14 and 5-15.

It is noted that the shear wave velocity ratios in Figure 5-14 and Figure 5-15 were plotted under the same mean normal effective stresses in the polarization plane using the fitted data by Equation 5-3. Thus the effect of stress anisotropy is removed and the V_s anisotropy is primarily resulted from fabric anisotropy. It is observed that V_s anisotropy is prominent at high stress and low fly ash content. For example, V_{s-hh}/V_{s-vh} at σ'_{corr} = 600 kPa and 10% fly ash content is 1.59. High V_s anisotropy is attributed to the high volume fraction of kaolinite particles, whose preferential alignment in horizontal direction becomes more significant with higher loading in one-dimensional consolidation (Bellotti et al. 1996; Pennington et al. 1997; Santamarina et al. 2001; Wang and Mok 2008). V_s anisotropy gradually decreased as fly ash content increased, and diminished once past the F_{th}. At σ'_{corr} = 600 kPa, V_{s-hh}/V_{s-vh} reduced to 1.31, 1.09 and 1.01 when fly ash content increased to 30%, 60% and 100%, respectively. Decrement of V_s anisotropy is due to the addition of nearly spherical fly ash cenospheres, which have little to none fabric anisotropy. Similar trends were observed for other mean normal effective stresses (Figure 5-14a) and for unloading cases (Figure 5-14b).

One exception is spotted where reversal trend of V_{s-hh}/V_{s-vh} values were observed at 20% and 30% fly ash contents under 200 kPa unloading stress (Figure 5-14b). The possible reason of the reversal is that Equation 5-2 may not accurately predict K_0 in calculating σ'_{corr} during unloading, where complicated stress conditions may develop and stress interlocking may occur (Wijewickreme et al. 2009; Yun and Santamarina 2005).

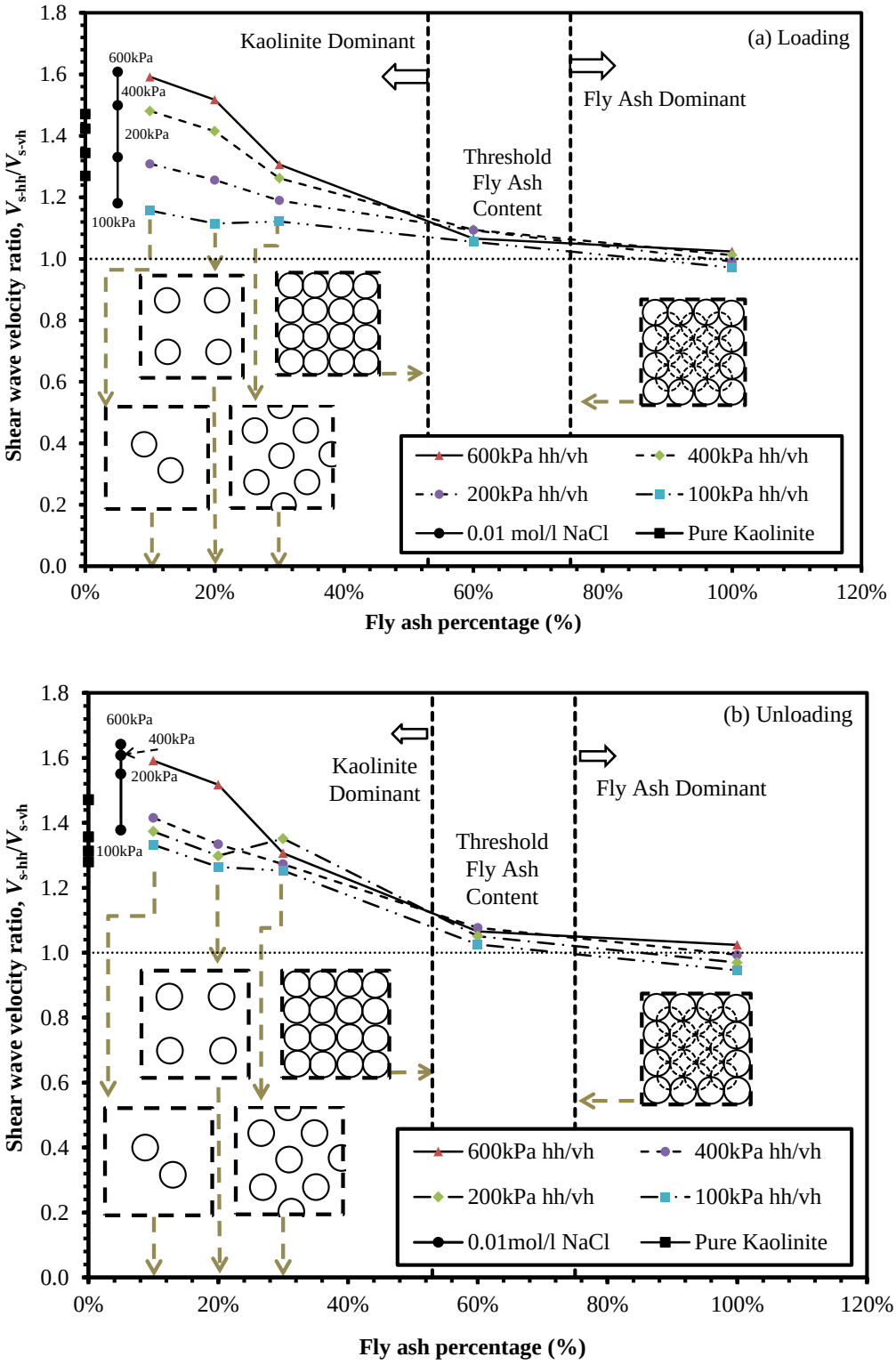

Figure 5-14 V_{s-hv}/V_{s-vh} of fly ash-kaolinite mixtures at different fly ash contents (0% - 100%) during (a) loading; and (b) unloading conditions.

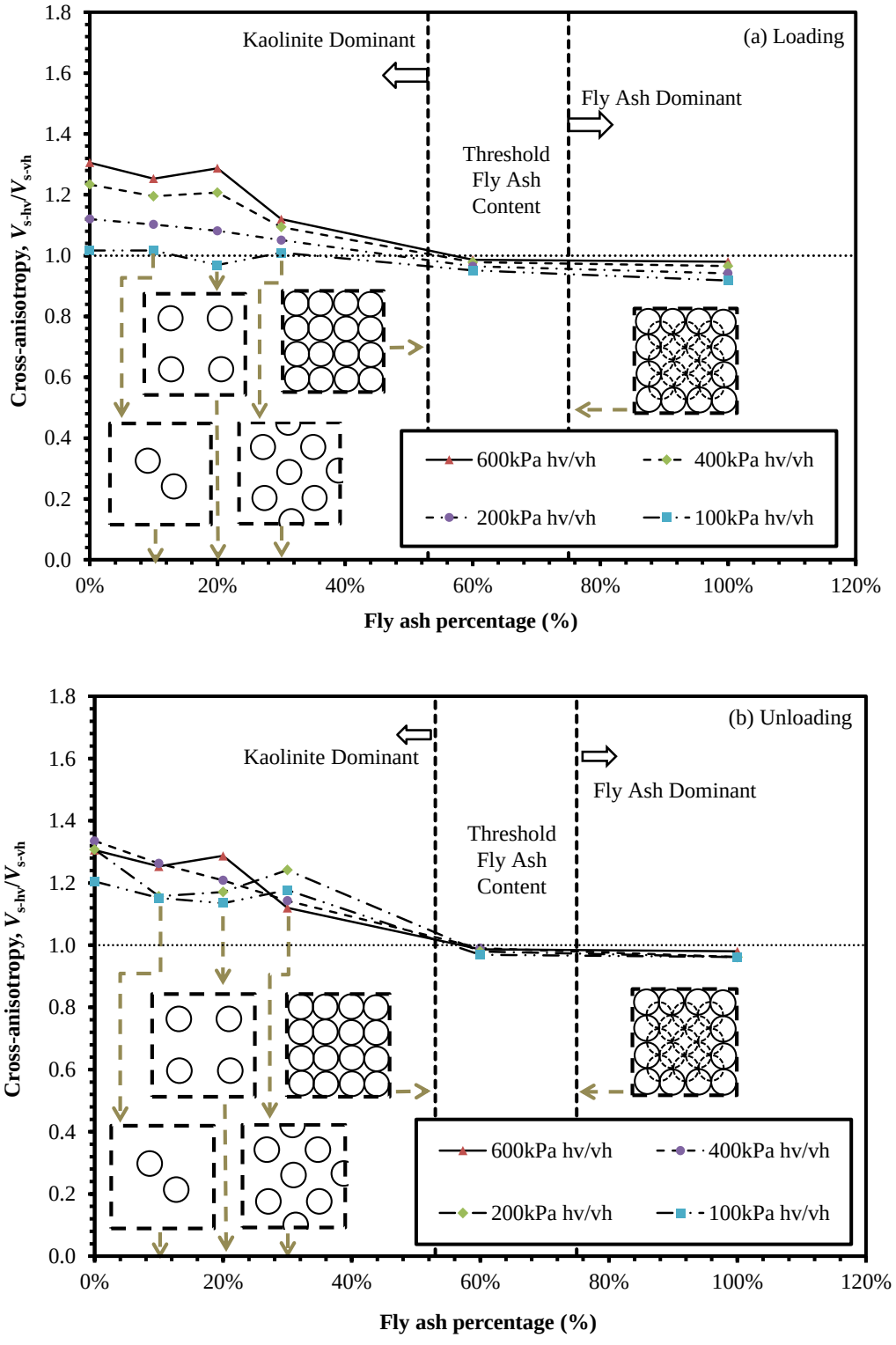

Figure 5-15 Shear wave velocity ratio V_{s-hv}/V_{s-vh} of fly ash-kaolinite mixtures at different fly ash contents during (a) loading and (b) unloading conditions.

5.5.3. Ionic Strength Effects on V_s Anisotropy. It was observed in a prior study that ionic strength increased the V_s anisotropy of kaolinite (Kang et al. 2014). This observation was confirmed in this study, as the use of 0.01 mol/l NaCl solution in kaolinite increased V_s anisotropy (Figures 5-14a and 5-14b). According to the fabric map of kaolinite (Palomino and Santamarina 2005), 0.01 mol/l NaCl solution induces more aggregated edge-to-edge (EE) kaolinite particle association, which is easier to align horizontally under high vertical load (> 200 kPa) than the dispersed kaolinite particle association in deionized water. On the other hand, it is concluded from previous section that the addition of fly ash decreased V_s anisotropy due to its spherical shape. However, 10% fly ash-kaolinite mixture had more V_s anisotropy than kaolinite in deionized water did (Figure 5-14). This result suggested that the ions released from Class F fly ash increased the ionic strength, whose effects on V_s anisotropy outweighed the spherical shape-induced reduced fabric anisotropy, and increased V_s anisotropy of 10% fly ash-kaolinite mixture.

5.5.4. Cross-Anisotropy. Cross -anisotropy, the material properties at *vh* and *hh* directions equal, is often assumed in many geotechnical problems (Yimsiri and Soga 2000). By means of shear wave velocity ratio V_{s-hv}/V_{s-vh}, this section will quantitatively evaluate the cross-anisotropy behavior of fly ash-kaolinite mixtures. At high stress (σ'_{corr} > 200 kPa) during loading or at any stress during unloading, V_{s-hv}/V_{s-vh} of the mixtures is higher than unity at kaolinite dominant zone (fly ash content < F_{th}), which means the mixtures are not cross-anisotropic (Figure 5-15). For example, V_{s-hv}/V_{s-vh} decreased from 1.30 to 0.98 as fly ash content increased from 0% to 60% (i.e. near F_{th}) at = 600 kPa (Figure 5-15). At kaolinite dominant zone, higher stresses during loading

normally developed higher V_{s-hv}/V_{s-vh} values (Figure 5-15a). Once the fly ash content exceeded F_{th}, V_{s-hv}/V_{s-vh} became close to unity, irrespective of the applied stress values. This means that the fly ash-kaolinite mixtures are cross-anisotropic. Round sand was reported as a cross-anisotropic material in the literature (Bellotti et al. 1996; Wang and Mok 2008). The shape of fly ash cenospheres is similar to that of the round sand, which makes fly ash cenospheres cross-anisotropic. On the other hand, platy-shaped kaolinite particles align preferentially under high loading (> 200 kPa) (Bellotti et al. 1996; Kang et al. 2014; Santamarina et al. 2001; Wang and Mok 2008), and therefore are not cross-anisotropic. Consequently, fly ash-kaolinite mixtures are not cross-anisotropic in kaolinite dominant zone (fly ash content < F_{th}) (except for σ'_{corr} < 100 kPa during loading, where preferential alignment is not developed), and become cross-anisotropic at F_{th} and fly ash dominant zone (fly ash content > F_{th}). Reversals of above-mentioned trends were observed at 30% fly ash contents during unloading (Figure 5-15), which, again, is attributed to the limitation of Equation (2) in representing complicated stress conditions as discussed in previous section.

5.5.5. Effects of Polymers on the V_s and V_s Anisotropy. For the organically modified 30% fly ash-kaolinite mixture, polymers will interact with both the fly ash (at macro-grain-scale, refer to polymer induced "cohesion") (Cole et al. 2012) and kaolinite (at microscale, i.e., polymer bridging) (Nasser and James 2006; Nugent et al. 2010; Ringelberg et al. 2014; Tan et al. 2014). Chang et al. (2015) reported that the polymer-clay interactions govern the overall behavior when clay (kaolinite) content is high ($\geq$60% by weight), where the formation of the biopolymer-clay matrices is the major contribution to the increase of strength. Since 30% fly ash-kaolinite mixture has high clay

content (70% kaolinite by weight), the mechanical changes due to polymer-kaolinite interactions are expected to dominate the overall behavior of the organically modified 30% fly ash-kaolinite mixtures.

The V_s increase (16%, Figure 5-10) of PEO modified 30% fly ash-kaolinite mixture is attributed to "polymer bridging". PEO chains served as "adhesive bonding" between soil particles (Mpofu et al. 2004; Swenson et al. 1998), which increased the interparticle attractive forces. Macroscopically, this was equivalent to an increase in effective stress, which improved the stiffness of geomaterials (Cho and Santamarina 2001). In addition, "polymer bridging" induced densely-compacted and larger kaolinite aggregates (Figure 5-5). The typical aggregate size of PEO modified fly ash-kaolinite mixture reached 2.585 um, which is eight times larger than the d_{50} of unmodified kaolinite (Figure 5-5). Large and compacted aggregates might contribute to the V_s increment even if the bulk void ratio remained almost constant (Table 5-1) (Zhan et al. 2013).

Chitosan was also found to increase the V_s of 30% fly ash-kaolinite mixtures, but to a lesser extent compared to PEO (Figure 5-10). Positively charged chitosan will firstly interact with negatively charged kaolinite through Coulombian attraction (charge neutralization). Charge neutralization would not bind kaolinite particles together and therefore would not induce large compacted aggregates (Huang and Chen 1996; Parazak et al. 1988; Zhang et al. 2013). Beside, charge neutralization process might reduce the number of available polymers that participate in the secondary interaction - polymer bridging (such as hydrophobic interactions and hydrogen bonds) (Kim and Yang 2012; Tan et al. 2014). As a result, given the same dosage, the polymer bridging effect of

Chitosan is weaker than PEO. This could be shown by the small aggregate size (0.980 μm) by chitosan modified 30% fly ash-kaolinite mixture (Figure 5-5c). In addition, a recent study from Wang et al. (2015) suggested that high salinity conditions (0.01-1.0 mol/l NaCl), under which the aggregation tendency of chitosan polymer chains leads to fewer polymer chains available to bind with kaolinite particles, thus weaken the "bridging" effect of chitosan. Since the fly ash hydration increases the ionic strength in the pore fluid (the ionic strength of 30% fly ash solution is equivalent to the ionic strength 0.01 mol/l NaCl), it weakens the "bridging" performance of chitosan, thus compromises the kaolinite aggregates size (0.980 μm , Figure 5-5c) and V_s increase (Figure 5-10).

The V_s of 30% fly ash-kaolinite mixtures decreased by 23% when treated with xanthan gum polymer (Figure 5-10), which could be attributed to the following two reasons. The interparticle forces are dominated by strong electrostatic repulsion forces that exist between negatively charged xanthan gum and negatively charged kaolinite (Benchabane and Bekkour 2006; Zhang et al. 2013). Macroscopically, this is equivalent to a decrement of effective stress, which in turn leads to a decrease of V_s. Beside, xanthan gum chains, attracting positively-charged edges of kaolinite and repelling negatively-charged faces of kaolinite via electrostatic attraction (Benchabane and Bekkour 2006; Tan et al. 2014; Zhang et al. 2013), induced a loose layered kaolinite fabric (Labille et al. 2005) (Figure 5-5f). As a result, the bulk void ratio increased dramatically (by 22%, Table 5-1), and the V_s decreased by 23% (Figure 5-10).

The V_s anisotropy of fly ash-kaolinite mixtures was reduced by the addition of PEO, chitosan or xanthan gum (Figure 5-12), which could be attributed to reduction of

fabric anisotropy and reduction of stress anisotropy. Fabric anisotropy was reduced due to changes of the fabric of kaolinite aggregates. In the case of PEO or chitosan modification, the size of kaolinite aggregates was increased by "polymer bridging" (Figure 5-5), where compacted and large aggregates were formed with small aspect ratio (less platy like unmodified kaolinite particles). The reduction of aspect ratio decreased the fabric anisotropy. Thus, V_s anisotropy of organically modified fly ash-kaolinite mixtures decreased in both loading and unloading conditions (Figures 5-12a and 5-12b). In the case of xanthan gum modification, dispersed and thin-layered fabrics (SEM images, Figure 5-5) were observed even under the highest applied stresses in this study, which prevents preferential alignment. As a result, V_s anisotropy is less apparent than unmodified fly ash-kaolinite mixture. On the other hand, stress anisotropy was reduced due to the decrease of coefficient of lateral earth pressure at rest, K_0, by polymers. PEO and chitosan increased the critical state friction angle (ϕ') (Kang 2015), and led to decrease in K_0 according to Jaky's Equation ($K_0 = 1 - \sin\phi'$). Consequently, the mean normal effective stress in *hh* direction is reduced, which leads to the decrease of V_{s-hh}, and eventually to the reduction of V_s anisotropy (V_{s-hh} / V_{s-vh}, Figure 5-12a).

5.5.6. Stress Dependence of V_s. The stress dependence of V_s could be expressed by Equation 5-3 (Santamarina et al. 2001). The coefficient β is theoretically related to the contact effects. An β value of 1/6 represents the Hertzian contact (elastic spheres), 1/4 represents the cone-to-plane contacts (rough or angular particles) or spherical particles with contact yield, and 3/4 represents the contacts governed by Coulombian forces (Santamarina et al. 2001). α and β parameters were fitted with Equation 5-3 by least

square method (Solver function in Microsoft Excel) (see Figures 5-16a and 5-16b). Data during the loading and unloading stages were fitted separately. High R^2 values (0.9025 - 0.9970) of the fitting suggested a good agreement between the measured data and Equation 5-3.

For kaolinite particles, overconsolidation shrinked the electrical double layer and increases the particle contacts. For fly ash particles, overconsolidation increased packing density (Figure 5-6). Both mechanisms yield stiffer particulate material than their normally consolidated conditions, which was demonstrated by increased α values and decreased β values in general (Figures 5-16a and 5-16b).

During loading, at kaolinite dominant zone (fly ash content < F_{th}), most α and β values fall in the "loading zone" as shown in Figure 5-16a, which were characterized by low a values (α < 30) and high b values (β > 0.23); while at fly ash dominant zone (fly ash content > F_{th}), α and β values fall in the "transition zone" (Figure 5-16a), which were characterized by higher α values and lower β values than the "loading zone". During unloading, approximately monotonic trend was observed that as fly ash content increased from 0% to 100%, α values increased and β values decreased (Figure 5-16a). In both cases, the addition of fly ash to kaolinite increased the stiffness and Hertzian contacts, which were illustrated by increased α values and decreased β values, respectively. During loading, no obvious trend was observed on the effects of polymers on α and β values of 30% fly ash-kaolinite mixtures, the majority of which resided in "loading zone" and "transition zone" (Figure 5-16b). During unloading, however, higher α values and lower β values were observed in "transition zone" and "unloading zone". During unloading, in the order of xanthan gum, chitosan and PEO, α increased and β

decreased monotonically. This observation agrees with the SEM results (Figure 5-5) and previous discussions on the fabric structures of polymer modified 30% fly ash-kaolinite mixtures that, xanthan gum induced more flocculated structure (more Coulombian force) and PEO induced larger and stiffer particle (more elastic contacts). Linear and hyperbolic functions (Figures 5-16a and 5-16b) were used to fit the observed data with good *R*-squared values (ranged from 0.7587-0.9028). The resulting fitting curves in this study are similar to previous studies (Santamarina et al. 2001; Ku et al. 2011) with lower β values in overconsolidated soils. This is postulated to be the presence of fly ash particles (more Hertzian contacts).

5.5.7. Porosity Dependency of V_s. Figure 5-17 shows the relationship of shear wave velocity versus porosity of fly ash-kaolinite mixtures in the *vh* direction. Similar trends were observed for V_s in the *hv* and *hh* directions. At a given fly ash content, the V_s decreased as the porosity increased. However, the same porosity yielded different V_s values because of the different fly ash contents and applied stresses (Figure 5-17).

5.6. CONCLUSIONS

The shear wave velocity and its anisotropy of unmodified and polymer modified fly ash-kaolinite mixtures were investigated by a self-developed floating wall consolidometer type bender element testing system. The following results were concluded:

(1). The compressibility and swelling potential of fly ash-kaolinite mixtures decreased as the fly ash content increased. PEO and chitosan could reduce the compressibility and swelling potential; however, xanthan gum relatively increased the compressibility and swelling potential of the 30% fly ash-kaolinite mixture.

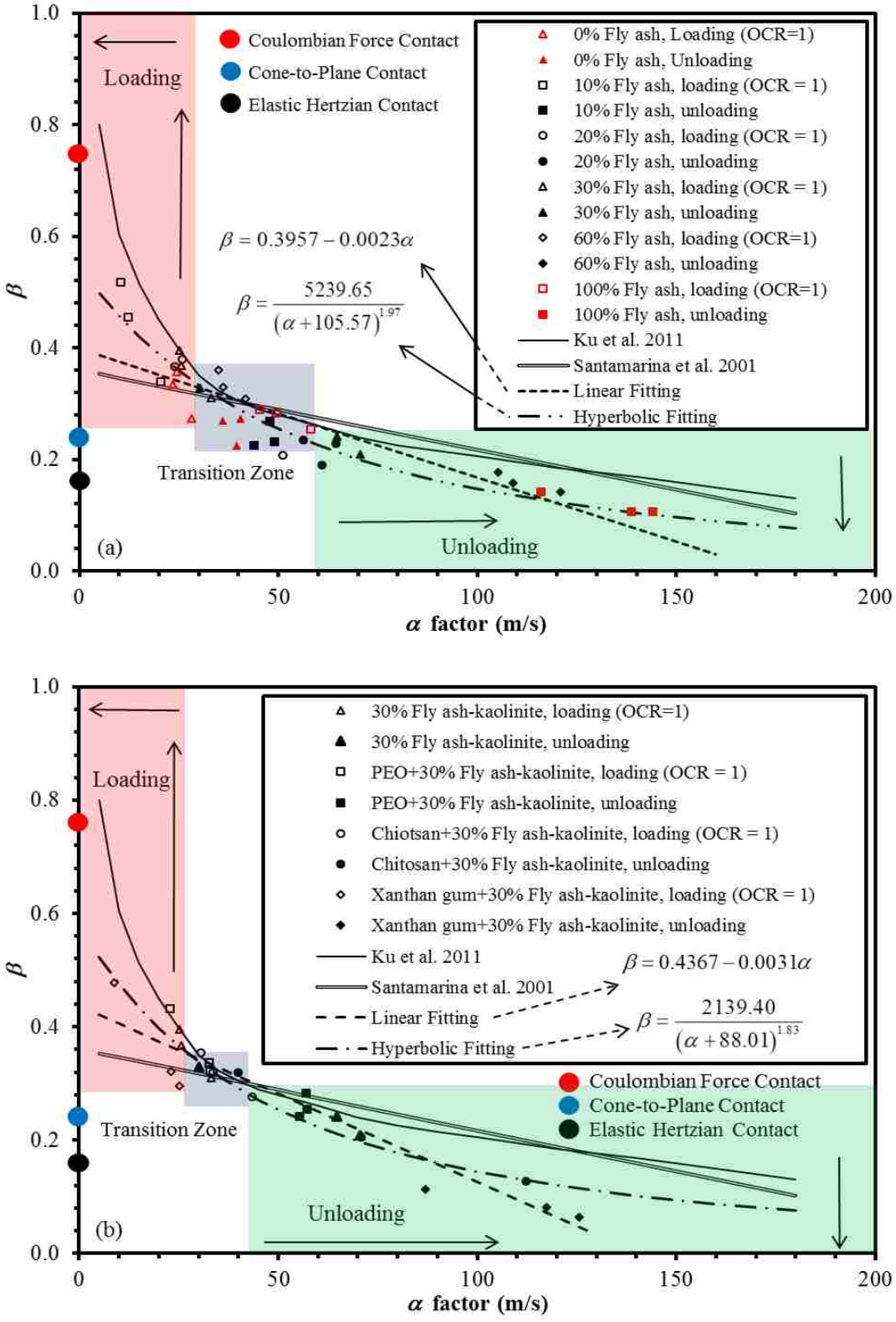

Figure 5-16 Fitted values of α and β coefficients of (a) fly ash-kaolinite mixtures; and (b) organically modified 30% fly ash-kaolinite mixtures.

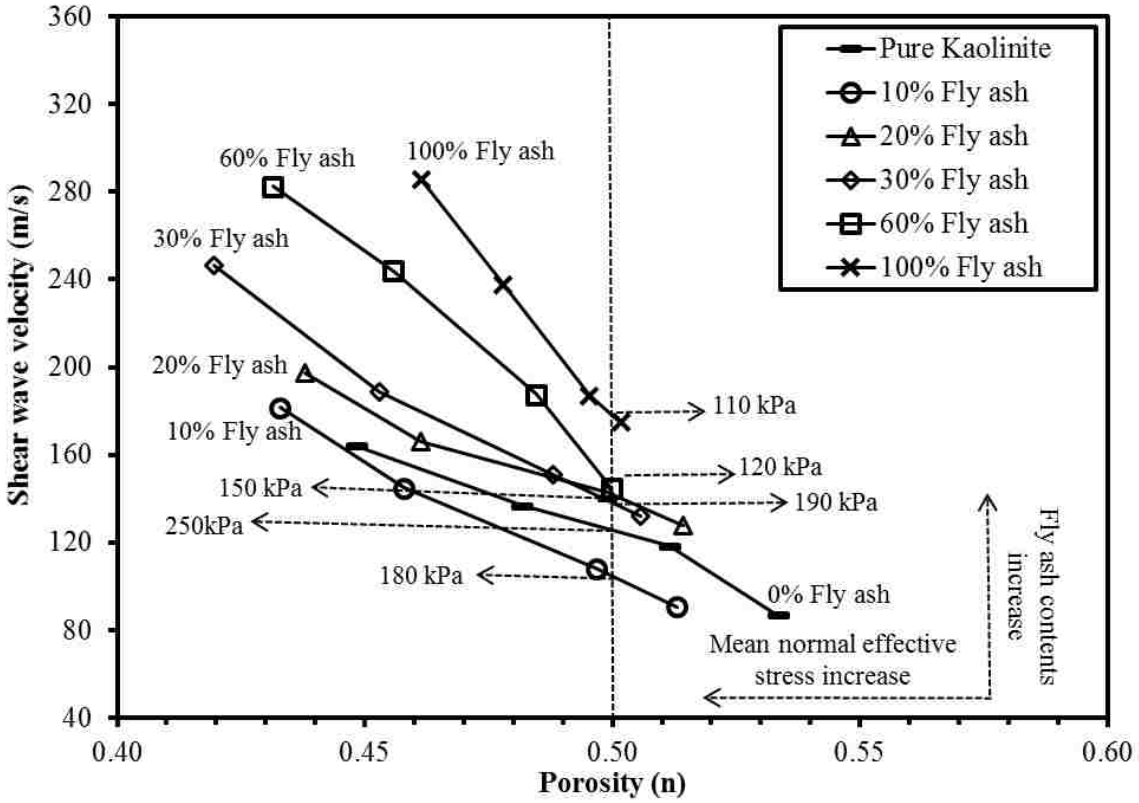

Figure 5-17 V_{s-vh} of fly ash-kaolinite mixtures during loading as a function of porosity.

(2). A threshold fly ash content (F_{th}), which corresponding to the onset of continuous contacts between fly ash particles throughout the sample, was found to exist for the V_s and V_s anisotropy behaviors of fly ash-kaolinite mixtures. Before F_{th}, as fly ash content increased, the magnitude of V_s in three orthogonal directions increased, while V_s anisotropy decreased. After F_{th}, as fly ash content increased, V_s slightly decreased or remained constant, while V_s anisotropy almost diminished.

(3). Fly ash particles are stiffer than saturated kaolinite. Therefore, the addition of fly ash particles increased the stiffness of mixture when fly ash content is below the F_{th}. After F_{th}, there are two competing mechanisms, i.e. V_s increase due to the increase of fly

ash content and V_s decrease due to the loss of kaolinite mass, especially those at fly ash particle contacts. The results suggested that the latter is more obvious.

(4). Mechanically, fly ash particles are primarily spherical, and therefore have-not fabric anisotropy. As a result, addition of fly ash particles reduces V_s anisotropy.

(5). Physicochemically, high ionic strength increased V_s anisotropy. High salt concentration (0.01 mol/l NaCl) increased the V_s anisotropy of kaolinite. The ions released from Class F fly ash increased ionic strength of the pore fluid, which, in return, increased the V_s anisotropy of fly ash-kaolinite mixtures.

(6). Cross anisotropy assumption is valid as fly ash content is higher than F_{th}, and is invalid as fly ash content is lower than F_{th}.

(7). The addition of PEO leads to larger and stiffer kaolinite aggregates due to polymer bridging, which yields higher V_s. Chitosan has similar effects to PEO on V_s values, but to a lesser extent. On the contrary, xanthan gum induced more flocculated layered structure to the kaolinite aggregates, which leads to a lower V_s.

(8). All three polymers reduced V_s anisotropy. This is attributed to the reduction of initial fabric anisotropy and the reduction of stress anisotropy (which reduces the V_{s-hh}).

6. LARGE STRAIN STRESS-STRAIN RESPONSES OF ORGANICALLY MODIFIED HIGH VOLUME CLASS F FLY ASH-KAOLINITE

6.1. INTRODUCTION

Sustainable reuse of fly ash has been gradually gaining its weight in Geotechnical Engineering applications in recent decades, such as deep soil mixing, soil replacing, and soil stabilization (Ferguson 1993; Doven and Pekrioglu 2005; Kang et al. 2013; Kang et al. 2015; Nhan et al. 1996). The reuse of fly ash has significant benefits; however, challenges exist in the high volume reuse of Class F fly ash in geotechnical engineering, for example, little cementitious effects, easy to be liquefied, drastic mechanical drop due to small variation of water content, weak water retention capacity, lack of the guidelines to characterize fly ash, and environment concerns. In spite of the advantages of organics and the successful cases in organically modified soils, studies on organically modified fly ash-soil mixtures were rarely found in the literature. Fly ash is often negatively charged, the reuse of which in geotechnical engineering could also benefit from the addition of organics through polymer bridging and electrostatic forces. Therefore, this study intended to use organic agents, which include both synthetic polymers and biopolymers, to modify the geotechnical properties of fly ash-kaolinite mixtures so as to foster high volume reuse of Class F fly ash in geotechnical engineering, i.e., soil stabilization, deep soil mixing, structural fill, landfill liners, and pavement subgrades. The objectives of this chapter are: (1) Characterize the microstructure of organically modified fly ash-kaolinite mixtures by using scanning electron microscopy (SEM) technique. (2) Investigate large strain stress-strain behaviors of organically modified fly ash-kaolinite mixtures and their dependency on the polymeric additives by conducting consolidated undrained (CU) triaxial shear test.

6.2. MATERIALS AND EXPERIMENTAL METHODOLOGY

6.2.1. Materials. Georgia kaolinite (RP-2, Active Mineral International) was used was used in this study. The kaolinite is an air-float processed clay, with a specific gravity G_s = 2.6 and an average aggregates diameter (d_{50}) of 0.00036 mm (Figure 6-1). The Fly ash used in this study is from Lafarge power plants, Wisconsin, USA. This fly ash is classified as Class F (ASTM standard C 618), which has little self-cementious property. The fly ash has an average diameter (d_{50}) of 0.028mm (Figure 6-1) and specific gravity G_s = 2.7 (Pycnometer test, ASTM D854-14). The chemical components of the fly ash and kaolinite are tabulated in Table 6-1. The major chemical components of kaolinite are Al_2O_3 (45.60%) and SiO_2 (38.40%). Large volume of amorphous chemical component (63.5%) was detected in the fly ash. Aluminum oxide (Al_2O_3) and mullite ($Al_6Si_2O_{13}$) are the major crystal components of the fly ash, which takes 16.2% and 10.1%, respectively (Table 6-1).

Table 6-1 Chemical analysis results of RP-2 kaolinite and fly ash from XRD Tests

Kaolinite		**Fly Ash**		
Chemical Component	Percentage		Chemical Component	Percentage
SiO_2	45.60%	Crystal	Al_2O_3	16.2%
Al_2O_3	38.40%		SiO_2	6.4%
Fe_2O_3	0.88%		Fe_2O_3	3.9%
TiO_2	1.69%		$Al_6Si_2O_{13}$	10.1%
CaO	0.05%			
MgO	0.02%			
K_2O	0.15%		Amorphous	63.5%
Na_2O	0.21%			
LOI	13.70%			

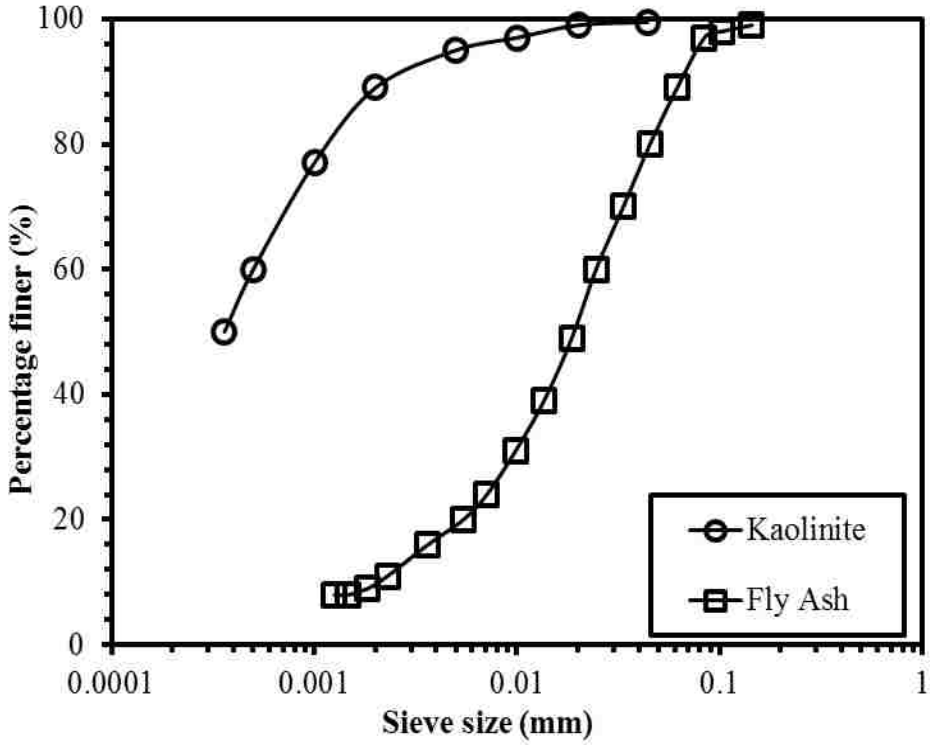

Figure 6-1 Grain size distributions of kaolinite and fly ash.

Three polymers were selected to improve the strength of fly ash-kaolinite mixtures: Nonionic Polyethylene Oxide ($(-CH_2CH_2O-)_n$, PEO), positively-charged Chitosan **(** $(C_6H_{11}NO_4)_n$ **)**, and negatively charged xanthan gum ($(C_{35}H_{49}O_{29})_n$ **)**. The chemical structures of the selected polymers are shown in Figure 6-2. PEO is perceived as a "flexible" polymer, with a structure described as a random coil and can change conformation dynamically in solution (Mpofu et al. 2004). The PEO polymer used in this research has a molecular weight (M.W.) of 600,000 g mol^{-1}. Chitosan is produced commercially by deacetylation of chitin, which is the structural element in the exoskeleton of crustaceans (such as crabs and shrimp) and cell walls of fungi. Chitosan

adopted in this research has a M.W. of 100,000-300,000 g mol^{-1}. Xanthan gum is an anionic polysaccharide, derived from the bacterial coat of Xanthomonas campestris, which usually used as rheology modifier and soil conditioner. The xanthan gum used in this research has a M.W. of 90,000-160,000 g mol^{-1}. All chemicals were purchased from Fisher Scientific, and were used as received.

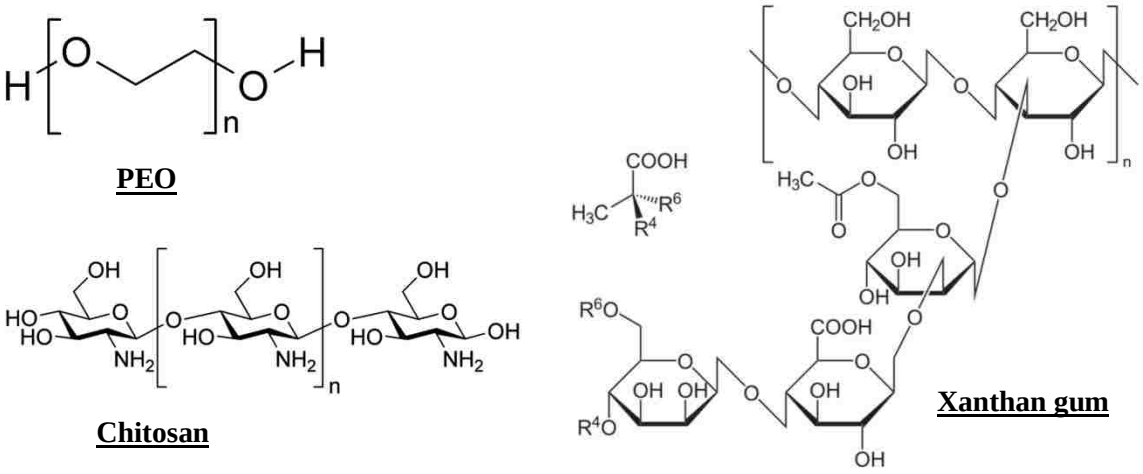

Figure 6-2 The chemical structures of PEO, Chitosan, and Xanthan gum.

6.2.2. Sample Preparation. All the specimens used in this study were obtained from slurry consolidation. The details of the sample preparation are in Kang et al. (2014), but the key information is presented here. Dry fly ash and kaolinite at fly ash weight ratios of 0, 30%, 60% and 100% were mixed and submerged into 1.0 mol/l NaCl solutions or 1 g/l polymer solutions (PEO, xanthan gum, or chitosan) with a solid to water ratio of approximately 0.2 (± 0.05). The resulting slurry was then gently stirred by hand for 30 minutes and then let stand for 24 hours for the completion of the hydration

process. The slurry was then translated into a sample preparation tube (45.7 cm × 11.5 cm in height × diameter) with double drainage system. Stepped axial consolidation loadings of 3.5, 7, 14, 28, 50, and 100 kPa, was applied to the slurry during which the settlement of the loading piston was monitored, and each step of loading was added until the end of primary consolidation was reached (judged by Taylor's method). After reaching 100 kPa vertical consolidation pressure, samples were unloaded with the unloading sequence of 100, 50, 28, 14, 7, and 3.5 kPa and then stored in moist curing room until testing. It is important to note that friction losses from loading piston were not measured in the slurry consolidometer and that the ultimate vertical consolidation load on the slurry was lower than the nominal vertical load 100 kPa.

6.2.3. Scanning Electron Microscopy Imaging. SEM test was performed on fly ash, kaolinite and organically modified kaolinite and fly ash-kaolinite samples with SEM S-4700 (Hitachi Inc.). Sample surfaces were coated with a conductivity material, gold, using a sputter-coater (Hitachi E 1030) so as to increase the surface electrical conductivity and ensure high quality images. For each sample, four to six images were taken and compared, and then a representative image was reported.

6.2.4. Consolidated Undrained (CU) Triaxial Compression Test. Isotopically consolidated undrained triaxial compression tests were carried out in a Humboldt triaxial testing system with normally consolidated samples and three effective consolidation pressures (Table 6-2). All the shear tests were strain-rate-controlled tests and were performed in accordance with ASTM D 4767-11.

The slurry consolidated specimens (11.5 cm diameter) were trimmed into four 3.6 cm (2.8 in) diameter by 7.2 cm (5.6 in) height cylindrical specimens for triaxial

compression tests. The specimens were saturated using back pressure until a *B* value of 0.95 or higher were reached. After saturation, the specimens were consolidated by different consolidation pressures, 103 kPa (15 psi), 207 kPa (30 psi), and 414 kPa (60 psi). The coefficient of consolidation, C_v, of kaolinite, fly ash-kaolinite mixtures, and organically modified fly ash-kaolinite mixtures was analyzed using the Taylor square-root-of-time method with double drainage.

A strain-rate of 0.0005 cm/min (0.0002 in/min) based on the lowest permeability samples (pure kaolinite) was used for applying the deviatoric stress. This strain rate was adopted for all the tests, therefore to avoid the strain-rate effects. Large shear strain was retained for each test so as to ensure all the specimens have reached the critical state. Because under small shear strain the macro-fabric is sheared to critical state, however, the micro-fabric of individual clay packets may not reach the critical state thus the initial fabric influence is still associated (Wheeler and Sivakumar 2000).

Corrections for cross-sectional area change, membrane stiffness, and friction between loading rod and bushing were accounted for in the calculation of applied stress. The corrected heights and diameters of the samples were used in the shearing test calculation by assuming the deformation of a "right" circular cylinder.

To prevent corrosion within the panel controls, the salt/organic solution was isolated from the de-aired water by P620000 bladder accumulators (Trautwein Soil Testing Equipment, Houston, Texas). Void ratios of the samples at the end of consolidation of each test were tabulated in Table 6-2.

Table 6-2 Physical and mechanical properties of tested samples

Test Sample	Liquid Limit	Void Ratio			Φ_{peak}	$\Phi_{residual}$
		104(kPa)	207(kPa)	414(kPa)		
Pure Kaolinite	54.8	1.238	1.133	1.021	-	20.3
1.0 mol/l NaCl Kaolinite	51.0	1.185	1.075	1.004	25.6	21.4
30 % Fly ash-Kaolinite	44.5	0.977	0.864	0.796	29.7	25.2
60 % Fly ash-Kaolinite	32.9	0.997	0.916	0.846	31.3	27.9
100 % Fly ash	N/A	1.072	1.043	1.031	31.3	30.0
1.0 g/l PEO+ 30 % Fly ash-Kaolinite	43.2	1.077	1.009	0.875	31.0	26.3
1.0 g/l Chitosan+ 30 % Fly ash-Kaolinite	44.3	1.015	0.925	0.844	29.4	25.3
1.0 g/l Xanthan Gum+ 30 % Fly ash-Kaolinite	50.7	1.232	1.139	1.007	28.2	22.6

The CU triaxial test results were presented in the $p'-q$ stress space, where q is the difference between effective major and minor principle stresses (Equation 6-1), and p' is one third of the summation of the three effective principle stress (Equation 6-2). M is called the friction parameter which is the slope of the critical state line in $p'-q$ space. The critical state is defined that "under sustained uniform shearing, the soil is continuously deforming at constant volume, constant normal effective stress, constant shearing stress, and constant velocity" (Schofield and Wroth 1968). The critical state lines in $p'-q-e$ space are defined by Equations 6-4 and 6-5, where e_{cs} is the void ratio, p'_{cs} is the mean effective stress, and q_{cs} is the deviator stress at critical state. The Γ_{cs} is the location of CSL in the compression plane and the λ_{cs} is the slope of the CSL in $v-\log p'$ plane.

$$q = (\sigma_1^{'} - \sigma_3^{'}) \quad \text{Equation 6-1}$$

$$p' = \frac{1}{3}(\sigma_1^{'} + 2\sigma_3^{'}) \quad \text{Equation 6-2}$$

$$M = \frac{6\sin\left(\phi_c^{'}\right)}{3 - \sin\left(\phi_c^{'}\right)} \quad \text{Equation 6-3}$$

$$q_{cs} = Mp_{cs}^{'} \quad \text{Equation 6-4}$$

$$v_{cs} = 1 + e_{cs} = \Gamma_{cs} - \lambda_{cs} \log p_{cs}^{'} \quad \text{Equation 6-5}$$

6.3. RESULTS

6.3.1. Microfabric and Particle Associations. SEM images suggested that the Georgia RP-2 kaolinite particles are primarily in platy shape (Figure 6-3a). On the contrary, fly ash particles are in spherical shape and varied in sizes under SEM (Figure 6-3b). The SEM image of 30% fly ash-kaolinite mixture is shown in Figure 6-3c, where ash particles were randomly distributed in the kaolinite (indicated by the circles).

Edge-to-Edge (EE) and Edge-to-Face (EF) particle associations were observed in both chitosan and xanthan gum treated kaolinite (Figures 6-3f and 6-3h). Face-to-Face (FF) aggregations were observed for the PEO treated kaolinite (Figure 6-3d), whose aggregate size was reached up to 2.585 μm (d_{50} of pure kaolinite is 0.3 μm).

For the organically modified 30% fly ash-kaolinite mixtures, similar microfabrics were observed where the fly ash particles are surrounded by the polymer induced highly compacted kaolinite aggregates (Figures 6-3e, 6-3g and 6-3i).

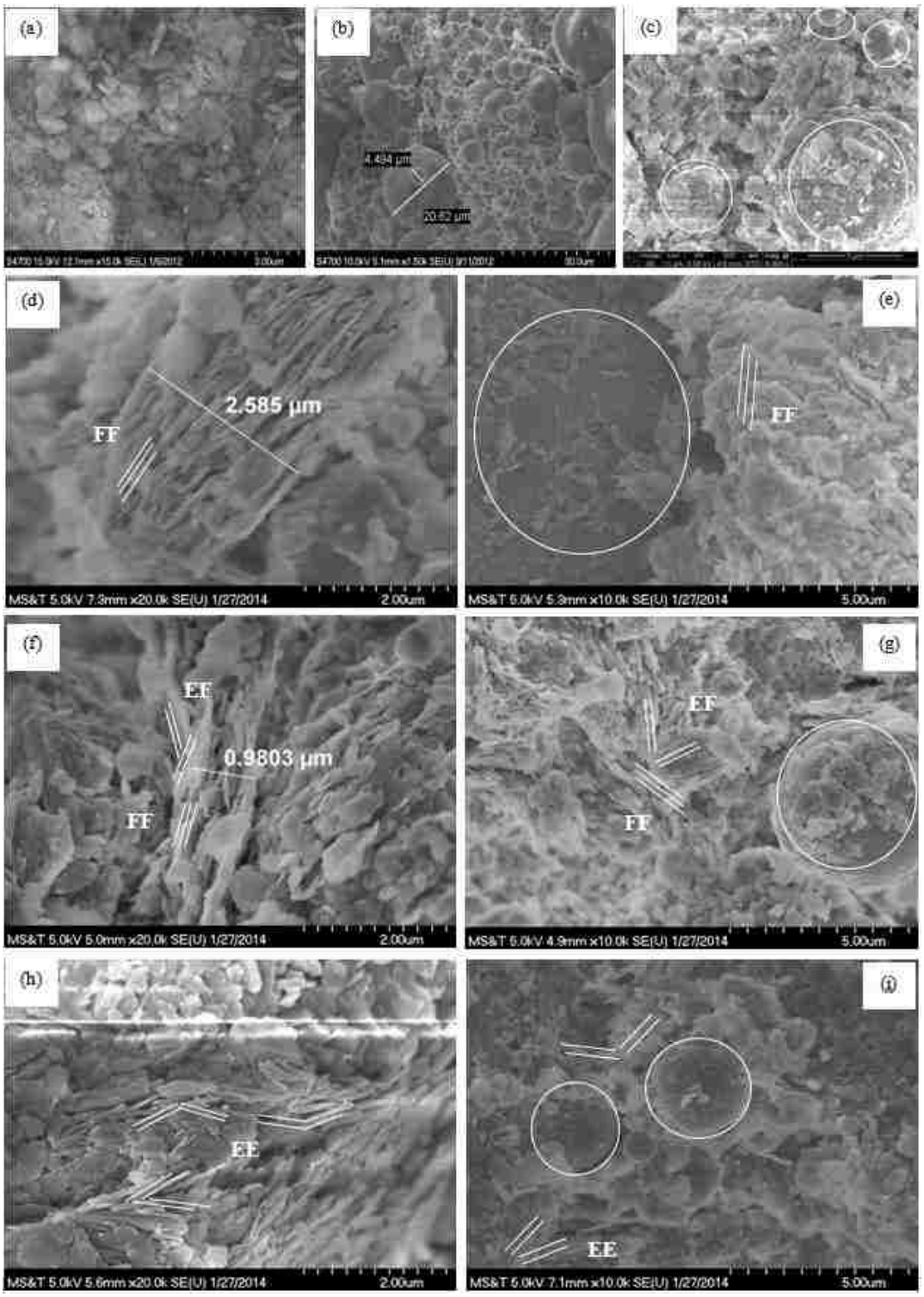

Figure 6-3 Scanning electron microscope images of: (a) Georgia RP-2 kaolinite particles, (b) fly ash particles, (c) 30 % fly ash-kaolinite mixtures, (d) Xanthan gum modified kaolinite, (e) PEO modified kaolinite, (f) Chitosan modified kaolinite, (g) PEO modified 30 % fly ash-kaolinite mixture, (h) Chitosan modified 30 % fly ash-kaolinite mixture, and (i) Xanthan gum modified 30 % fly ash-kaolinite mixture.

6.3.2. The Coefficient of Consolidation (C_v). The C_v was analyzed during the consolidation stage of the triaxial shear test at 414 kPa confining pressure. Pure kaolinite exhibited the lowest C_v, which is $4.45\times10^{-6}\,m^2/\min$. The C_v of kaolinite under 1.0 mol/l NaCl electrolyte solution was increased to $8.87\times10^{-6}\,m^2/\min$. The C_v of 30% and 60% fly ash-kaolinite mixtures, and pure fly ash are $2.07\times10^{-5}\,m^2/\min$, $7.12\times10^{-5}\,m^2/\min$, and $4.02\times10^{-3}\,m^2/\min$, respectively, indicating that the magnitude of C_v increased as the fly ash content increased. PEO and Chitosan resulted in higher values of the C_v (the C_v of PEO modified mixture is $8.22\times10^{-5}\,m^2/\min$, and the C_v of chitosan modified mixture is $2.38\times10^{-5}\,m^2/\min$), while xanthan gum relatively decreased the C_v of the 30% fly ash-kaolinite mixtures ($C_v = 1.35\times10^{-5}\,m^2/\min$).

Increases in the magnitude of C_v may indicate increased degree of flocculation within the organically modified soil (PEO and chitosan), which has been demonstrated to increase as the total organic content increased (Bate et al. 2014). The decrease in the magnitude of the C_v is attributed to the deflocculated and dispersed fabric that prohibited the flow. In addition, due to the pseudoplastic nature of xanthan gum, the pore fluid viscosity is increased, which decreases the hydraulic conductivity (polymer induced pore clogging), and in turn decreases the magnitude of the C_v (Bouazza et al. 2009; Martin et al. 1996).

6.3.3. Stress-Strain Responses. Contractive behaviors were observed for NC kaolinite samples in CU triaxial compression tests, where positive pore-water pressures were generated and the shear stress monotonically increased to a plateau value (Figure 6-4). All three NC kaolinite specimens bulged as the shearing taking place and no failure plane was observed at the end of shearing. The normally consolidated kaolinite under 1.0

mol/l NaCl electrolyte solution, however, exhibited peak shear stress point/pore-water pressure point (post peak strain-softening) with positive pore-water pressure generation (Figure 6-4). The post peak strain-softening behavior was due to a well-developed failure plane during shearing.

Post peak strain-softening behaviors were also observed for the 30% fly ash-kaolinite mixtures (Figure 6-5). The normally consolidated fly ash samples showed typical "overly consolidated" behavior (dilation) as those reported by Schofield and Wroth (1968), with the shear stress first mobilized to its peak and then yielded to the critical-state as shearing taking place (Figure 6-5d). Positive pore-water pressures were generated initially and then decreased to negative values. In general, the undrained shear strength of fly ash is much higher than that of the kaolinite and fly ash-kaolinite mixtures due to the dilation.

The PEO, chitosan and xanthan gum modified 30% fly ash-kaolinite mixtures tested in consolidated undrained triaxial compression tests also demonstrated peak shear strength and positive pore-water pressure generation, as exhibited by the stress-strain behaviors of PEO modified 30% fly ash-kaolinite mixtures (Figure 6-6a). Stress-strain behaviors of other tested organically modified soils were similar (data not shown). All the samples showed a peak shear stress point, after that yielded to the critical state as shearing taking place, which is similarly to the behaviors observed from the salt treated kaolinite (Figure 6-4). There is no dilation tendency observed due to the positive pore-water pressure generation (Figure 6-6b). It was noted that the peak shear strength was mobilized at smaller strains when the effective confining pressure is low (indicated by the circle in Figure 6-6a).

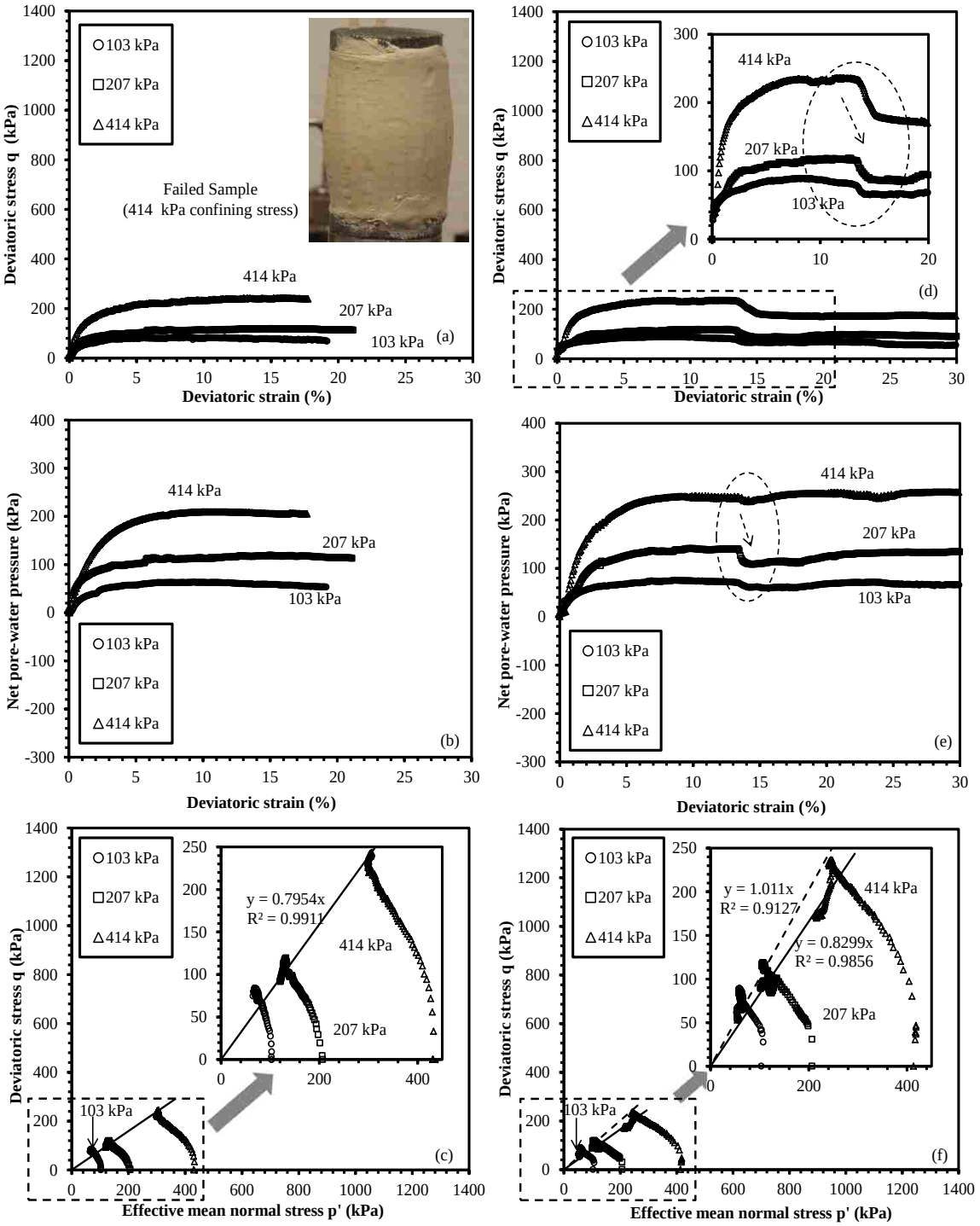

Figure 6-4 Consolidated undrained triaxial compression strength test results of pure kaolinite (a) stress-strain diagram; (b) pore-water pressure diagram; (c) $p' - q$ diagram; and 1.0 mol/l NaCl treated kaolinite: (d) stress-strain diagram; (e) pore-water pressure diagram; (f) $p' - q$ diagram.

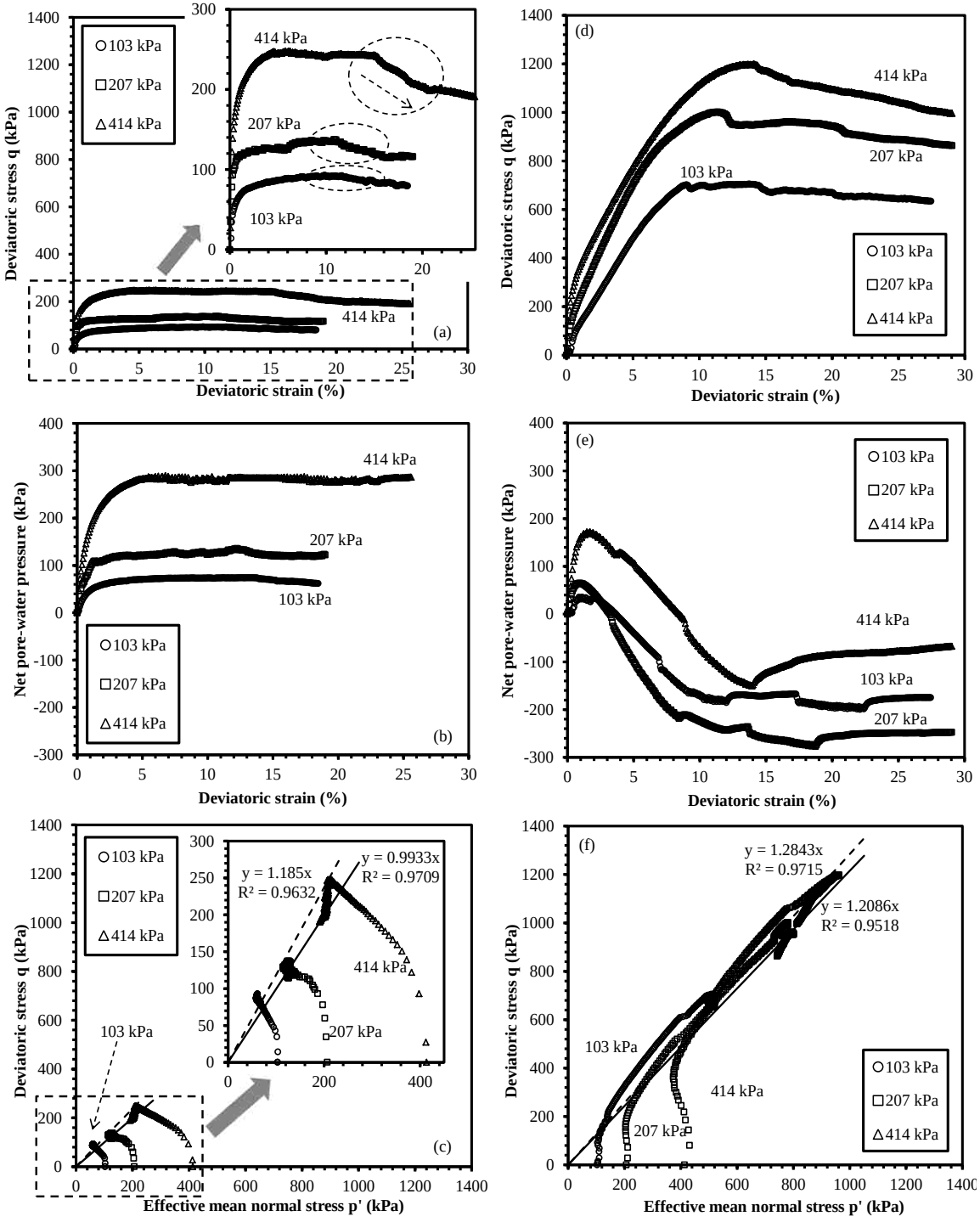

Figure 6-5 Consolidated undrained triaxial compression strength test results of 30 % fly ash-kaolinite mixture (a) stress-strain diagram; (b) pore-water pressure diagram; (c) $p' - q$ diagram; and 100 % fly ash samples: (d) stress-strain diagram; (e) pore-water pressure diagram; (f) $p' - q$ diagram.

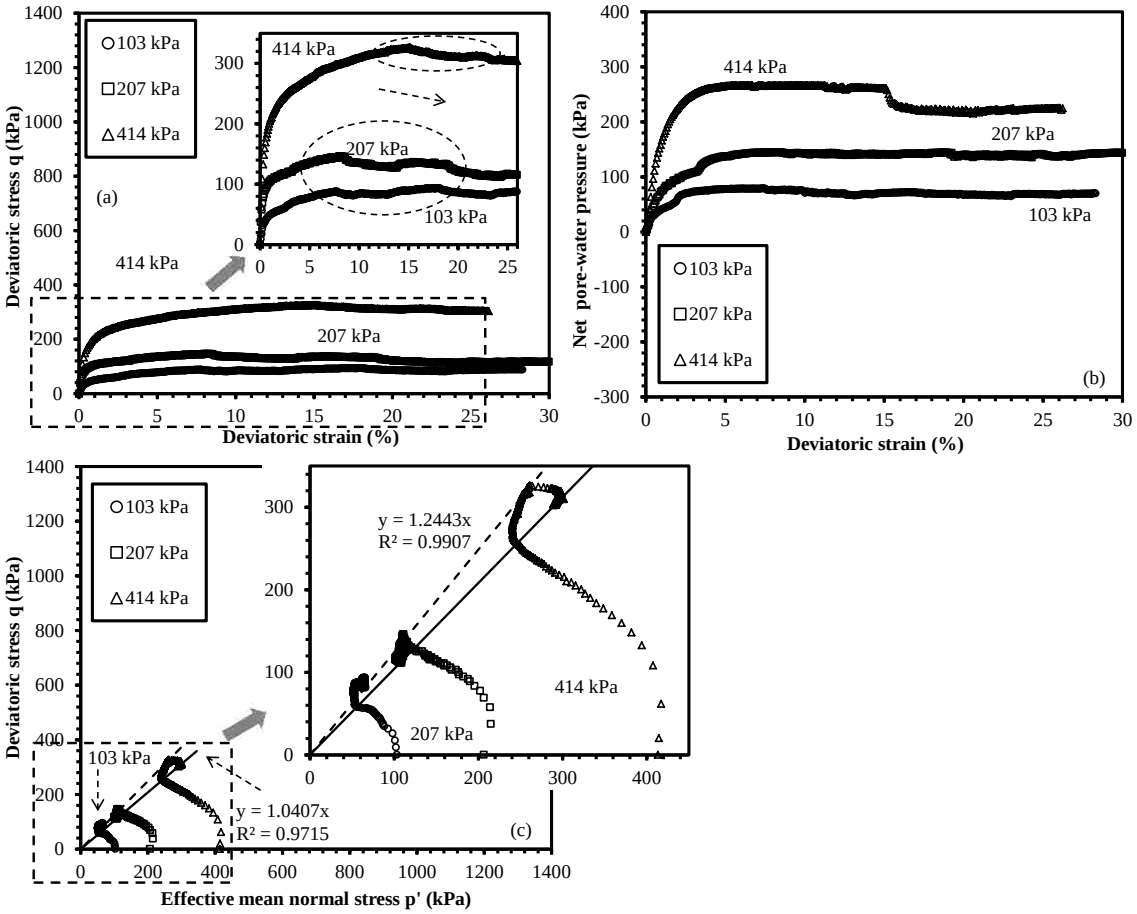

Figure 6-6 Consolidated undrained triaxial compression strength test results of PEO modified 30 % fly ash-kaolinite mixtures (a) stress-strain diagram; (b) pore-water pressure diagram; (c) $p' - q$ diagram.

The NCLs were plotted against the effective mean normal stress at the end of isotropic consolidation and the CSLs were plotted by using the mean normal effective stress values at the critical state (Roscoe and Wroth 1958; Schofield and Wroth 1968) (see Figures 6-7a, 6-7b, and 6-7c). Linear regressions were carried out based on the Equations 6-4 and 6-5 and the locations of NCLs and CSLs (Γ_{nc} and Γ_{cs}) and the slopes of NCLs and CSLs (λ_{nc} and λ_{cs}) in $v - \log p'$ plane, and the slope of the critical state

failure envelope, M, were determined and tabulated in Table 6-3. Based on the test results, a few observations were draw: (1) The NCLs were roughly parallel with the CSLs for all the soils, although deviation was noted in some instances (100 % fly ash sample, and xanthan gum modified fly ash-kaolinite sample) as higher pressures were reached. (2) Salt could effectively lower the position of the NCL and CSL of kaolinite; however the slope of NCL and CSL remain unchanged (Figure 6-7a). (3) As the fly ash content increased, the slope of the NCL in $v - \log p'$ plane (λ_{nc}) decreased from 0.36 (0 % fly ash) to 0.07 (100 % fly ash). Similarly trend was observed for the λ_{cs} (Figure 6-7b). The location of the CSL in the compression plane also moved downward (from 1.97 to 1.20), however, the slope of the failure envelope M increased (0.80 to 1.21). (4) Chitosan and PEO were found to decrease the λ_{cs}, and increased the values of Γ_{nc} and Γ_{cs}. On the contrary, the slope of the NCL and CSL in $v - \log p'$ plane was increased and the locations (Γ_{nc} and Γ_{cs}) moved up due to the addition of xanthan gum (Figure 6-7c, Table 6-3).

In $p' - q$ space, the peak and critical-state friction angles were calculated by regression analysis from stress-strain curves at three different confining pressures (Figures 6-4, 6-5, and 6-6). The coefficient of determination ranged from 0.9127 to 0.9907 for peak friction angels and from 0.9518 to 0.9955 for critical-state friction angles, indicating good correlations. The effective critical-state friction angle of kaolinite in deionized water and in 1.0 mol/l NaCl solution are 20.3^0 and 21.4°, respectively. Peak friction angle ($\phi_p' = 25.6^0$) was induced for the kaolinite in 1.0 mol/l NaCl solution (Figure 6-4). PEO and Chitosan were found to slightly increase the ϕ_c', however, xanthan

gum relatively decreased the $\phi_c^{'}$ of kaolinite (as indicated by the "difference" of $\phi_c^{'}$ between polymer modified and unmodified kaolinite in Figure 6-8b).

Table 6-3 Parameters of the NCL and CSL

Test Sample	NC State		Critical state		M
	λ_{nc}	Γ_{nc}	λ_{cs}	Γ_{cs}	
Pure kaolinite	0.36	1.97	0.34	1.86	0.80
1.0 mol/l NaCl kaolinite	0.30	1.78	0.31	1.71	0.83
30 % Fly ash+70 % kaolinite	0.31	1.58	0.33	1.55	0.99
60 % Fly ash+40 % kaolinite	0.25	1.50	0.31	1.56	1.11
100 % Fly ash	0.07	1.21	0.12	1.36	1.21
1.0 g/l PEO+30 % Fly ash-kaolinite	0.35	1.80	0.33	1.66	1.04
1.0 g/l Chitosan+30 % Fly ash-kaolinite	0.28	1.59	0.31	1.58	0.99
1.0 g/l Xanthan gum+30 % Fly ash-kaolinite	0.37	1.99	0.66	2.49	0.88

For the fly ash-kaolinite mixtures, both the peak and critical-state friction angles increased as the fly ash content increased (Figure 6-8a). For the organically modified 30% fly ash-kaolinite mixtures, the $\phi_c^{'}$ of PEO modified mixture increased from 25.2^0 to 26.7^0, the $\phi_c^{'}$ of Chitosan treated mixture remained almost unchanged (slightly increased from 25.2^0 to 25.3^0), however, the $\phi_c^{'}$ decreased from 25.2^0 to 22.6^0 by mixing of the xanthan gum. The effect of polymers on the $\phi_c^{'}$ was found to follow the order of PEO>chitosan>xanthan gum.

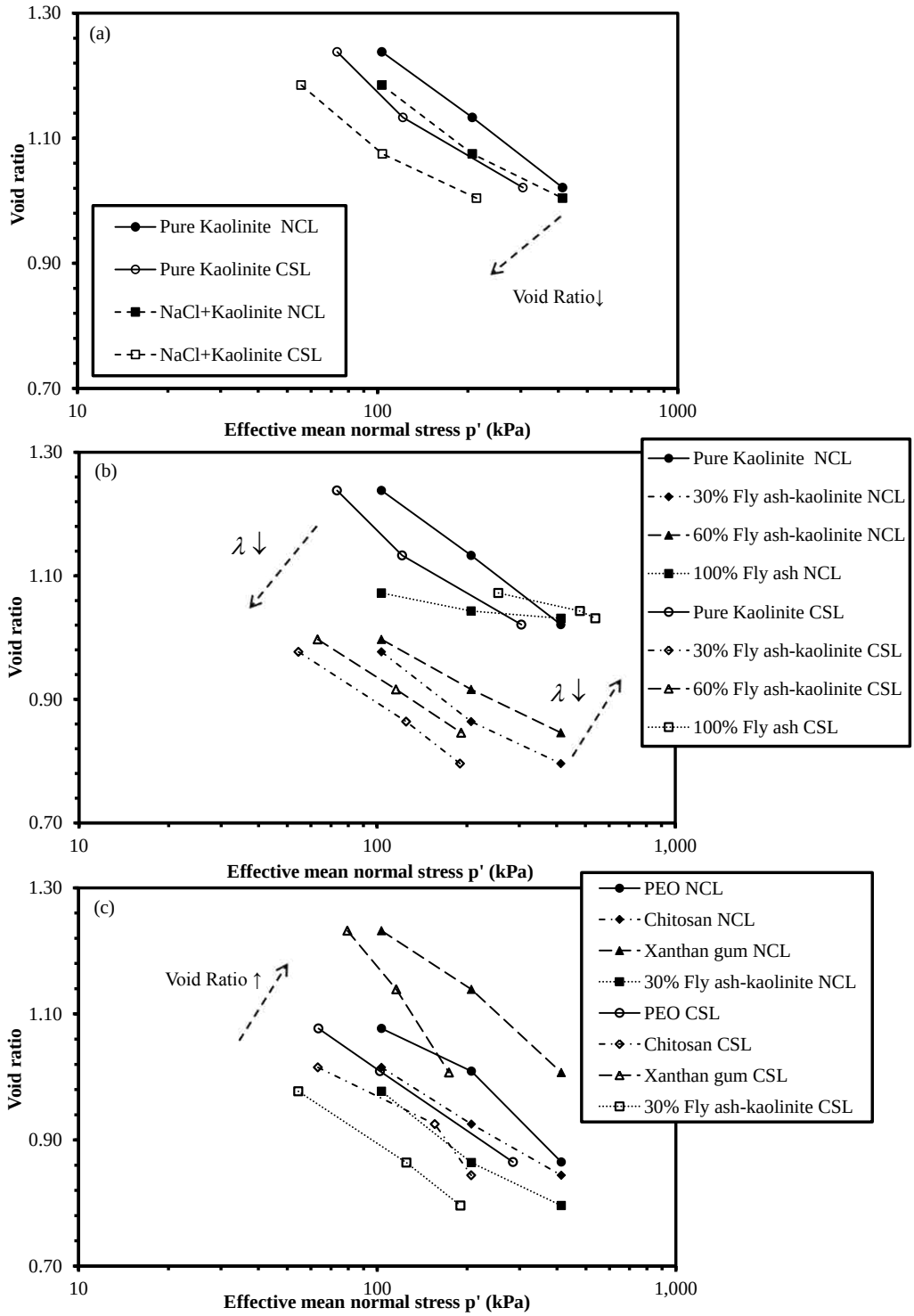

Figure 6-7 Normal consolidated lines (NCL) and critical state lines (CSL) for test samples: (a) pure kaolinite and salt treated kaolinite; (b) fly ash kaolinite mixtures at different fly ash content; (c) organically modified fly ash kaolinite mixtures at 30% fly ash content.

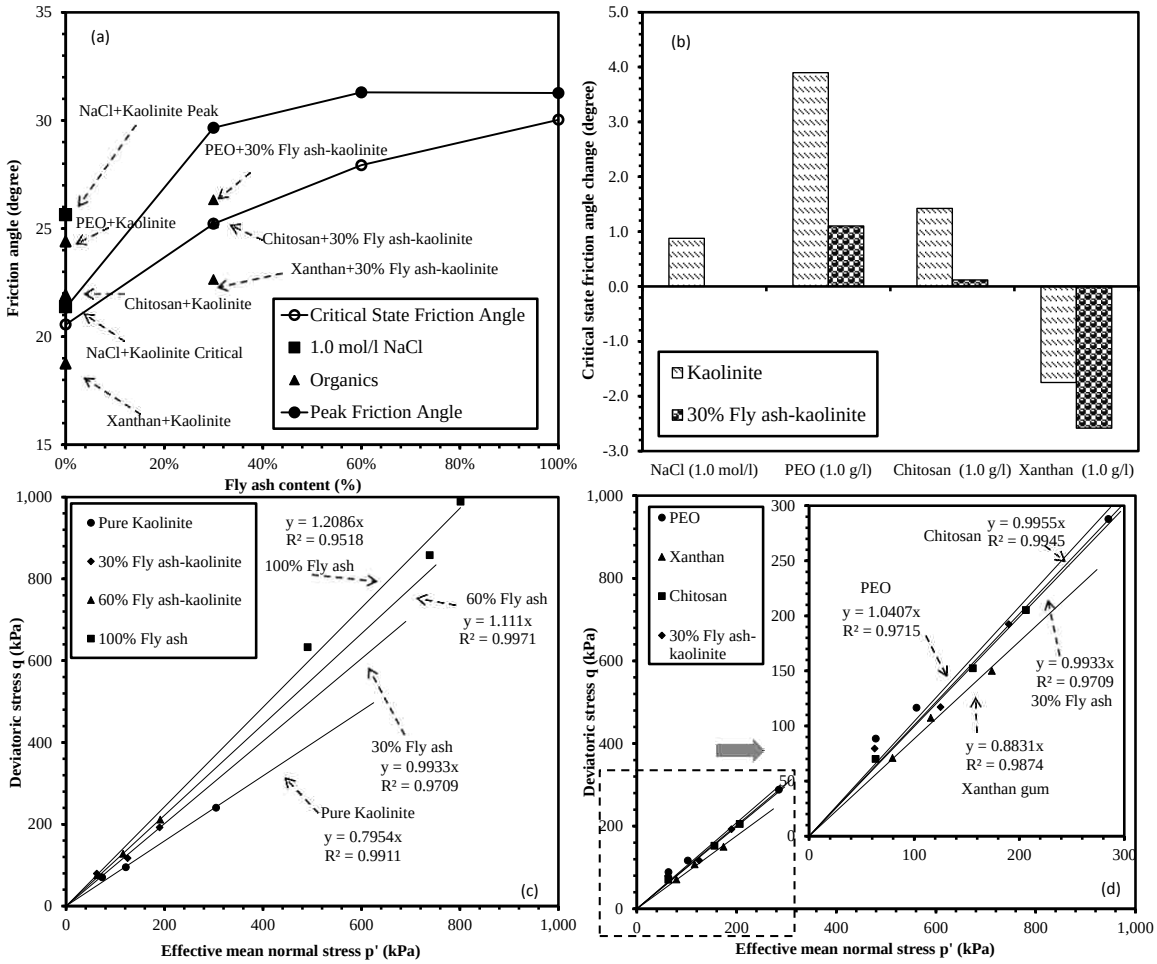

Figure 6-8 (a) Peak and critical-state friction angles for tested specimens as a function of the fly ash content: (b) critical-state friction angle change induced by different salt and organic polymers for both kaolinite and 30% fly ash-kaolinite mixtures; (c) critical-state of fly ash-kaolinite mixtures in p'-q space; (d) deviatoric stress as a function of effective mean normal stress of fly ash-kaolinite mixture modified by different polymers.

6.4. DISCUSSIONS

6.4.1. Effect of Salt on the Stress-Strain Behaviors of Kaolinite. All three NC kaolinite samples treated by 1.0 mol/l salt solution exhibited post peak strain-softening behaviors (Figure 6-4a). This is attributed to the aggregated microfabric (FF) that induced by the high salinity condition (Mitchell and Soga 2005; Moore and Mitchell 1974). In

addition, high salinity condition shrunk the thickness of electrical diffuse double layer, induced aggregation to kaolinite, and decreased water content, which in turn reduced the void ratio (Table 6-2). The critical-state friction angle of kaolinite was increased by the addition of salt, which is attributed to the following three mechanisms. (1) The increase of the interparticle attractive force. Salt could compress EDL and reduce the EDL repulsion force, which lead to the van der Waals attraction force becomes the dominant interparticle force (Anandarajah and Zhao 2000; Moore and Mitchell 1974; Sachan and Penumadu 2007; Yong and Warith 1989;). (2) The alteration of the kaolinite basal spacing by salt (Mitchell and Soga 2005). The decrease of basal spacing will lead to an increase of the frictional resistance during basal plane slippage (Mitchell and Soga 2005). (3) Salt induced "larger" kaolinite aggregates (Figure 6-3) that enhanced the frictional resistance during shearing (Kang et al. 2013). Furthermore, it is documented that 1.0 mol/l NaCl could also increase the critical-state friction angle of bentonite clay by 3^0 (Di Maio and Fenelli 1994).

6.4.2. Effect of Fly Ash Content on the Stress - Strain Behaviors. Normally consolidated fly ash-kaolinite mixtures exhibited post-peak strain softening behavior during shearing (Figure 6-5a), which is attributed to the initially flocculated microfabric (EE/EF) induced by the high pore fluid ionic strength. For example, the hydration of 30% fly ash in the mixture could increase the pore fluid ionic strength to 936 $\mu S/cm$ (equivalent to 0.01 mol/l salt solution), which essentially induced flocculation (EF/EE) to kaolinite ("fabric map"), therefore, all specimens exhibited post-peak strain-softening behavior during shearing (Palomino and Santamarina 2005).

The NC fly ash samples, however, exhibited dilative behaviors during shearing (Figure 6-5d) which is attributed to the coarse fly ash particles (like sand) and high relative density (78.8%). The fly ash used in this study is classified as "sandy silt" (USCS) which has approximately 25% particles in the range of fine sand (62.5-125 μm) and 75% particles in the range of silt (4-62.5 μm) with little plasticity. The relative density of the slurry consolidated fly ash sample is 78.8% ($e_{\max} = 1.391$ and $e_{\min} = 0.984$) (ASTM D 4253 and D 2454), which falls into the category of dense sand (I_D = 65%-85%) (Craig 1997). Therefore, it exhibited dilative behaviors during shearing. Furthermore, dilative trends were observed in Dingrando et al. (2013), whose fly ash contains 22% particles in the range of fine sand, and their NC fly ash samples were also prepared by slurry consolidation. Kim et al. (2005) and Rivard-Lentz et al. (1997) conducted CU test on compacted fly ash samples (I_d =75% and 95%) which also exhibited dilative behaviors.

As the fly ash content increased, the slope of the NCLs and CSLs decreased (Table 6-3), indicating the compressibility of the fly ash-kaolinite mixtures decreased. Saturated kaolinite particles are more plastic because they have thick EDL and large interparticle repulsive force (Santamarina et al. 2001); however, spherical fly ash particles have thin EDL (little interparticle repulsive force). The large repulsion force generated from thick EDL of kaolinite causes greater interparticle void space, which leads to the high compressibility of kaolinite. As the fly ash content increased, it not only gradually replaces kaolinite, but also compresses the EDL of kaolinite during hydration, thus the compressibility decreased.

The peak and critical-state friction angle changes could be understood by the proposed concept of "threshold fly ash content" (Kang 2015), which is defined as the weight of fly ash over the total weight of the fly ash-kaolinite mixture when kaolinite fully fills the interparticle voids among fly ash grains. Essentially, it is related to the onset of continuous fly ash particle contacts throughout the sample, where the external forces were mainly taken by the chains of fly ash particle contacts. In this study, the threshold fly ash content of the fly ash-kaolinite mixtures constructed by slurry consolidation is found between 53.1% and 71% (see appendix), which corresponding to the observed noticeable changes of both the peak and critical-state friction angles at approximately 60% (Figure 6-8a). When the fly ash content was higher than the threshold fly ash content (> 60%, Figure 6-8a), fly ash particles dominated the contacts, thus both the peak and critical-state friction angles stayed constant. When the fly ash content went below the threshold fly ash content (< 60%, Figure 6-8a), kaolinite-to-kaolinite contact dominated the behavior. As a result, both the peak and critical-state friction angles decreased as the kaolinite content increased (Figure 6-8a). Similarly results were observed by Kim et al. (2005) who investigated the peak and critical-state friction angles of a binary soil (SM mixed with ML). When the SM content increased from 50% to 100% (where bottom ash was the dominant), the peak friction angle was found to be almost constant (increased by $1^0 - 2^0$) and the critical-state friction angle slightly increased (by 3^0). Rivard-Lentz et al. (1997) reported that the undrained shear strength kept almost constant when bottom ash mixed with bentonite up to 20%. Their findings all indicate that when the coarse-grained soil becomes the dominant component in a mixture (the contacts are formed

through coarse grains, fines only fill in the interparticle voids), the strength of the binary soil will be governed by the continuous contacts of the coarse particles.

6.4.3. Effect of Polymers on the Particle Associations and Microfabric. Due to the effect of polymer bridging (Mpofu et al. 2004), kaolinite particles were agglomerated together by PEO (Figure 6-3d). The typical measured aggregate size reached 2.585 μm , which is eight times larger than the typical kaolinite aggregates under SEM (0.3 μm). PEO could also induce a contraction of the clay interlayer *d* spacing (Swenson et al. 1998). Thus it condensed the soil and induced densely packed kaolinite aggregates (FF, Figures 6-3d, and 6-3g). Although chitosan could induce densely packed kaolinite aggregates (FF) through polymer bridging, its average size (0.980 μm) was found to be smaller than that of the PEO modified kaolinite (2.585 μm) (Figure 6-3e), which might be attributed to the following two reasons. Positively charged chitosan will firstly interact with negatively charged kaolinite through Coulombian attraction (charge neutralization). However, charge neutralization would not bind kaolinite particles together and therefore would not induce large compacted aggregates (Chen and Chung 2011; Huang and Chen 1996; Parazak et al. 1988). Besides, charge neutralization process might reduce the number of available polymers that participate in the secondary interaction - polymer bridging, such as hydrophobic interactions and hydrogen bonds (Kim and Yang 2012; Zhang et al. 2013). As a result, given the same dosage, the polymer bridging effect of Chitosan is weaker than PEO. Due to the strong electrostatic repulsion forces among the negatively changed xanthan gum, fly ash and kaolinite, xanthan gum chains are extended and repelled out, which lead to the formation of a loose-open microfabric (EF, EE) (Benchabane and Bekkour 2006; Labille et al. 2005; Tan et al. 2014; Zhang et al. 2013).

In addition, the anionic side chains of xanthan gum are close to each other (Figure 6-2), inducing high charge density, strong electrostatic repulsion, and thus a rigid double-helix conformation (Lp=120 nm), which compromise the bridging effect (Labille et al. 2005; Lafuma et al. 1988) and contribute to the formation of EE and EF microfabric (Figures 6-3f, and 6-3i).

6.4.4. Effect of Polymers on the Stress – Strain Behaviors. The observed post peak strain-softening behavior of polymer modified fly ash-kaolinite mixtures (i.e., PEO) is primarily attributed to the "damage" of polymer induced flocculated and aggregated microfabrics during shearing. In addition, van der Waals attraction and polymer bridging could develop interparticle cohesion between soil particles (Cole. et al. 2012), thus induces apparent overconsolidation to the normally consolidated soils which exhibited post peak strain-softening behaviors during shearing (Figure 6-6a, Nugent et al. 2010; Mitchell and Soga 2005). Although post peak strain-softening was observed, the organically modified fly ash-kaolinite mixtures did not show any trend of dilation due to the positive net pore-water pressure generation during shearing (Figure 6-6b). The positive net pore-water pressure generation is attributed to the entanglement and cross-linking of polymer strands in the clay-polymer interwoven network, which developed open interparticle pores (Kim and Palomino 2009).

PEO was found to slightly increase the critical-state friction angle of the 30% fly ash-kaolinite mixtures (Figures 6-8a and 6-8d), which is attributed to the following two reasons. (1) Formation of the clay-polymer-fly ash interwoven network by "polymer bridging". The entanglement of the adsorbed PEO chains would act as "adhesive bonding" between kaolinite particles, which contribute to the increase of interparticle

attractive force (Gregory 1985; Mpofu et al. 2004; Nugent et al. 2010; Podsiadlo et al. 2007; Swenson et al. 1998; Theng 1982). As a result, the shear resistance increased. (2) Increased aggregate sizes by polymer bridging (Figure 6-3d). The "particles" become coarser in the mixture, thus the aggregate-to-aggregate friction resistances increase (Anandarajah et al. 1996; Kuganenthira et al. 1996). Similar to PEO, the positively charged chitosan could also bridge kaolinite particles while the critical-state friction angle only increased slightly (Figure 6-8d). On the other hand, the repulsion force between negatively charged xanthan gum chains, fly ash, and kaolinite particles leaded to a loose-open microfabric, where the particles were loosely associated and dispersed away from each other (Atesok et al. 1988; Theng 1982; Zhang et al. 2013). In addition, the repulsion force between xanthan gum chains and kaolinite particles reduces the interparticle attractive force, which is equivalent to a reduction of the "effective stress" (Mitchell and Soga 2005). Therefore, the critical state friction angle of xanthan gum modified mixture slightly decreased (Figure 6-8d).

The cross-linking and entanglement of polymer chains leaded to a highly interlinked clay-polymer interwoven network (Nugent et al. 2010; Gregory 1985; Podsiadlo et al. 2007, Theng 1982). Interparticle open pores were formed in the network due to higher degree of flocculation and aggregation where more water is trapped in. In addition, the polymers all have hydrophilic function groups which provide additional adsorption sites for water molecules. As a result, the void ratio and liquid limit both increased slightly at macro scale (Table 6-2). For example, the mixing of xanthan gum relatively increased the water content and raised up the positions of CSL and NCL of the fly ash-kaolinite mixtures. The measurement of the zeta potential of Xanthan gum treated

fly ash soil mixtures (Kang et al. 2013) indicated that high interparticle repulsive forces and greater thickness of the EDL have been induced. Therefore the soil particles were largely dispersed by each other which would allow greater interparticle void space and result in higher initial void ratio.

6.5. CONCLUSIONS

The stress-strain behaviors of fly ash-kaolinite mixtures and organically modified fly ash-kaolinite mixtures were investigated in this study by conducting consolidated undrained triaxial compression tests. The following results were concluded:

(1) Due to the effect of polymer bridging, the addition of PEO and chitosan induced flocculation (EF) and aggregation (FF) to the soil which yielded larger and densely packed kaolinite aggregates. Due to the strong interparticle repulsion forces, however, loose-open microfabric (EF, EE) was observed for xanthan gum treated soil where the particles were dispersed away from each other.

(2) The C_v of kaolinite was found to increase as the fly ash content increased. PEO and Chitosan resulted in higher values of the C_v while xanthan gum relatively decreased the C_v of 30% fly ash-kaolinite mixture.

(3) High ionic strength could induce flocculated/aggregated microfabric, yield "larger" and densely packed kaolinite aggregates, and increase the interparticle attractive force. Therefore, the addition of salt to kaolinite has induced post-peak strain softening behavior during shearing and increased the critical-state friction angle. In addition, flocculation and aggregation would decrease the specific area and increase the density of the kaolinite, which leaded to a reduction of the water content and void ratio at macroscale, thus lowered the position of the CSL (NCL).

(4) Before threshold fly ash content (～60%), both the peak and critical-state friction angles increased as fly ash content increased. When the fly ash content goes beyond the threshold fly ash content, continuous fly ash particle contacts might generate throughout the sample where the external forces are mainly taken by the chains of fly ash particle contacts. As a result, both the peak and critical-state friction angles stayed constant/or increased slightly. In addition, more kaolinite is replaced by increasing of fly ash content, which not only increases the ionic strength (shrinks the kaolinite's EDL), but also enhances the fly ash to fly ash particle contacts, thus lead to lower compressibility and lower positions of the NCLs and CSLs.

(5) Polymer modified fly ash-kaolinite mixtures exhibited post peak strain-softening behavior during shearing, which might be attributed to the "damage" of clay-polymer interwoven network and the "apparent" overconsolidation induced by the polymer "adhesive bonding". PEO mediated large kaolinite aggregates and leaded to the formation of the kaolinite-polymer interwoven network, thus the critical-state friction angle was increased. The addition of xanthan gum, however, deflocculated the microfabric which leaded to lower resistance to the external stress, thus the critical-state friction angle was decreased.

7. CONCLUSIONS AND RECOMMENDATIONS

7.1. INTRODUCTION

This study investigated the mechanical characteristics of organically modified fly ash-kaolinite mixtures. Organic agents, such as biopolymers (Chitosan and Xanthan gum) and synthetic polymers (Polyethylene Oxide) were utilized to improve the engineering properties of the fly ash-kaolinite mixtures so as to increase the reuse volume of class F fly ash in geotechnical engineering. The effects of fly ash and polymers on the microstructure and geotechnical properties, such as strength, stiffness, stiffness anisotropy, and compressibility of the organically modified soils were investigated by a series of laboratory tests which include scanning electron microcopy test, Atterberg limits test, conduction test, proctor compaction test, consolidation test, bender element test, and triaxial compression test. Based on the laboratory investigations, a few conclusions have been drawn which are presented in the following section.

7.2. CONCLUSIONS

The laboratory investigation showed that organic polymers were able to modify the microfabrics and particle associations of the kaolinite and fly ash-kaolinite mixtures. Due to the change of microfabric and pore fluid chemistry, the geotechnical properties of organically modified soils were found largely dependent on the polymers. The addition of fly ash could reduce the liquid limit and plastic limit of the kaolinite, which in turn decreased the PI. Organic agents, such as xanthan gum was found to increase the liquid limit of the kaolinite, however, the liquid limit was quite constant for PEO and Chitosan modified soils. The maximum dry unit weight was found to increase and the optimum

water content was found to decrease by the addition of fly ash. The addition of organic polymers resulted in a slightly increase of the maximum dry unit weight, however, the dry unit weight decreased as the organic content increased further. The thermal conductivity of fly ash-kaolinite mixtures was found relatively low compared with pure kaolinite, and an increase of the organic agents could cause the thermal conductivity to decrease.

A new floating wall-type consolidometer bender element testing system was developed to study stiffness anisotropy of clays at applied vertical stress up to 800 kPa. The floating wall design eliminated the detrimental bending moment that acted upon the benders due to soil settlement, which greatly improved signal quality and bender reuse. In addition, the water chamber maintains saturation and pH, salt concentration of bulk fluid. Floating wall-soil interface resistance was evaluated with both pulling tests and analytical equations, and was quantified with cohesion and friction components. Analytical equations were then derived to calculate the wall resistance-corrected vertical effective stress. The shear wave velocity of kaolinite was measured via the bender element test which indicated that V_s increased with stress, density, and concentration. The hierarchy of V_s in three orthogonal directions (i.e., hh > hv > vh) agreed with results in the literature. It was also illustrated that V_s anisotropy increased with applied stress and decreased during unloading. Several advantages of the newly developed device in measuring stiffness anisotropy over a triaxial test setup were discussed. The benefit including easiness of installing horizontal bender elements, concurrent measurement of V_s in three orthogonal directions in one sample (compared to single pair bender element setup), the flexible geometry in design that can improve the signal quality by limiting side-reflected P-waves

and the near field effects (compared to three pairs BE setup), and the reduction of directly transmitting P-waves (compared to conventional setup).

The shear wave velocity and its anisotropy of organically modified fly ash-kaolinite mixtures were investigated by using the novel designed floating wall consolidometer type bender element testing system. The compressibility and swelling potential decreased as the fly ash content increased. PEO and chitosan could reduce the compressibility and swelling potential; however, xanthan gum relatively increased the compressibility and swelling potential of the organically modified fly ash-kaolinite mixtures. As the fly ash content increased, the magnitude of V_s in three orthogonal directions increased, however, the V_s anisotropy decreased. The increase of V_s is attributed to the increase of the number of fly ash contacts in the fly ash-kaolinite mixtures (due to the replacement of the kaolinite by fly ash). The decrease of the V_s anisotropy is due to the fly ash particle's spherical shape which has little stress induced fabric anisotropy. When the fly ash content is less than the $F_{th}(\%)$, the fly ash-kaolinite mixture's fabric anisotropy was found to increase as kaolinite content increased. On the other hand, when the fly ash content is higher than the $F_{th}(\%)$, the V_s anisotropy almost vanished due to the continuous fly ash-to-fly ash contacts. PEO and chitosan were found to increase the V_s of the fly ash-kaolinite mixtures. The reasons are attributed to the increased aggregate sizes by "polymer bridging" and the formation of the rigid clay-polymer interwoven network. The xanthan gum, however, was found to decrease the V_s which could be attributed to the development of deflocculated and dispersed microfabrics. As loading increased, the V_s anisotropy of the organically modified soil also increased which is comparable to the inorganic soils. However, the decrease of the

$V_{s\text{-}hh}/V_{s-vh}$ and $V_{s\text{-}hv}/V_{s-vh}$ of the organically modified fly ash-kaolinite mixtures under the same stress conditions indicating that the organically modified soils have less V_s anisotropy and are stiffer both horizontally and vertically. The major reasons are attributed to the polymer induced larger aggregates which reduced the degree of fabric anisotropy and stress anisotropy inside the specimen. In addition, the cross anisotropy assumption is found to be valid when fly ash content is higher than F_{th}, while it is invalid as fly ash content is lower than the F_{th}.

Regarding to the large-strain strength, the mechanical characteristics of fly ash-kaolinite mixtures and organically modified fly ash-kaolinite mixtures were investigated by conducting consolidated undrained triaxial compression tests. The physicochemical conditions (i.e., the pore fluid chemistry) were found to influence the stress-strain behaviors, the positions of CSL, and the shear strength. The observed post-peak strain softening behavior of salt treated NC kaolinite could be attributed to the damage of initial flocculated microfabric during shearing. In addition, the salt could also increase the critical-state friction angle of kaolinite. As fly ash content increased, the undrained shear strength and friction angles (both peak and residual) improved gradually. The fly ash not only chemically changes the pore fluid chemistry but also mechanically improves the contacts and frictional resistance. In addition, the positions of NCLs and CSLs have been lowered by adding fly ash. PEO was found to effectively increase the critical-state friction angle; however, xanthan gum slightly decreased the critical-state friction angle. The flocculation and polymer entanglement (clay-polymer interwoven network) could contribute to the increase of shear resistance (PEO and Chitosan), however, the

deflocculated microfabric (xanthan gum modified soil) which has lower resistance to the external stress would decrease critical-state friction angle.

7.3. RECOMMENDATIONS

This work investigated the mechanical responses of organically modified fly ash-kaolinite mixtures and provides insight and knowledge to explain the observed behaviors of the engineering properties of the polymer modified soils. It is recommended that, in the future, the following areas need to be further studied.

1. Investigate the microstructure and different functional groups of organic polymers on the efficiency of adsorption process on clay surface. Carry out kinetics study on the clay-polymer suspensions, including the adsorption and de-adsorption kinetics of polymers on the clay surface and the subsequent interaction between organic cations and inorganic cations on clay surface.
2. Numerical simulation on the effect of polymers on the shear strength behavior using molecular dynamics or programs at the clay particle scale level.
3. Test the durability of polymer modified fly ash-kaolinite mixtures under multiple impacts and harsh environment, such as wet and dry loading cycles, freezing and thaw cycles, tsunami earthquake loading, tide and wind erosion, UV exposure loading, and etc.
4. Conduct field level applications (design, construction, and monitoring) of the polymer modified soil, such as deep soil mixing, pavement subgrade soil replacement, and embankment and levee fills. Carry out long term

monitoring of their geotechnical properties, for example, settlement, creep, pore-water-pressure change, tomography evolution, strength, as well as leaching properties of the polymer modified fly ash-kaolinite mixtures in the field.

APPENDIX

Upper and Lower Bound Threshold Fly Ash Content Calculation

Case I: Simple Cubic Packing

Given the mass of fly ash (M_{FA}), the number of fly ash cenospheres can be calculated by Equation (4):

$$N_{FA} = \frac{3M_{FA}}{4\pi G_{s-FA}\rho_w\left[R^3-(R-S)^3\right]} \qquad \text{Equation (1)}$$

where M_{FA} is the dry mass of fly ash; the R is the outer radius of the fly ash cenosphere, and ρ_w is the density of water, and S is the fly ash shell thickness, G_{s-FA} is the specific gravity of fly ash.

At simple cubic packing, the void ratio is e_{simple} (e_{simple} =0.91), thus, the total volume of interparticle voids, V_v , is:

$$V_v = \frac{4}{3}\pi R^3 N_{FA} e_{simple} \qquad \text{Equation (2)}$$

Since the interparticle voids are taken up by kaolinite and water, and given the water content of the kaolinite, w (w =0.30, obtained from consolidation test, at 800kPa vertical consolidation stress, which is equivalent to $\sigma'_{corr} = 600kPa$), the volume of the water (V_w) and the volume of the kaolinite (V_{KA}) in the interparticle voids are:

$$V_w = \frac{V_v}{(1+w/G_{s-KA})}, \text{ and } V_{KA} = V_v - V_w \qquad \text{Equation (3)}$$

where G_{s-KA} is the specific gravity of the kaolinite. The mass of kaolinite is $M_{KA} = G_{s-KA}\rho_w V_{KA}$. Putting M_{FA} and M_{KA} into Equation 4, the lower bound threshold fly ash content could be calculated, which is 53.1%.

$$F_{th} = \frac{M_{FA}}{M_{FA} + M_{KA}} \qquad \text{Equation (4)}$$

Case II: Face-Centered Packing

Repeat Equations 1-4, only change the void ratio from e_{simple} to $e_{face-centered}$ (0.35), then the upper bound threshold fly ash content could be calculated, which is 74.6%.

Model Parameters:

R, average radius of the fly ash cenosphere, the diameter of the cenosphere (0.028 mm) is determined from d_{50} value from PSD curve (hydrometer test)

S, shell thickness of cenospheres (0.0033mm, mean shell thickness from statistical analysis of 36 SEM images, see section "shell thickness")

M_{FA}, dry mass of fly ash

M_{KA}, dry mass of kaolinite

G_{s-FA}, specific gravity of fly ash, G_{s-FA}=2.7

G_{s-KA}, specific gravity of kaolinite, G_{s-KA}=2.6

e_{simple}, void ratio when cenospheres in simple cubic packing, e_{simple}=0.91

$e_{face-centered}$, void ratio when cenospheres in face-centered packing, $e_{face-centered}$=0.35

w, water content, which is dependent on the consolidation stress

BIBLIOGRAPHY

Aase, J. K., Bjorneberg, D. L., and Sojka, R. E. (1998). "Springkler irrigation runoff and erosion control with polyacrylamide-laboratory test." *Soil Sci. Soc. Am. J.* 62, 1681-1687.

Al-Khanbashi, A., and Abdalla, S. W. (2006). "Evaluation of three waterborne polymers as stabilizers for sandy soil." *Geotechnical & Geological Engineering*, 24(6), 1603-1625.

Allen, J. C., and Stokoe, K. H. (1982). "Development of Resonant Column Apparatus with Anisotropic Loading." University of Texas at Austin, Austin, TX, 137.

Anandarajah, A., and Zhao, D. (2000). "Triaxial Behavior of Kao- linite in Different Pore Fluids." *J. Geotech. Geoenviron. Eng.*, 126(2), 148–156.

Anandarajah, A., Kuganenthira, N. and Zhao, D. (1996). "Variation of Fabric Anisotropy of Kaolinite in Triaxial Loading." *J. Geo. Engr. Div.*, 122(8), 633-640.

Arasan, S., Akbulut, R. K., Yetimoglu, T., and Yilmaz, G. (2010). "Swelling pressure of compacted clay liners contaminated with inorganic salt solutions." *Environmental and Engineering Geoscience*, 16(4), 401-409.

Arulnathan, R., Boulanger, R. W., and Riemer, M. F. (1998). "Analysis of Bender Element Tests." *Geotechnical Testing Journal*, 21(2), 120-131.

Atesok, G., Somasundaran, P., and Morgan, L.J. (1988). "Charge Effects in the Adsorption of Polyacrylamide on Sodium Kaolinite and Its Flocculation." *Powder Technology*, 54, 77-83.

Bachus, R. and Santamarina, C., (2012). "Geotechnical properties of fly ash and Potential for static liquefaction: Volume I-Summary and Conclusions." EPRI, Palo Alto, CA.

Bate, B. (2010). "Engineering Behavior of Fine-grained Soils Modified with a Controlled Organic Phase." Ph.D. thesis, Georgia Institute of Technology, Atlanta, GA.

Bate, B., and Burns, S. E. (2010). "Effect of Total Organic Carbon Content and Structure on the Electrokinetic Behavior of Organoclay Suspensions." *J. Colloid Interface Sci.*, 343(1), 58–64.

Bate, B., Choo, H., and Burns, S. (2013). "Dynamic Properties of Fine-grained Soils Engineered with a Controlled Organic Phase." *Soil Dyn. Earthquake Eng.*, 53,176–186.

Bate, B., Zhao, Q., and Burns, S. (2014). "Impact of Organic Coatings on the Frictional Strength of Organically Modified Clay." *J. Geotech. Geoenviron. Eng.*, 140(1), 228–236.

Bellotti, R., Jamiolkowski, M., Lo Presti, D. C. F., and O'Neill, D. A. (1996). "Anisotropy of Small Strain Stiffness in Ticino Sand." *Géotechnique*, 46(1), 115–131.

Benchabane, A., Bekkour, K. (2006). "Effects of anionic additives on the rheological behavior of aqueous calcium montmorillonite suspensions." *Rheologica Acta*, 45 (4), 425-434.

Bouazza, A., Gates, W.P., and Ranjith. P.G. (2009). "Hydraulic conductivity of biopolymer treated silty sand." *Géotechnique*, 50(1), 71-72.

Brignoli, E. G. M., Gotti, M., and Stokoe, K. H. (1996). "Measurement of shear waves in laboratory specimens by means of piezoelectric transducers." *Geotechnical Testing Journal*, 19(4), 384-397.

Cabalar, A. F., and Canakci, H. (2005). "Ground improvement by bacteria." *Proc, 3rd Biot Conference on Poromechanics*, May 24, 2005 - May 27, 2005, A.A. Balkema, 707-712.

Castro, G., Enos, J. L., France, J. W., and Polulos, S. J. (1982). "Liquefaction induced by cyclic loading." Report to National Science and Foundation, No. NSF/CEE-82018, National Science Foundation, Washington, D.C.

Chandraprabha, M. N., Natarajan, K. A. and Somasundaran, P. (2004). "Selective separation of arsenopyrite from pyrite by biomodulation in the presence of Acidithiobacillus ferrooxidans." *J. Colloid Interface Sci.,* 276, (2), 323–332.

Chang, I.-H., Cho, G.-C., Lee, J.-G., and Kim, L.-H. (2006) "Characterization of clay sedimentation using piezoelectric bender elements." *Trans Tech Publications Ltd*, 1415-1420.

Chen, S. L., Zhang, L. M., and Chen, L. Z. (2005). "Consolidation of a finite transversely isotropic soil layer on a rough impervious base." *Journal of Engineering Mechanics*, 131(12), 1279-1290.

Cho, G.C., and Santamarina, J.C. (2001). "Unsaturated particulate materials-particle-level studies." *Journal of Geotechnical and Geoenvironmental Engineering,* 127 (1), 84-97.

Choo, H., Bate. B., and Burns, S.E. (2015). "Effects of organic matter on stiffness of overconsolidated state and anisotropy of engineered organoclays at small strain." *Engineering Geology*, 184(14), 19-28.

Cole, D.M., Ringelberg, D.B., Reynolds, C.M. (2012). "Small-Scale mechanical properties of biopolymers." *Journal of Geotechnical and Geoenvironmental Engineering*, 138 (9), 1063-1074.

Craig, R. F., (1997). Soil Mechanics, 6th edn. E&FN Spon, London.

Delage, P. and Lefebvre, G. (1984). "Study of the structure of a sensitive Champlain clay and of its evolution during consolidation." *Canadian Geotechnical Journal***,** 21(1), 21-35.

Di Maio, C. (1996). "Exposure of Bentonite to Salt Solution: Osmotic and Mechanical Effects." *Géotechnique*, 46(4), 695–707.

Di Maio, C. (1998). "Discussion on Exposure of bentonite to salt solution: osmotic and mechanical effects." *Géotechnique*, 48(3), 433-436.

Di Maio, C., and Fenelli, G. B. (1994). "Residual strength of kaolin and bentonite: The influence of their constituent pore fluid." *Géotechnique*, 44(2), 217-226.

Dingrando, J. S., Kalinski, M. E., Salehian, A., and Zand, B. B. (2013). "Cyclic triaxial testing of water pluviated fly ash specimens." *2013 World of Coal Ash Conference*, April 22-25, Lexington, KY, USA.

Doven, A. and Pekrioglu, A. (2005). "Material Properties of High Volume Fly Ash Cement Paste Structural Fill" *J. Mater. Civ. Eng.*, 17(6), 686–693.

Dyvik, R., and Madshus, C. "Lab measurements of G_{max} using bender elements." *Proc., Advances in the Art of Testing Soils under Cyclic Conditions*. Proceedings of a session held in conjunction with the ASCE Convention., ASCE, 186-196.

Ezaoui, A., and Di Benedetto, H. (2009). "Experimental measurements of the global anisotropic elastic behavior of dry Hostun sand during triaxial tests, and effect of sample preparation." *Géotechnique*, 59(7), 621-635.

Fam, M., and Santamarina, C. (1995). "Study of geoprocesses with complementary mechanical and electromagnetic wave measurements in an oedometer." *Geotechnical Testing Journal*, 18(3), 307-314.

Fam, M., and Santamarina, J. C. (1997). "A study of consolidation using mechanical and electromagnetic waves." *Géotechnique*, 47(2), 203-219.

Ferguson, G. (1993). "Use of self-cementing fly ashes as a soil stabilization agent." Fly ash for soil improvement, *Geotechnical Special Publication*, No. 36, 1–14.

Ferguson, G., and Levorson, S.M. (1999). "Soil and Pavement Base Stabilization with Self- Cementing Coal Fly Ash." American Coal Ash Association, Alexandria, VA.

Fernandez, A. L. (2000). "Tomographic imaging the state of stress." PhD, Georgia Institute of Technology, Atlanta.

Fioravante, V., and Capoferri, R. (2001). "On the Use of Multi-directional Piezoelectric Transducers in Triaxial Testing." *Geotechnical Testing Journal*, 24(3), 243-255.

Foster, K.M., Rodriguez-Marek, A., Green, R.A. (2014). "Preliminary results from a study of the dynamic geotechnical properties of coal combustion products (CCP)." *Geotechnical Special Publication*, (234 GSP), 377-388.

Gajo, A., and Maines, M. (2007). "Mechanical effects of aqueous solutions of inorganic acids and bases on a natural active clay." *Géotechnique*, 57(8), 687-699.

Graber, E.R., Fine, P., and Levy, G. J. (2006). "Soil stabilization in semiarid and arid land agriculture." *Journal of Materials in Civil Engineering*, 18(2), 190-205.

Graham, J., Noona, M. L., and Lew, K. V. (1983). "Yield states and stress-strain relationships in a natural plastic clay." *Canadian geotechnical journal*, 20(3), 502-516.

Gregory, J. (1985). "The use of polymeric flocculants." *Proc. of the Engineering Foundation Conference on Flocculation, Sedimentation and Consolidation*, The Clister Sea Island, Georgia, USA. American Institute of Chemical Engineers, New York, USA, pp. 125 – 137.

Hardin, B. O., and Drnevich, V. P., (1972). "SHEAR MODULUS AND DAMPING IN SOILS: MEASUREMENT AND PARAMETER EFFECTS." *ASCE J. Soil Mech Found Div*, 98 (SM6), 603-624.

Hicher, P.Y., Wahyudi, H., Tessier, D. (2000). "Microstructural analysis of inherent and induced anisotropy in clay." *Mechanics of Cohesive Frictional Materials, 5*, 341-371.

Huang, C., and Chen, Y., (1996). "Coagulation of colloidal particles in water by chitosan." *Journal of Chemical Technology and Biotechnology*, 66 (3), 227-232.

Israelachvili, J. N., (2011). "Intermolecular and Surface Forces, 3rd Edition." Academic Press.

Jaky, J. (1944). "The coefficient of earth pressure at rest." *Journal of Society of Hungarian Architects and Engineers*, 7, 355-358.

Janz, M., and Johansson, S. (2002). "The functions of different binding agents in deep stabilization." Swedish Deep Stabilization Research Center Rep. No. 9, Swedish Geotechnical Institute, Linkoping, Sweden.

Jiang, G.-L., Tatsuoka, F., Flora, A., and Koseki, J. (1997). "Inherent and stress-state-induced anisotropy in very small strain stiffness of a sandy gravel." *Géotechnique*, 47(3), 509-521.

Johnson, K. L. (1985). Contact Mechanics, Cambridge University Press.

Jovicic, V., Coop, M. R., and Simic, M. (1996). "Objective criteria for determining G_{max} from bender element tests." *Géotechnique*, 46(2), 357-362.

Jovicic, V., and Coop, M. R. (1998). "The measurement of stiffness anisotropy in clays with bender element tests in the triaxial apparatus." *Geotech. Testing J.* 21(1), 3–10.

Kang, X., Zhao, X., and Bate, B. (2013). "Microscopic and Physicochemical Studies of Fly Ash-Kaolinite Suspensions." *International Workshop in Experimental Micromechanics for Geomaterials*. May 23-24, 2013, The University of Hong Kong.

Kang, X., Kang, G.-C., and Bate, B. (2014). "Measurement of Stiffness Anisotropy of Kaolinite Using Bender Element Tests in a Floating Wall Consolidometer." *Geotechnical Testing Journal*, 37(5), 1-16.

Kang, X., Kang, G-C., Chang, T-K., and Louis, Ge, (2015). "Chemically Stabilized Soft Clays for Road Base Construction." *Journal of Materials in Civil Engineering*, ASCE. 16(4), 04014199. DOI: 10.1061/(ASCE)MT.1943-5533.0001156.

Kavazanjian Jr, E., Iglesias, E., and Karatas, I. (2009). "Biopolymer soil stabilization for wind erosion control." *Proc., 17th International Conference on Soil Mechanics and Geotechnical Engineering*, ICSMGE 2009, October 5, 2009 - October 9, 2009, IOS Press, 881-884.

Kawaguchi, T., Mitachi, T., and Shibuya, S. (2001). "Evaluation of shear wave travel time in laboratory bender element test." *Proc., 15th Int. Conf. on Soil Mechanics and Geotechanics Engineering*, Istanbul, Balkema, 155-158.

Khatami, H. and O'Kelly, B. (2013). "Improving Mechanical Properties of Sand Using Biopolymers." *J. Geotech. Geoenviron. Eng.*, 139(8), 1402–1406.

Kim, B., Prezzi, M., and Salgado, R. (2005). "Geotechnical properties of fly and bottom ash mixtures for use in highway embankments." *J. Geotech. Geoenviron. Engg.*, 131(7), 914-924.

Kim, N. R., and Kim, D. S. (2010). "A shear wave velocity tomography system for geotechnical centrifuge testing." *Geotechnical Testing Journal*, 33(6), 434-444.

Kim, S., and Palomino, A. M., (2009), "Polyacrylamide-treated kaolin: A fabric Study." *Applied Clay Science*, 45, 270-279.

Kim S., and Yang, Y., (2012). "Chitosan-based delivery system for tissue regeneration and chemotherapy." *Engineering biomaterials for regenerative medicine*, pp 321-343.

Knox, D. P., Stokoe, K. H., and Kopperman, S. E. (1982). "Effect of state of stress on velocity of low-amplitude shear waves propagating along principal stress directions in dry sand." Civil Engineering Department, University of Texas at Austin, Report GR82-23.

Kolay, P.K., Bhusal, S. (2014). "Recovery of hollow spherical particles with two different densities from coal fly ash and their characterization." *Fuel*, 117 (PART A), 118-124.

Kuganenthira, N., Zhao, D. and Anandarajah, A. (1996). "Measurement of Fabric Anisotropy in Triaxial Shearing." *Géotechnique*, 46(3):657-670.

Kumar, A., Reed, J., and Sant, G., (2013). "Vertical Scanning Interferometry: A New Method to Measure the Dissolution Dynamics of Cementitious Minerals." *Journal of the American Ceramic Society*, 96 (9), 2766-2778.

Ku, T., Mayne, P. W., and Gutierrez, B. J., (2011). "Hierarchy of V_s Modes and Stress-dependency in Geomaterials." *Proceedings of the Fifth International Symposium on Deformation Characteristics of Geomaterials*, Seoul, South Korea, September 1-3, 2011, Technical Committee 101 (TC101) of International Society for Soil Mechanics and Geotechnical Engineering (ISSMGE), London, UK and Korean Geotechnical Society, Seoul, South Korea. 533–540.

Labille, J., Thomas, F., Milas, M., Vanhaverbeke, C., (2005). "Flocculation of colloidal clay by bacterial polysaccharides: Effect of macromolecule charge and structure." *Journal of Colloid and Interface Science*, 284 (1), 149-156.

Lake, C. B., and Rowe, R. K. (2005). "A comparative assessment of volatile organic compound (VOC) sorption to various types of potential GCL bentonites." *Geotextiles and Geomembranes*, 23(4), 323-347.

Lambe, T. W., (1958). "The engineering behavior of compacted clay." *Jour. Soil Mech. and Fdns. Div.*, ASCE, 84(2), 1-35.

Lee, C., Lee, J.-S., Lee, W., and Cho, T.-H. (2008). "Experiment setup for shear wave and electrical resistance measurements in an oedometer." *Geotechnical Testing Journal*, 31(2), 149-156.

Lee, J.-S. (2003). "High resolution geophysical techniques for small-scale soil model testing." Ph.D dissertation, Georgia Institute of Technology, Atlanta, GA, USA.

Lee, J.-S., and Santamarina, J. C. (2005). "Bender elements: Performance and signal interpretation." *Journal of Geotechnical and Geoenvironmental Engineering*, 131(9), 1063-1070.

Lee, S. H. H., and Stokoe, K. H. (1986). "Investigation of low-amplitude shear wave velocity in anisotropic material." Civil Engineering Department, University of Texas at Austin, Report GR86-06, 34 pages.

Leong, E. C., Cahyadi, J., and Rahardjo, H. (2009). "Measuring shear and compression wave velocities of soil using bender-extender elements." *Canadian geotechnical journal*, 46(7), 792-812.

Leong, E. C., Yeo, S. H., and Rahardjo, H. (2005). "Measuring shear wave velocity using bender elements." *Geotechnical Testing Journal*, 28(5), 488-498.

Li, Q., Ng, C. W. W., and Liu, G. B. (2012). "Determination of small-strain stiffness of Shanghai clay on prismatic soil specimen." *Canadian geotechnical journal*, 49(8), 986-993.

Li, Z., Chen, R., and Zhang, L. (2013). "Utilization of chitosan biopolymer to enhance fly ash-based geopolymer." *Journal of Materials Science*, 48 (22), 7986-7993.

Lupini, J. F., Skinner, A. E., and Vaughan, P. R. (1981), "The drained residual strength of cohesive soils." *Géotechnique*, 31(2), pp.181-213.

Marjanovic, J., and Germaine, J. T. (2013). "Experimental study investigating the effects of setup conditions on bender element velocity results." *Geotechnical Testing Journal*, 36(2), 1-11.

Martin, G. R., Yen, T. F., and Karimi, S. (1996). "Application of biopolymer technology in silty soil matrices to form impervious barriers." *Proc., 7th Australia-New Zealand Geomechanics Conference*, Adelaide, Australia.

Martin, R. T., and Ladd, C. C. (1978), "Fabric of consolidated kaolinite." *Clays and Clay Minerals J.*, 23, 17-25.

Mayne, P. W., and Kulhawy, F. H. (1982). "K_0-OCR relationships in soil." *J. Geotech. Engrg. Div.*, 108(6), 851–872.

Mazzieri, F., Di Emidio, G., and Van Impe, P. (2010). "Diffusion of calcium chloride in a modified bentonite: impact of osmostic efficiency and hydraulic conductivity." *Clays and Clay Minerals,* 58 (3), 351-363.

Meng, J. (2003). "The influence of loading frequency on dynamic soil properties." Ph.D., Georgia Institute of Technology, Atlanta, GA.

Mesri, G., and Olson, R. E. (1970). "Shear Strength of Montmorillonite." *Géotechnique*, 20(3), 261-270.

Mitchell, J. K., and Santamarina, J. C. (2005). "Biological considerations in geotechnical engineering." *Journal of Geotechnical and Geoenvironmental Engineering*, 131 (10), 1222-1233.

Mitchell. J. K., and Soga, K. (2005). "Fundamentals of Soil Behaviors. 3rd ed." John Wiley and Sons, New York.

Mohamad, R., and Dobery, R. (1986). "Undrained monotonic and cyclic triaxial strength of sand." *J. Geotech. Engrg.,* 112(10), 941-958.

Moore, C. A., and Mitchell, J. K., 1974, "Electromagnetic Forces and Soil Strength." *Geotechnique*, 24(4), 627–640.

Mpofu, P., Addai-Mensah, J., and Ralston, J. (2004). "Temperature influence of nonionic polyethylene oxide and anionic polyacrylamide on flocculation and dewatering behavior of kaolinite dispersions." *Journal of Collide and Interface Science*, 271, 145-156.

Nabzar, L., Pefferkorn. E., and Varoqui, R. (1984). "Polyacrylamide-Sodium Kaolinite interactions: Flocculation behavior of polymer clay suspension." *J. Colloid and Interface Sci.* 102(2), 380-388.

Nadukuru, S. S., and Michalowski, R. L. (2012). "Arching in distribution of active load on retaining walls." *Journal of Geotechnical and Geoenvironmental Engineering*, 138 (5), 575-584.

Nasser, M. S., James, A. E., (2006), "The effect of polyacrylamide charge density and molecular weight on the flocculation and sedimentation behavior of kaolinite suspensions." *Separation and Purification Technology*, 52 (2), 241-252.

Natesan, M., Smith, S., Humphreys, K., and Kaya, Y. (2003). "The Cement Industry and Global Climate Change: Current and Potential Future Cement Industry CO_2 Emissions." *Greenhouse Gas Control Technologies – 6th International Conference.* Oxford: Pergamon. pp. 995–1000.

Nath, D.C.D., Bandyopadhyay, S., Gupta, S., Yu, A., Blackburn, D., and White, C. (2010). "Surface-coated fly ash used as filler in biodegradable poly(vinyl alcohol) composite films: Part 1—The modification process." *Applied Surface Science*, 256(9), 2759-2763.

Newman, K., and Tingle, J. S. (2004). "Emulsion polymers for soil stabilization." *Worldwide Airport Transfer Conference*. New Jersey, USA.

Nhan, C.T., Graydon, J.W. and Kirk, D.W. (1996). "Utilizing coal fly ash as a landfill barrier material." *Waste Management*, 16, (7), 587-595.

Ni, S. H. (1987). "Dynamic Properties of Sand under True triaxial Stress States from Resonant Column/Torsional Shear Tests." PH.D., The University of Texas at Austin, Austin.

Ng, C. and Leung, E. (2007). "Determination of Shear-Wave Velocities and Shear Moduli of Completely Decomposed Tuff." *J. Geotech. Geoenviron. Eng.*, 133(6), 630-640.

Ng, C. W. W., Xu, J., and Yung, S. Y. (2009). "Effects of Wetting–Drying and Stress Ratio on Anisotropic Stiffness of an Unsaturated Soil at Very Small Strains." *Can. Geotech. J.*, 46, 1062–1076.

Nugent, R. A., Zhang, G., and Gambrell, R. P. (2010). "The Effect of Exopolymers on the Erosional Resistance of Cohesive Sediments." *Proc., 5th International Conference on Scour and Erosion*, ASCE, San Francisco, CA.

Orts, W., Roa-Espinosa, A., Sojka, R., Glenn, G., Imam, S., Erlacher, K., and Pedersen, J. (2007). "Use of Synthetic Polymers and Biopolymers for Soil Stabilization in Agricultural, Construction, and Military Applications." *J. Mater. Civ. Eng.* 19, 58–66.

Parazak, D.P., Burkhardt, C.W., McCarthy, K.J., and Stehlin, M.P. (1988). "Hydrophobic flocculation." *Journal of Colloid and Interface Scienc*e, 123 (1), 59-72.

Pennington, D. S., Nash, D. F. T., and Lings, M. L. (1997). "Anisotropy of G_0 Shear Stiffness in Gault Clay." *Géotechnique*, 47(3), 391–398.

Pennington, D. S., Nash, D. F. T., and Lings, M. L. (2001). "Horizontally Mounted Bender Elements for Measuring Anisotropic Shear Moduli in Triaxial Clay Specimens." *Geotechnical Testing Journal*, 24(2), 133-144.

Piriyakul, K. (2006). "Anisotropic Stress-Strain Behavior of Belgian Boom Clay in the Small Strain Region." Ph.D., Ghent University.

Podsiadlo, P., Kaushik, A. K., Arruda, E. M. Waas, A. M., Shim, B. S., Xu, J. D., Nandivada, H., Pumplin, B. G., Lahann, J., Ramamoorthy, A., and Kotov, N. A., (2007). "Ultralong and Stiff Layered Polymer Nanocomposites." *Science*, 318, 80-83.

Ringelberg, D.B., Cole, D.M., Foley, K.L., Ruidaz-Santiago, C.M., and Reynolds, C.M. (2014). "Compressive strength of soils amended with a bacterial succinoglycan: Effects of soluble salts and organic matter." *Canadian Geotechnical Journal*, 51 (7), 747-757.

Rivard-Lentz, D. J., Sweeney, L. R., and Demars, K. R. (1997). "Incinerator bottom ash as a soil substitute: physical and chemical behavior." Testing Soil Mixed with Waste or Recycled Materials, ASTM STP 1275, Mark A. Wasemiller, Keith B. Hoddinott, Eds., ASTM.

Roesler, S. K. (1979). "Anisotropic shear modulus due to stress anisotropy." *J. Geotech. Engrg. Div.*, 105(7), 871–880.

Roscoe, K. H.; Schofield, A. N.; Wroth, C. P. (1958), "On the Yielding of Soils", *Geotechnique* 8, 22–53.

Rosenqvist, I. T. (1959). "Physico-chemical properties of soils: soil-water systems." *Jour. Soil Mch. and Fdns. Div.*, ASCE, 85(2), 31-53.

Sachan, A., and Penumadu, D. (2007). "Effect of Microfabric on Shear Behavior of Kaolin Clay." *J. Geotech. Geoenviron. Eng.*, 133(3), 306–318.

Sanchez-Salinero, I., Roesset, J. M., and Stokoe, K. H. (1986). "Analytical studies of body wave propagation and attenuation." Report GR 86-15, University of Texas at Austin.

Santamarina, J. C., and Cascante, G. (1996). "Stress anisotropy and wave propagation: A micromechanical view." *Can. Geotech. J.*, 33, 770–782.

Santamarina, J. C., Klein, K. A., and Fam, M. A., (2001). "Soils and Waves—Particulate Materials Behavior, Characterization and Process Monitoring." John Wiley and Sons, New York.

Schofield, A. N. and Wroth, C. P. (1968). "Critical state soil mechanics." London, McGraw Hill.

Shibuya, S., Mitachi, T., Fukuda, F., and Degoshi, T. (1995). "Strain Rate Effects on Shear Modulus and Damping of Normally Consolidated Clay." *Geotechnical Testing Journal*, 18(3), 365-375.

Shirley, D. J. (1978). "An improved shear wave transducer." *J. Acoust. Soc. Am.*, 63(5), 1643-1645.

Sridharan, A., Rao, S. N. and Rao, G. V. (1971). "Shear strength characteristics of saturated montmorillonite and kaolinite clays." *Soils Found.*, 11, 1–22.

Sridharan, A., and Satyamurty, P. V. (1996). "Potential-distance relationships of clay-water systems considering the Stern theory." *Clays and clay minerals*, 44(4), 479-484.

Stokoe, K. H., II, Lee, S. H. H., and Knox, D. P. (1985). "Shear moduli measurements under true triaxial stresses." *Proc., Advances in the Art of Testing Soils under Cyclic Conditions*, ASCE, Reston, Va., 166–185.

Swenson, J. Smalley, M. V. and Hatharasinghe, H. L. M. (1998). "Mechanism and Strength of Polymer Bridging Flocculation." *Phys. Rev. Lett.* 81, 5840-5843.

Tan, X., Hu, L., Reed, A.H., Furukawa, Y., Zhang, G. (2014). "Flocculation and particle size analysis of expansive clay sediments affected by biological, chemical, and hydrodynamic factors, Topical Collection on the 11th International Conference on Cohesive Sediment Transport." *Ocean Dynamics*, 64 (1), 143-157.

Theng, B. K. G. (1982). "Clay-polymer interactions: summary and perspectives." *Clays and Clay Minerals*, 30(1), 1-10.

Thomann, T. G., and Hryciw, R. D. (1990). "Laboratory measurement of small strain shear modulus under K_0 conditions." *Geotechnical Testing Journal*, 13(2), 97-105.

Vempati, R.K., Rao, A., Hess, T.R., Cocke, D.L. and Lauer, H.V. (1994). "Fraction and characterization of Texas lignite class F fly ash by XRD, TGA, FTIR and SFM." *Cement and Concrete Research*, 24, 1153-1164.

Viggiani, G., and Atkinson, J. H. (1995). "Interpretation of bender element tests." *Géotechnique*, 45(1), 149-154.

Walker, T.R. (2005). "Comparison of anthropogenic metal deposition rates with excess soil loading from coal, oil and gas industries in the USA Basin, NW Russia." *Polish Polar Research*. 26(4), 299-314.

Wang, D., Zhang, Y., Dong, A., Tang, Y., Wang, Y., Xia, J., and Ren, N., (2003). "Conversion of fly ash cenosphere to hollow microspheres with zeolite/mullite composite shells." *Adv. Funct. Mater.* 13(7), 563-567.

Wang, S., Zhang, L., Yan, B., Xu, H., Liu, Q., Zeng, H. (2015). "Molecular and surface interactions between polymer flocculant chitosan g polyacrylamide and kaolinite particles: Impact of salinity." *Journal of Physical Chemistry C*, 119 (13), 7327-7339.

Wang, Y. H. and Siu, W. K. (2006). "Structure Characteristics and Mechanical Properties of Kaolinite Soils. II. Effects of Structure on Mechanical Properties." *Can. Geotech. J.*, 43(6), 601–617.

Wang, Y. H. and Mok, C. B., (2008). "Mechanisms of Small strain Shear-modulus Anisotropy in Soils." *J. Geotech. Geoenviron. Eng.*, 134(10), 1516–1530.

Wheeler, S. J., and Sivakumar, V. (2000). "Influence of compaction procedure on the mechanical behavior of an unsaturated compacted clay. Part 2: Shearing and constitutive modelling." *Géotechnique*, 50(4), 369-376.

White, D. J., Harrington, D.S., and Thomas, Z. (2005). "Fly ash soil stabilization for non-uniform subgrade soils, Volume I." Engineering properties and construction guidelines, Center for Transportation Research and Education, Iowa State Univ., Ames, IA.

Wijewickreme, D., Karimian, H., and Honegger, D., (2009). "Response of buried steel pipelines subjected to relative axial soil movement." *Canadian Geotechnical Journal*, 46 (7), 735-752.

Williams, C. R., Cascione, A. A., Cochran, W. E., and Hernandez, B. N. (2014). "Development of Bio-based polymers for use in asphalt." Iowa State University.

Wood, D. M. (1990). "Soil Behavior and Critical State Soil Mechanics." Cambridge University Press, Cambridge, UK.

Xu, S., and Boyd, S. A., (1995). "Cationic surfactant adsorption by swelling and nonswelling layer silicates." *Langmuir*, 11, 2508-2514.

Yamashita, S., Kawaguchi, T., Nakata, Y., Mikamt, T., Fujiwara, T., and Shibuya, S. (2009). "Interpretation of international parallel test on the measurement of G_{max} using bender elements." *Soils and Foundations*, 49(4), 631-650.

Yeboah, N. N. N., and Burns, S., (2011). "Geological disposal of energy-related waste." *KSCE Journal of Civil Engineering*, 15 (4), 697-705.

Yimsiri, S., and Soga, K. (2000). "Micromechanics-based stress-strain behavior of soils at small strains." *Géotechnique*, 50 (5), 559-571.

Yoshizawa H., Chen Y.L., Israelachvili J. (1993). "Fundamental mechanisms of interfacial friction. 1. Relation between adhesion and friction." *Journal of Physical Chemistry*, 97, 4128-4140.

Young, R. N., and Warith, M. A. (1989). "Leaching effect of organic solution on geotechnical properties of three clay soils." *Proc. of 2nd Symposium on Environmental Geotechnology*, Vol.1, Envo. Pub. Inc., Bethlehem, 99–110.

Yu, P., and Richart, F. E. (1984). "Stress Ratio Effects on Shear Modulus of Dry Sands." *Journal of Geotechnical Engineering*, 110(3), 331-345.

Yun, T.S., Santamarina, J.C. (2005). "Decementation, softening, and collapse: Changes in small-strain shear stiffness in K_0 loading." J*ournal of Geotechnical and Geoenvironmental Engineering*, 131 (3), 350-358.

Zhang, G., Yin, H., Lei, Z., Reed, A. H., and Furukawa, Y. (2013). "Effects of exopolymers on particle size distributions of suspended cohesive sediments." *Journal of Geophysical Research: Oceans*, 118, 3473-3489.

VITA

Xin Kang was born in Qingjian, Shaanxi, P.R. China. He graduated from Chang An University with a first class honors degree in Geological Engineering. After completing his B.S., he spent six years in Graduate School and received a M.S. in Geotechnical Engineering (2011) and Ph.D. in Civil Engineering (2015), all from the Missouri University of Science and Technology, USA. His Doctoral research was focused on the physicochemical and Mechanical characteristics of high volume fly ash-soil mixtures modified with controlled organic phase and particulate interactions at Nanoscale. He has worked as a Teaching/Research Assistant for three classes and six research projects since 2009. He has accumulated rich experience in geotechnical laboratory testing including soil index properties, consolidation, hydraulic conductivity, static and cyclic triaxial shear/direct simple shear/direct shear, pulse velocity, zeta potential, and bender elements. His research interests focus on the sustainable soil modification and remediation applications in Geotechnical, Geoenvironmental, and Mining Engineering, with particular emphasis on the productive and beneficial reuse of industrial waste materials; physicochemical behaviors of organic and inorganic treated soil (interfacial at nanoscale); pavement and subgrade soil stabilization; development of smart sensors (Piezoelectric / Ultrasonic / Thermal) for NDT; and Energy related geo-engineering.